Optical Super-Resolution Microscopy of the Structure and Dynamics of Cellular Nanopores

Viola Mönkemöller

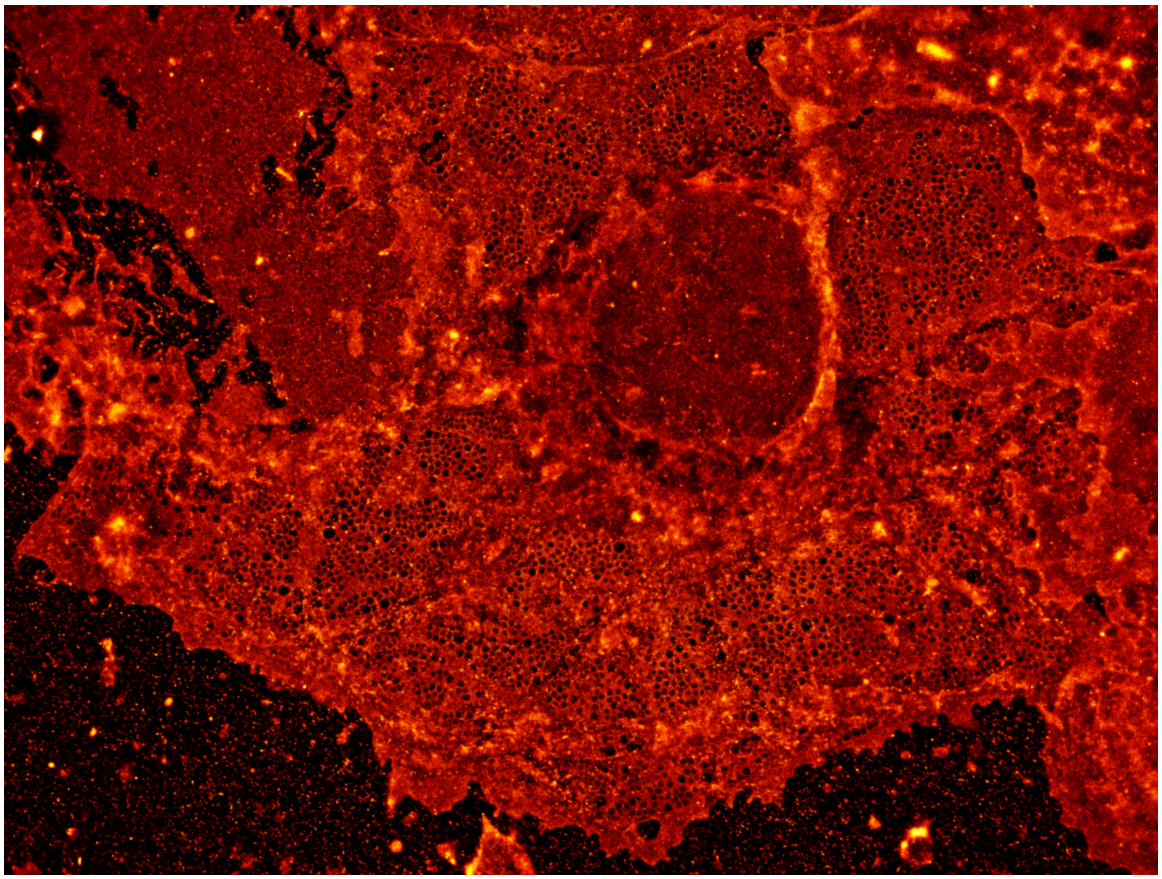

Bielefeld 2016

Optical Super-Resolution Microscopy of the Structure and Dynamics of Cellular Nanopores

Viola Mönkemöller

Dissertation
an der Fakultät für Physik
der Universität Bielefeld
Bielefeld

vorgelegt von
Viola Mönkemöller
aus Bielefeld

Erstgutachter: Prof. Dr. Thomas Huser
Zweitgutachter: Prof. Dr. Andreas Hütten

Contents

1. Introduction **1**

2. Optical nanoscopy **5**
2.1. Microscopy techniques . . . 5
2.2. Fluorescence microscopy . . . 7
2.2.1. Resolution limit . . . 10
2.2.2. Confocal laser scanning microscopy . . . 13
2.2.3. Two-photon excitation microscope . . . 15
2.3. Photon-reassignment microscopy . . . 16
2.4. Optical super-resolution microscopy . . . 18
2.4.1. Stimulated emission depletion (STED) . . . 18
2.4.2. Single molecule localization microscopy based techniques . . . 20
2.4.3. Structured Illumination Microscopy . . . 23

3. LSECs - Liver Sinusoidal Endothelial Cells **29**
3.1. Function and morphology . . . 29
3.2. Human LSECs in 3D-structured illumination microscopy . . . 31
3.3. Preparation of LSECs from rat . . . 31
3.4. Freezing and thawing of LSECs . . . 33
3.5. Confocal microscopy images of LSECs . . . 34

4. LSECs imaged by SMLM compared to 3D-SIM **37**
4.1. *d*STORM on LSECs . . . 37
4.2. Evaluation of the fenestration diameter in *d*STORM vs. 3D-SIM . . . 39
4.3. Acquisition speed . . . 43
4.4. Conclusion . . . 44

5. LSECs imaged by SMLM and 3D-SIM on the same setup **47**
5.1. Correlative SMLM and 3D-SIM on the same setup . . . 47
5.2. Correlative SMLM and 3D-SIM of LSECs . . . 50
5.3. Rapid multi-color 3D-SIM overviews combined with super-resolution of SMLM . . . 53
5.4. Correlation between the membrane and cytoskeleton in LSECs . . . 55

6. Fluorescence stains and their effect on living cells **59**
6.1. The plasma membrane . . . 59
6.2. Lectins . . . 60
6.2.1. Wheat germ agglutinin . . . 60

6.2.2. *Ulex europaeus* agglutinin 61
6.2.3. Intercalating dyes 63

7. Fenestration dynamics and structural changes of living LSECs 77
7.1. Fenestration dynamics of living LSECs 77
7.2. Effect of different substances on living rat LSECs 79
7.3. Ethanol and paracetamol treatment 82

8. Instant SIM and its extension to two-photon microscopy 85
8.1. LSECs imaged by instant SIM 85

9. Further super-resolution projects 91
9.1. Visualizing lipid nanodomains in mammalian cells 91
9.2. Open-source image reconstruction of super-resolution SIM data in ImageJ 93
9.3. Nanoparticles as nonfluorescent analogues of fluorophores 96

Conclusions and outlook 107

A. Preparation and staining protocols 111
A.1. LSECs - Liver Sinusoidal Endothelial Cells 111
A.2. LSECs imaged by SMLM compared to 3D-SIM 112
A.3. LSECs imaged by SMLM and 3D-SIM on the same setup 112
A.4. Fluorescence stains and their effect on live cells 113
A.5. Fenestration dynamics and structural changes of living LSECs 115
A.6. Instant SIM and its extension to two-photon microscopy 116
A.7. Visualizing lipid nanodomains in mammalian cells 116
A.8. Open-source image reconstruction of super-resolution SIM data in ImageJ 117
A.9. Nanoparticles as nonfluorescent analogues of fluorophores 117

B. Materials and methods 119
B.1. Materials 119
B.2. *d*STORM imaging 119
B.3. 3D-SIM imaging 120

Acknowledgment 131

1. Introduction

Microscopy is an important imaging technique for the life sciences. Fluorescence microscopy in particular enabled the visualization and quantitation of various biochemical processes in living cells for the first time. Providing unprecedented contrast and specificity, it is a technique well suited for live cell imaging. These days a broad palette of fluorophores is available, specialized for different targets and imaging conditions. Commonly used fluorescent markers are small organic dyes, fluorescent proteins or quantum dots. Operating at wavelengths of visible light, the resolution obtained by conventional fluorescence microscopy is, however, limited by diffraction to about 200 nm [1]. Many relevant inner-cell processes and therefore desired imaging targets are smaller than this and cannot be resolved.

During the last decades, fluorescence microscopy was revolutionized by a number of developments. Novel imaging methods, the so-called nanoscopy techniques, were developed to overcome the diffraction limit (in the optical far-field), and have been awarded with the Nobel prize in chemistry in 2014 [2]. For instance, stimulated emission depletion (STED) [3], photoactivated localization microscopy (PALM) [4] and the stochastical optical reconstruction microscopy (STORM) [5] methods have the potential for imaging structures down to the molecular scale. These techniques rely on fluorescent probes and use techniques to modify their fluorescent properties to achieve optical super-resolution, while other techniques use light modulation to enhance the spatial resolution, such as structured illumination microscopy (SIM) [6, 7].

Depending on the specific nanoscopy technique and desired spatial resolution, however, certain trade-offs with respect to fluorescent stainings or sample preparation have to be made. Single molecule localization based techniques (PALM, STORM) require long overall acquisition times by collecting several thousands of raw frames to achieve the very high spatial resolution. Often high laser intensities or UV-illumination are used, leading to phototoxic effects in living cell samples.

The resolution of STED also depends strongly on the laser intensity, and a balance between desired resolution and phototoxic effects is essential. As a point-scanning technique it is limited in acquisition speed, such as the confocal microscope it is based on.

In contrast (3D)-SIM uses moderate photon densities and does not depend on specialized fluorophores. The required raw data set are 9 images per z-slice (15 for 3D-SIM) with a shifting structured illumination pattern applied during the acquisition, which makes this technique very fast. However in linear SIM the resolution is limited to a two-fold improvement (about 100 nm in lateral direction).

All of these techniques have advantages and disadvantages and their use always needs to be adapted to the specific biological problem at hand.

LSECs as a sample structure for super-resolution microscopy

A good example for the need of super-resolution microscopy is the investigation of liver sinusoidal endothelial cells (LSECs). These physiologically important cells act as a filter between the blood and hepatocytes, and therefore have a direct effect on the liver function [8]. A number of clinical conditions, especially metabolic and aging-related disorders, are related to improper function of LSECs. Furthermore the disruption of these cells due to e.g. paracetamol poisoning can lead to acute liver failure and death [9].

LSECs are a challenging target to image for conventional microscopy techniques, even for confocal microscopes, due to their special morphological substructure [10]. They contain a large number of transcellular pores, so-called fenestrations that are grouped into sieve plates. From the 1950s up to recently, fenestrations could only be resolved by transmission or scanning electron microscopy (TEM/SEM) due to their small size. EM methods have certain drawbacks: they require extensive sample preparation including drying steps that can lead to artifacts. Therefore EM methods are not suitable to study the function and dynamics of fenestrations in living LSECs, which is why fenestrations are still poorly understood and thus provide an ideal target for optical microscopy. With a diameter of about 50 to 200 nm fenestrations are well below the optical diffraction limit. Their size and the fact that there are no specific markers for fenestration labeling has so far prohibited any functional analysis of living LSECs with standard and advanced light microscopy techniques. Preceding this work, Cogger and colleagues [11, 12] published first studies that employ super-resolution techniques to LSECs, where they used 3D-SIM to image fenestrations in sieve plates in fixed LSECs.

Super-resolution microscopy of LSECs

The work at hand uses two different super-resolution methods and their multi-modal combination to image fixed and live LSECs. To provide the context for this work chapter 2 contains a brief but comprehensive overview of the basics of fluorescence microscopy, as well as the standard and super-resolution techniques employed in this research. Chapter 3 provides an overview of the biological target (LSECs).

Single molecule localization microscopy of LSECs

I successfully employed direct stochastic optical reconstruction microscopy (*d*STORM) for the first time to image the fenestrations in LSECs with a unprecedented resolution for optical microscopy, which surpasses SIM by a factor of 5 [13] (see chapter 4). For the application of *d*STORM to this type of imaging, some challenges had to be overcome: Due to lacking markers for fenestrations I had to work with a negative counter-staining, in which the membrane around the fenestrations is stained. Single molecule based techniques are mostly used to image spots or one-dimensional structures, such as actin filaments. The imaging of hollow/empty structures such as fenestrations on a brightly stained membrane poses a challenge for these techniques. Another issue was the selection of a suitable dye that enables a stochastic photoswitching behavior while still staining

the membrane very densely. The super-resolved images are compared to 3D-SIM and SEM measurements.

Multi-modal nanoscopy of LSECs

Many applications, in particular live cell imaging applications, require both, a rapid search mode that enables the identification of cells/areas of interest, which can then be followed by more time-consuming, super-resolution microscopy measurements of the relevant features. To take advantage of two different nanoscopy methods I used a multi-modal approach by correlating *d*STORM and 3D-SIM in a single imaging platform, the results of which can be found in chapter 5. There are a few attempts of groups who use multi-modal nanoscopy [14, 15, 16], however, the combination of both techniques in this way, combining the specific advantages of each technique, was not previously performed.

I demonstrated the ability of a single optical platform to rapidly search, survey, and stitch large sample areas for relevant features (with sizes below the diffraction limit) in multi-color operation, on freshly isolated fixed rat LSECs. Once areas with sieve plates are identified, the illumination and acquisition mode of the microscope is switched to *d*STORM to revisit these locations and enable imaging of the LSEC cytoskeleton and fenestrations with up to 20 nm optical resolution.

The combination of both methods enabled me to also directly compare areas imaged by two different super-resolution modalities, which ultimately enabled us to reveal the close association between the LSEC cytoskeleton and the plasma membrane.

Membrane dyes and their effects on live LSECs

Since 3D-SIM imaging is faster and still yields sufficient spatial resolution to image fenestrations in LSECs, this technique is used for live cell imaging experiments. In chapter 6 the efforts to find a suitable dye for live LSEC super-resolution imaging are shown. A wide range of membrane dyes are available, e.g. intercalating dyes or lectins that bind to carbohydrates which are located outside of the cell on the plasma membrane.

I managed to obtain the first live LSEC images, which enabled me to follow fenestration formation and dynamics that are further analyzed in chapter 7. Furthermore different treatments on live LSECs were tested in this chapter, such as the actin disruptor Swinholide A. Live imaging of actin and the membrane reveal the dramatic effects of this toxin. In addition preliminary experiments on ethanol and paracetamol poisoning are analyzed by 3D-SIM.

Instant SIM and further projects

I also tested another state-of-the-art live cell high-resolution imaging technique (Chapter 8): instant structured illumination microscopy (based on prior work by York et al. [17]). This technique provides fast high-resolution imaging by using parallelized focus illumination and optical compression. The resolution is better than in a confocal microscope, however it is worse than in 3D-SIM. The experiments with fixed LSECs show the general feasibility for this technique even with LSECs. Furthermore I started to set up

a two-photon instant SIM microscope, which will allow fast observations of dynamics in thick tissue samples with a nearly two-fold resolution increase.

In the final chapter 9, other published side projects are described. I applied the multimodal technique (introduced in chapter 5) for the complementary analysis of lipid nanodomains in neural crest-derived stem cells (NCSCs) [18]. These nanodomains are believed to be crucially involved in the regulation of signal transduction pathways in mammalian cells. Due to their small size (diameter 10-200 nm), they cannot be directly imaged using conventional light microscopy. Super-resolved fluorescence images that I obtained reveal the distribution of Ganglioside 1 in NCSCs by 3D-SIM and SMLM.

In another project I contributed to the development of the open-source reconstruction software fairSIM as a plugin for ImageJ/Fiji. With optical nanoscopy techniques becoming increasingly cost-effective, research groups building their own set-ups are greatly benefiting from such ready-to-use reconstruction software. To avoid background effects optical sectioning can be applied (this is also demonstrated in chapter 9). The software was tested on different data sets gained by 3D-SIM using single slice reconstruction for 2D analysis.

Furthermore, I investigated an alternative for fluorophores that can be used for super-resolution techniques. With fluorophores the observation time and the spatial resolution is often limited by photo-bleaching of fluorescent probes. This bleaching effect is fatal in 3D-SIM and leads to artifacts in the reconstructions. I demonstrate in chapter 9 that Raman scattering nanoparticles also provide valuable, non-bleaching contrast for optical nanoscopy.

The majority of the results presented in this thesis have already been published in several peer-reviewed journal articles. The corresponding articles are referenced in the respective chapters.

2. Optical nanoscopy

Generally speaking, microscopy is a technical field that uses magnifying techniques to image objects that are too small to be seen with the naked eye. There are three widely used types of microscopes: *scanning probe*, *electron* and *optical microscopes*. Optical fluorescence microscopy is the basis for the nanoscopy techniques used in this work. Its working principles are described in detail in this chapter.

2.1. Microscopy techniques

Scanning probe microscopes use a probe tip to scan the specimen and form an image. The most commonly used techniques are Atomic Force Microscopy (AFM) and Scanning Tunneling Microscopy (STM). An AFM uses a cantilever with a sharp tip scanning the sample, and by analyzing acting forces between tip and sample (e.g. van der Waals) a three dimensional image of the surface can be reconstructed [19]. A STM uses the concept of quantum tunneling by scanning a conducting tip with a bias voltage applied between tip and sample and measuring the tunneling current. There are also photon-sensing scanning probe techniques such as Scanning Nearfield Optical Microscopy (SNOM). SNOM is a surface analyzing technique that uses the properties of evanescent waves to gain 20 nm resolution. These non-propagating fields only exist close to the surface of an analyzed object and carry high frequency spatial information about it. Therefore SNOM achieves resolutions beyond the far-field diffraction limit [20].

Electron microscopes are in general divided into two types: Transmission Electron Microscope (TEM) and Scanning Electron Microscope (SEM). In a TEM the electrons pass through the (thinned) sample and undergo scattering or absorption on their way to the detector, depending on the sample composition. For example in bright field mode the contrast depends on the thickness and the atomic number of analyzed regions. Whereas thicker and high atomic number materials appear dark, regions with no sample in the beam appear bright [21, 22]. In SEM an electron beam is scanned across the sample surface. Backscattered or secondary electrons are detected and generate the image. The brightness depends on the number of electrons reaching the detector. This is influenced by the angle between electron beam and surface. For instance flat sample surfaces perpendicular to the beam have a smaller activated region emitting secondary electrons in contrast to steep surfaces and edges. These tend to be brighter due to an increased interaction volume resulting in more secondary electrons. The results are bright edges with darker flat areas which results in images of three dimensional appearance [23, 24]. The drawback of this method is the extensive sample preparation which includes drying of the sample that can lead to changes and therefore artifacts in the biological

material. TEM requires thinned samples while in SEM non-conductive samples are often additionally sputtered with gold to avoid charging effects which would lead to imaging artifacts.

A Helium Ion Microscope (HIM) works in a similar way as a SEM but instead with electrons the sample is scanned with a helium beam. The advantage of this technique is the high yield of secondary electrons for similar beam intensities and a smaller excitation volume inside the sample. HIM is therefore more surface sensitive and provides a higher depth of field.

During the last century TEM (1932 [21, 22]), SEM (1937 [23, 24]) and AFM (1986 [19]) were the well-established imaging methods that are used by a wide range of scientist to analyze systems down to the nanoscopic scale.

Optical microscopy

Optical microscopes were invented over 500 years ago. Instead of electrons or physical probes photons are used to generate a microscopic image. In a simple bright-field microscope the image can directly be seen by the eye. The contrast is gained by absorbing and scattering light on the path to the eye/detector. Even with these rather simple instruments imaging important biological / bio-medical research was possible, for example it led to the discovery of bacteria at the turn of the 17th century [25].

Phase contrast, polarization and dark-field microscopy are able to enhance the contrast. Dark-field uses a patch stop to filter the direct light of the lamp and leads to an illumination of the sample from the side. Since the direct light path to the detector is blocked only scattered light will reach the objective. Scattering structures in the sample (e.g. changes in diffractive index) appear bright in front of a dark background.

Phase contrast microscopy requires a modification of the excitation light by a condenser. The direct non-scattered light is passed through a phase shift ring which leads to a -90°phase shift of half of the light and a reduction in background light due to destructive interference. The phase contrast is then created when the scattered and the direct light interfere constructively, i.e., when a sample structure changes the phase of the transmitted light. This results in an increase of brightness and contrast.

For polarization microscopy the sample is illuminated with polarized light and an opposing polarization filter is placed into the detection path of the microscope. In that way, all light directly passing the sample is blocked by the filter. Only processes changing the polarization, e.g. scattering in the sample, allow light to pass the filter and appear as bright structures.

While some basic biological research is possible with these illumination types, most questions cannot be answered. Features in cells such as actin fibers remain not visible, for instance. There the absorption and scattering does not give the contrast information that is needed for many questions. This is due to the homogeneity in diffraction and absorption index of biological materials. In general features such as cell walls and nuclei can be seen, but all other interior structures remain unseeable.

Fluorescence microscopy has revolutionized the imaging in life science. In fluorescence microscopy it is possible to selectively stain specific structures and therefore gain a

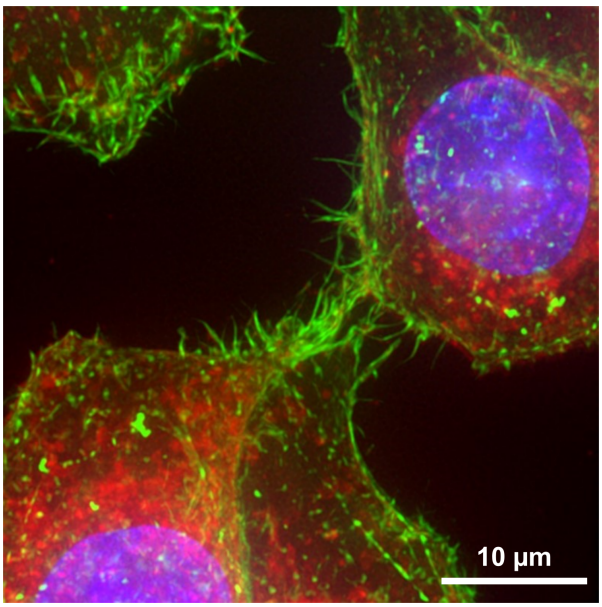

Figure 2.1.: This example of a fluorescence micrograph shows an U2OS cell stained with DAPI for the nucleus (blue), Phalloidin-ATTO 488 for actin (green) and CellMask Orange for membrane (red). Especially the actin structure would not yield contrast in an non-fluorescent microscopy technique.

high contrast (see Figure 2.1). Fluorescence microscopy is one of the most important techniques in modern life sciences and will be explained more precisely in the next section.

2.2. Fluorescence microscopy

The physical effect of fluorescence is the eponym of this technique. Fluorescence occurs when molecules, e.g. fluorochromes, can be excited by light while nanoseconds later they emit light of a lower frequency. This is the so-called *Stokes-shift* as seen in Figure 2.2 (a). The difference in absorption and emission wavelength allows for an optical separation by dichroic mirrors. They separate the much brighter excitation light from the weak emitted light. This optical element makes it possible that in epifluorescence as seen in Figure 2.4 the same objective can be used for excitation and emission. With additional band pass filters of the suitable wavelength windows the fluorescent image shows only the structure of interest that was labeled with the fluorescent dye. The Stokes-shift can be exemplified with help of the *Jablonski diagram* as seen in Figure 2.2 (b). According to Kasha's rule the photon emission occurs from the lowest excited vibrational state of S_1 [26]. The excited molecule relaxes to this state in a non-radiative transition process. Therefore the emitted photons have lower energy than the absorbed ones.

Notably the absorption and emission spectrum look like mirror images of one another. This can be explained with the *Franck-Condon principle* (Figure 2.3) [27]. According to the Franck-Condon principle electronic transitions occur instantly compared to movement of the nuclei in the molecules (Figure 2.3 (a)). The transition probability depends

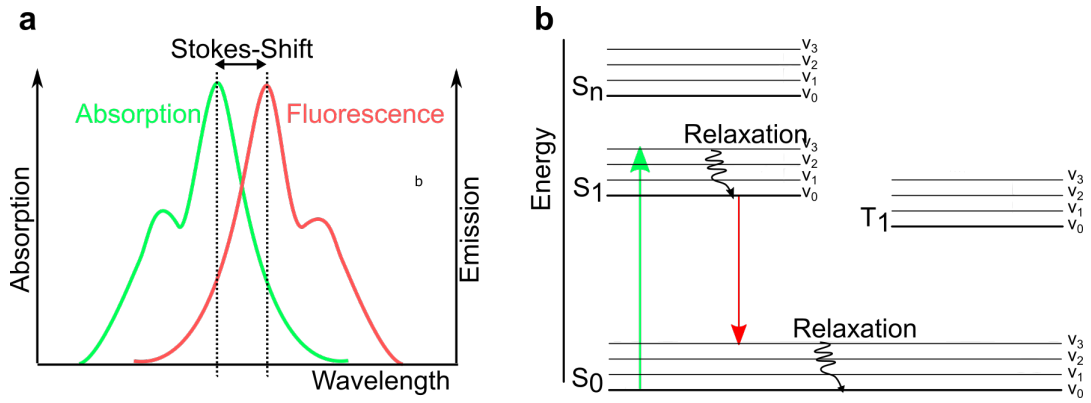

Figure 2.2.: (a) Absorption and emission spectra of a fluorescent molecule show the Stokes-shift according to their peaks. (b) The Jablonski diagram is a simple representation of possible energy levels of a molecule and the transitions between these levels. From the ground state S_0 an electron is excited by absorption of a photon to a vibrational energy level S_1, the first excited singlet state. Photon emission then occurs from the lowest excited vibrational state S_1V_0, after a non-radiative relaxation of the excited molecule to this state. These relaxations to the vibrational ground state V_0 are very quick, so both excitation and emission processes always start out at V_0 levels.

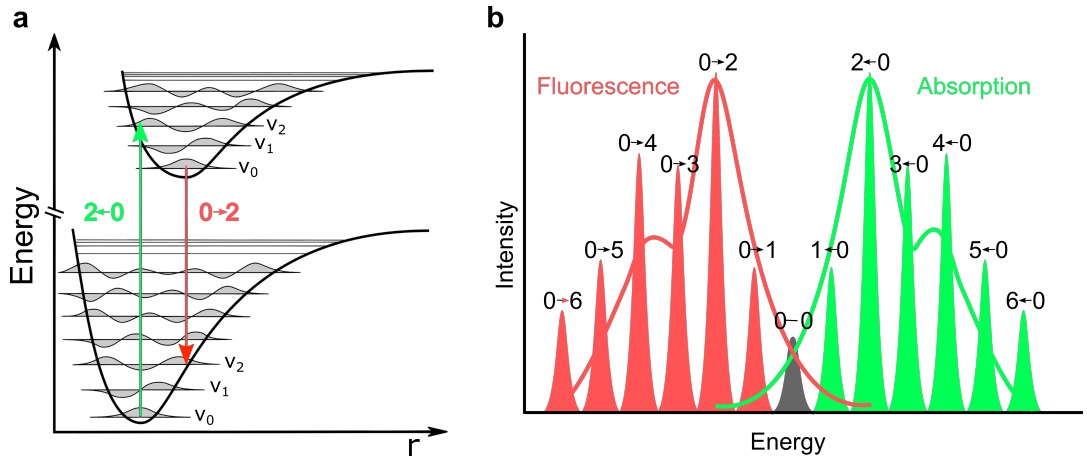

Figure 2.3.: (a) Franck-Condon principle energy diagram. Transitions to a certain vibrational state V_n are more likely if they do not yield a large shift in radius r. Since these transitions probabilities are nearly symmetric for $S_0V_0 \rightarrow S_0V_n$, absorption and emission spectra are mirrored. (b) Illustration of the corresponding absorption and emission spectra to the energy diagram in (a), showing the mirrored transition probabilities and the room-temperature continuous spectra.

on the compatibility of the vibration wave functions of both states. This means certain transitions (e.g. $2 \rightarrow 0$ and $0 \rightarrow 2$) are more probable and therefore contribute to higher intensities in the absorption and emission spectra (Figure 2.3 (b)).

The schematic image of a simple wide-field setup is pictured in Figure 2.4. Here a laser acts as an excitation light source. After widening the excitation beam with a telescope it is directed to the back-focal plane of an objective. The objective parallelizes the beam (epifluorescence) and collects the emitted light from the sample. The dichroic mirror separates excitation and emission light due to the above mentioned Stokes-shift. A lens

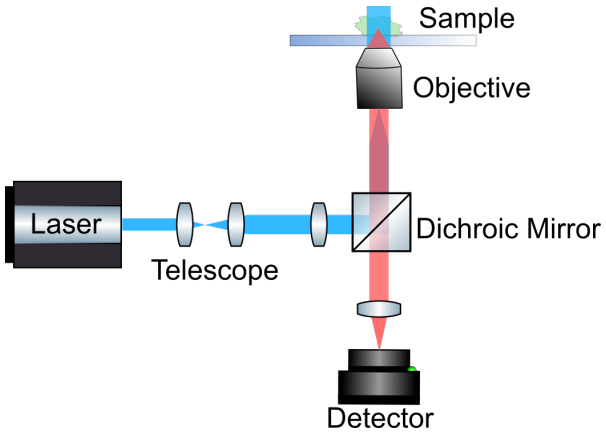

Figure 2.4.: A monochromatic excitation light source (laser, LED, filtered Hg bulb) is used to illuminate the sample on a microscope. The emitted light is separated from the excitation light with a dichroic mirror and focused on the detector, e.g. a CCD camera. The illumination light path is using the same objective as the detection, with is deemed *epi-illumination*. As a so-called wide-field instrument, the field-of-view is fully and evenly illuminated, which allows for high acquisition speed (primarily limited by the photon budget and camera speed).

focuses the image on the detector, e.g. a CCD (Charge-Coupled Device) or CMOS (Complementary Metal-Oxide-Semiconductor) camera.

There are different fluorescent markers that can be used to stain structures or chemical compounds in biological samples as seen in Figure 2.5 (a - c). Fluorescent dyes can be used to stain different biological structures by using different labeling approaches such as Phalloidin (d) and Immunoglobulins (e). Due to the variety of dyes they can be stained and detected simultaneously, while still being specific due to the individual color of the dye.

Fluorescent proteins (e.g. enhanced Green Fluorescent Protein (eGFP) in Figure 2.5 (b)) have been developed in molecular biology [30]. By using gene fusion the expression of the fluorescent compound can be linked to that of the target protein. The advantages are non-toxicity and a rare interference with the function of the protein under study. By genetical modification of cells or organisms which directly express the fluorescently tagged proteins, it is possible to study the functions of the original protein in vivo [31].

Organic fluorophores, such as Alexa Fluor [32] and ATTO dyes [33] (Figure 2.5 (a)), are chemically designed photostable dyes. They have a typical size of 1 - 2 nm, but require a chemical labeling procedure, e.g. the fluorophore needs to be bound to an antibody.

It is also possible to use quantum dots for life science experiments. They are fluorescent semiconductor nanoparticles of 5 - 20 nm diameter. Due to their high extinction coefficients they are in general brighter than other fluorescent dyes and undergo less photo-bleaching [34]. Due to their size and to their irregular blinking organic fluorophores are preferred in this thesis.

Figure 2.5 (f) shows an alternative to fluorochromes: Surface Enhanced Raman Scattering nanostructures (SERS). The physical effect is Raman scattering which is in contrast to fluorescence no resonance phenomenon and occurs in virtual levels. An advan-

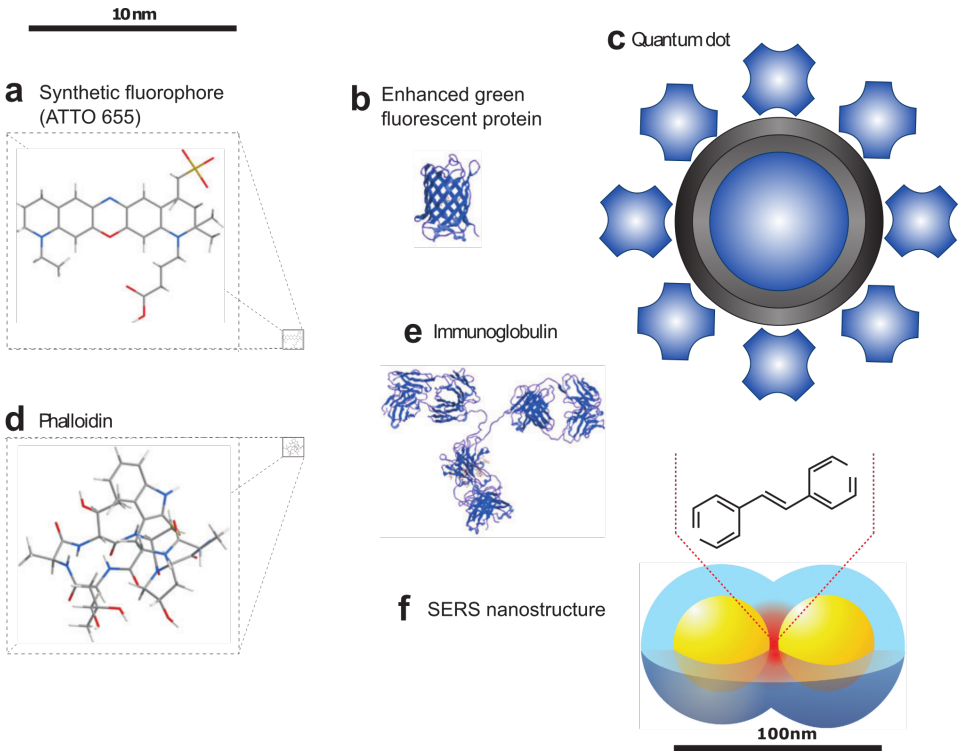

Figure 2.5.: Size comparison of (a) synthetic fluorophore (ATTO 655), (b) a monomeric fluorescent protein (eGFP), (c) a streptavidin coated quantum dot, (d) Phalloidin, (e) a typical Antibody (Immunoglobulin) and (f) a SERS nanostructure with adherent Raman-active molecules. The structural formulas for the synthetic fluorophores are shown with tenfold magnification, while the SERS nanostructure has different scale bar and is a ten fold demagnification compared to the other structures. Adapted from [28] and [29]

tage is the absence of bleaching as shown in [35] and in chapter 9.

Often cells or their components are autofluorescent at certain wavelengths [36]. This effect can disturb measurements with fluorescent markers. Some microscopes, e.g. specialized versions of confocal microscopes, are able to differentiate between the different lifetimes of excited states in autofluorescence and the fluorophores. In general, however, the aim is to avoid autofluorescent effects as good as possible, by e.g. selection of fluorophore wavelength, sample preparation and selection of bandpass filters.

There are many developments in fluorescence microscopy and technical subcategories as can be seen in Figure 2.6. In this thesis CLSM, *d*STORM, 3D-SIM and instantSIM are used and described in the next sections.

2.2.1. Resolution limit

In an optical microscope the resolution is often defined as the minimal distance of two structures (typically point-like light emitters) that can still be seen as two distinguishable objects. Different limits, such as the Abbe-, Sparrow-, and Rayleigh-limit can be used to compute this distance. They are deduced from interference effects in an optical system

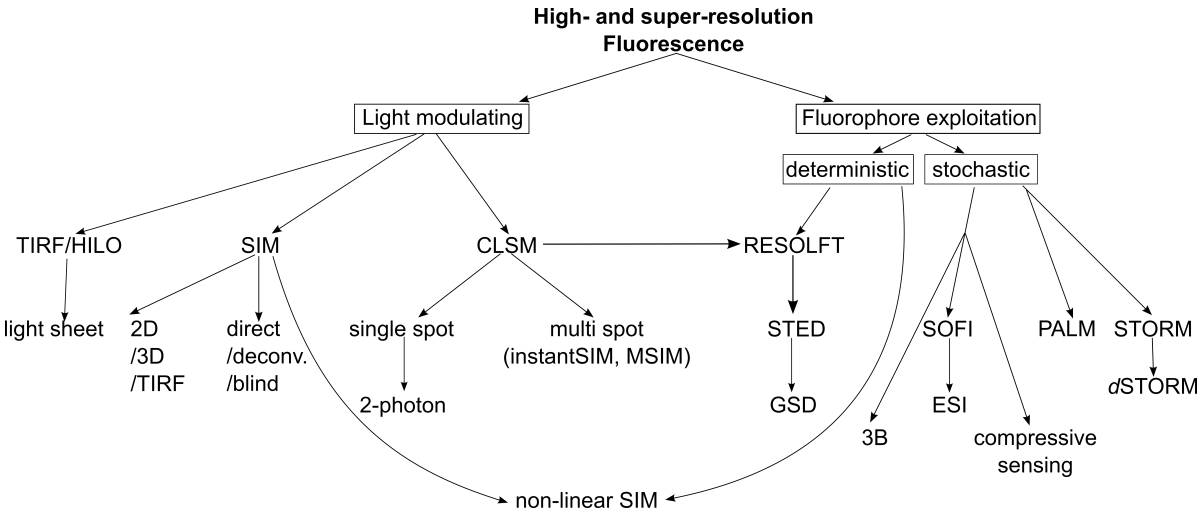

Figure 2.6.: Fluorescence microscopy can be divided into different technical subcategories. The two main approaches are to employ light modulation i.e. to change the even illumination of an epi-wide-field microscope and to exploit fluorophore properties, i.e. to introduce non-linearities in the amount of light a fluorophore emits. The latter approach can be used in a deterministic fashion (STED, RESOLFT) or stochastically (PALM, (d)STORM, SOFI).

and depend on the refractive indices and opening angle of the system. As interference always occurs due to the wave properties of light, resolution limits are fundamental and not only a technical limitation of the system. In the 19th century Abbe described the resolution limit with the formula [1]:

$$d = \frac{\lambda}{2nsin\alpha} = \frac{\lambda}{2NA} \tag{2.1}$$

Here the NA, the so-called numerical aperture, is a characteristic property of the objective (and immersion medium) in use. With a typical emission of 525 nm (excitation wavelength 488 nm) and using a high end oil immersion objective with a NA=1.42[1] the resolution is about 185 nm. This corresponds to the often quoted resolution limit of about 200 nm in wide-field microscopy.

The diffraction effects during imaging do not only set a fixed resolution limit. For a more in-depth understanding, the mathematical description of the imaging process can be used. The image $D(\vec{r})$, obtained on the detector (camera) of the microscope, is given by:

$$D(\vec{r}) = (E \otimes H)(\vec{r}) \tag{2.2}$$

where $\vec{r}$ is the spatial coordinate in sample space, E the samples light emission and H the point-spread-function (PSF). For fluorescence microscopy, E describes the photon density emitted by the fluorophores, and since this process is incoherent, H is the incoherent PSF and the imaging process is incoherent (independent of using a coherent light source, such as a laser, for excitation).

[1]such as the one employed by the 3D-SIM microscope in this thesis

The PSF $H(\vec{r})$ limits the resolution of the imaging system. It describes the light distribution of an ideal point source imaged onto the detector, which is not a perfect point, but an extended structure due to the unavoidable interference effects in the optical system. It follows the form of an airy pattern (see Figure 2.7 (a) and 2.14), given by a Bessel function [37]:

$$I(\frac{r}{q}) = \frac{J_1(\frac{2\pi}{\lambda} a \frac{r}{q})}{\frac{2\pi}{\lambda} a \frac{r}{q}} \tag{2.3}$$

where a is the radius of the aperture, r the radius coordinate in the spatial observation plan, q the distance between the aperture and the observation plane and λ is the wavelength.

The convolution operation $E \otimes H$ is generally not invertible, i.e. there is no way to calculate the full E from D. This becomes obvious when switching to frequency space (a basis transformation), where the convolution $E \otimes H$ becomes a multiplication:

$$\tilde{D}(\vec{k}) = \tilde{E}(\vec{k}) \cdot \tilde{H}(\vec{k}) \tag{2.4}$$

The optical transfer function (OTF) $\tilde{H}(\vec{k})$ now describes the frequency response of the optical system, and thus encodes the reduction in contrast for higher frequency structures, and the resolution limit as a cut-off frequency k_{max} where the OTF becomes zero ($\tilde{H}(|\vec{k}| > k_{max}) = 0$) (see Figure 2.7 (b)).

3D imaging

When imaging a biological sample in epi-fluorescent wide-field illumination, typically not only structures in the focal plane contribute to the signal, but also fluorescence that is generated above and below the focal plane as the whole sample volume receives excitation light.

These out-of-focus contribution appear as a blurred signal, as they are not imaged with a in-focus PSF, but with a defocus offset dependent on their axial position. Mathematically this can be described by extending equation 2.2 to 3 dimensions, i.e. by introducing a 3D PSF (and subsequently, a 3D convolution).

Its axial component is generally more complex (depending on immersion media, glass interface distance and NA), and can either be measured or obtained by numerical simulations.

Deconvolution

By scanning through a sample along its z-axis, and acquiring multiple images at different z-positions, a stack can be created where each fluorophore is ideally imaged in-focus ($z = z'$) as well as contributing to other focal planes as out-of-focus signal ($z \neq z'$). The resulting, 3 dimensional signal $D(\vec{r})$ can now be 'unblurred', i.e. estimated to only contain in-focus signal. This process is deemed *deconvolution*, as it partially reverses the convolution in equation 2.2. This can be achieved by switching to frequency space (equation 2.4) and dividing by $\tilde{H}(\vec{k})$. However, since $\tilde{H}(\vec{k})$ has regions $|\vec{k}| > k_{max}$ where

it is zero, a compensation has to be introduced, for example a Wiener-filtering step [38]. Alternatively, a popular iterative numerical algorithm, the so-called Richardson-Lucy algorithm [39, 40] can be applied. This algorithm allows for resolution-limited OTFs and will converge to the most likely signal, even when $D(\vec{r})$ contains shot noise. It is thus very popular, especially for axial deconvolution.

Shot noise

The cameras used to detect the signal $D(\vec{r})$ have a pixelated structure where each pixel electronically counts the number of photons emitted from the corresponding part of the sample[2]. With modern EMCCD and sCMOS cameras these photon counts are rather precise, but an important factor is the quantized nature of light. During the time of the measurement the pixel only captures a limited discrete number of photons N. This number is the result of a Poisson process of the photon intensity $D(\vec{r})$, which thus is only estimated by the photon count. This introduces a fundamental uncertainty into the measurement which scales with $\sqrt{N}$. With modern day cameras this is the dominating uncertainty named *shot noise* (first described in [41]).

Both the Wiener-filtering step and the Richardson-Lucy-deconvolution are adaptions of the deconvolution process to deal with a signal containing shot noise.

Resolution of deconvolved signals

It is important to note that a deconvolution step cannot improve the overall resolution of a microscope, as no cut-off in $\tilde{H}(\vec{k})$ can be changed and all frequency re-weighting comes at the cost of changing the signal-to-noise levels.

However, deconvolution can - sometimes drastically - improve image contrast and lead to a cleaner image that is easier to interpret (see Figure 2.7). Also 'simpler' resolution estimates such as the width (FWHM) of point-like emitters or thin structures are changed by the deconvolution, so a resolution estimate obtained by those means increase.

2.2.2. Confocal laser scanning microscopy

A schematic image of a Confocal Laser Scanning Microscope (CLSM) setup is depicted in Figure 2.8. In contrast to the wide-field setup the beam is focused on the sample and galvanometric mirrors are used to raster both illumination and detection on the sample. Furthermore it uses a pinhole to discard a part of the emitted out-of-focus light to decrease the detected volume to about 1 fl before hitting the detector (PMT). This leads to less background and better contrast in the resulting fluorescence image, as the unwanted fluorescence light from areas above or below the analyzed focus are rejected [42]. This also enables the observation of thick specimens and increases the resolution up to a factor of $\sqrt{2}$ [43].

By increasing the pinhole size more photons can be collected and by decreasing the pinhole size the lateral and axial resolution increase. For a nearly closed pinhole the

[2]This is typically mapped to a region of (80 nm)^2 to (120 nm)^2

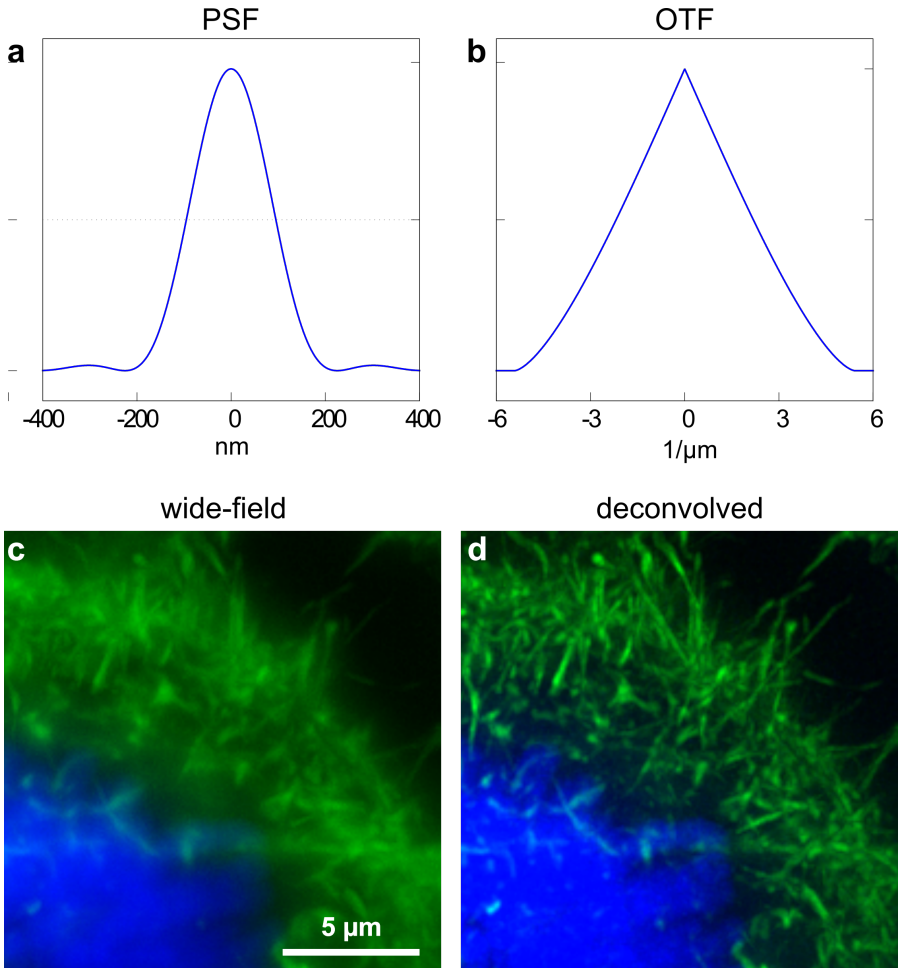

Figure 2.7.: Lateral point-spread function (PSF) (a) and its Fourier transformation, the optical transfer function (OTF) (b), for 525nm emission wavelength (488nm excitation) and a 1.42 NA objective (as used by the OMX v4). The frequency cut-off is at 5.41 μm^{-1}, i.e. no higher spatial frequency can be measured by the instrument. This corresponds to the Abbe limit of 185 nm.
The dotted line indicates the full-width-half-maximum of the point-spread function, the width where the signal of a point emitter has dropped of to half its intensity. This measure is often used as a simple indicator for resolution.
These theoretical plots assume a completely aberration-free instrument, where the resolution is only limited by a circular aperture in a Fourier plane of the light path (akin to the NA).
A deconvolution step can be used to change the medium frequency response, e.g. for structures around 3 μm^{-1} in size. It is most often used for the axial component of the signal ("background suppression"), but can also be applied laterally. It vastly improves image contrast in a physically valid way (compensating for the known instruments response curve). It also changes the FWHM of point emitters (since the PSF is modified), which suggest a resolution improvement when using FWHM as a resolution indicator. However, as the OTF cut-off is a property of the instrument, it cannot be changed by deconvolution in post-processing.
(c) and (d) show a U2OS cell stained for actin (Phalloidin Alexa 488) and nucleus (DAPI). (c) is the wide-field and (d) the corresponding deconvolved image. (Maximum intensity projection of an 21 µm stack).

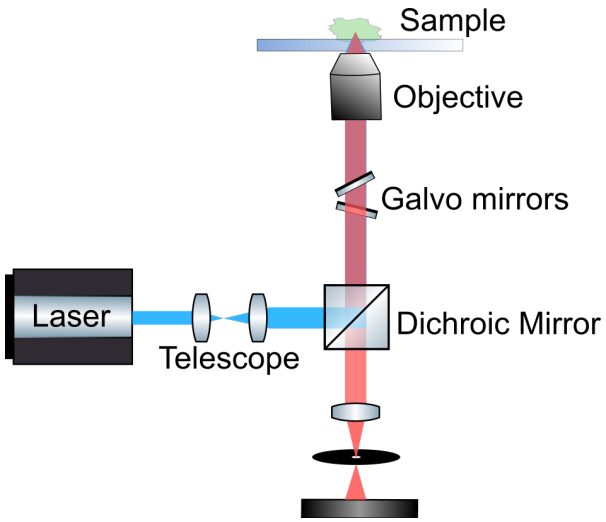

Figure 2.8.: The confocal setup scans the concentrated beam through the sample and rejects the out of focus light with a pinhole in the emission path. It increases the lateral resolution $\sqrt{2}$-fold, and greatly reduces background. It can be enhanced to acquire fluorescence spectra, to image with fluorescent lifetime information, or to built a STED/GSD/RESOLFT microscope. However, as a scanning technique, its speed is limited.

resolution reaches an improvement of $\sqrt{2}$ over a wide-field imaging system, when the full-width-half-maximum (FWHM) of a point emitter is used as a resolution criteria. In the case of an almost fully closed pinhole, most of the in-focus signal is discarded.

Scanning point by point makes this technique slow compared to a wide field microscope. There are several techniques of paralleled confocal approaches such as Spinning Disc Confocal Microscope [31] and Multifocal Structured Illumination Microscopy (MSIM) [44].

2.2.3. Two-photon excitation microscope

The two-photon excitation microscope setup is comparable to a confocal setup as seen in Figure 2.8. With a strong, focused laser it is possible to use two photons with low energy to excite a fluorophore. This principle is shown in Figure 2.9. To excite an electron from the ground state S_0 to the higher energy state S_1 a certain amount of energy $E = \frac{h \cdot c}{\lambda}$ is necessary to overcome the difference, that is often specified by the absorption wavelength of the fluorophore for a one-photon process (green). In the case that two photons with lower energy (dark red) arrive at the same time and are able to excite the electron in a two-photon process. This introduces a non-linearity, as the probability for this process scales with the laser intensity square I^2. The emitted photon (red) has a shorter wavelength than the excitation laser.

To enable a simultaneous arrival of the photons a very high photon density is required. This is only fulfilled for mode-coupling, pulsed laser (e.g. the often applied Ti-sapphire laser uses pulse width of 100 fs).

Due to the non-linearity of the process the emission volume is much smaller than

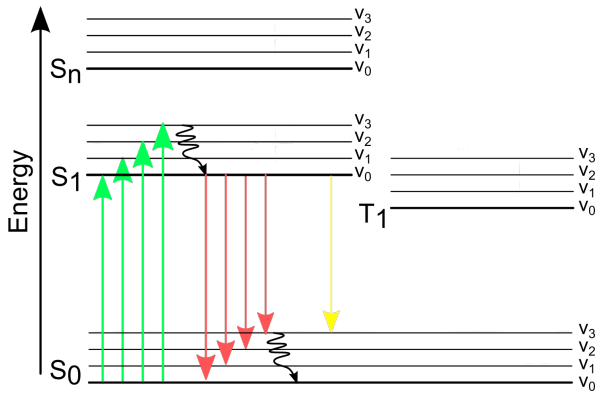

Figure 2.9.: Two-photon process: 2 low energy photons exciting the electron and emitting a higher energy photon possible

in confocal microscopy. This results in a better axial resolution without the need of a pinhole. Furthermore the longer laser wavelength used is less phototoxic and increases the penetration depth up to several 100 µm. This technique is thus often used for imaging tissue.

2.3. Photon-reassignment microscopy

There are several approaches to improve confocal microscopy in terms of speed and resolution, such as image scanning microscopy (ISM) [45]. In ISM the laser beam is scanned over the sample and imaged for each position. These raw images are then compressed with a factor 0.5 before being combined to the high-resolved image. This scanning point per point technique slows this imaging method down. The challenge is capturing higher-resolution images very fast.

Multifocal SIM (MSIM) generates multiple excitation foci by using a digital mirror device (DMD) to parallelize this approach [44]. The foci pattern is imaged by a sCMOS camera, digitally pinholed and scaled by 0.5 before summing up the raw data images with shifted foci patterns to a high-resolved one. This technique still suffers from speed, due to the need of several hundreds of raw images.

The multi-focal approach called instant structured illumination microscopy (iSIM) from York et al. in 2013 [17], claims a lateral resolution of 145 nm at 100 frames per second. The iSIM uses an optical approach for the 0.5 fold scaling and summing up of the foci. The original setup is seen in Figure 2.10. A microlens array generates the multi-spot excitation that is focused on the sample. The emitted light passes a pinhole array that rejects the out-of-focus light as in an conventional confocal microscope. To reach a twofold contraction of the spots a second microlens array is in the emission path, which decouples scanning and de-scanning magnification as described in the confocal re-scanning approach [46]. The compressed and pinholed spots are focused on a sCMOS camera. The multi-focus spots are scanned over the sample by one galvanometric mirror to raster the whole area. The backside of the same galvanometric mirror is used

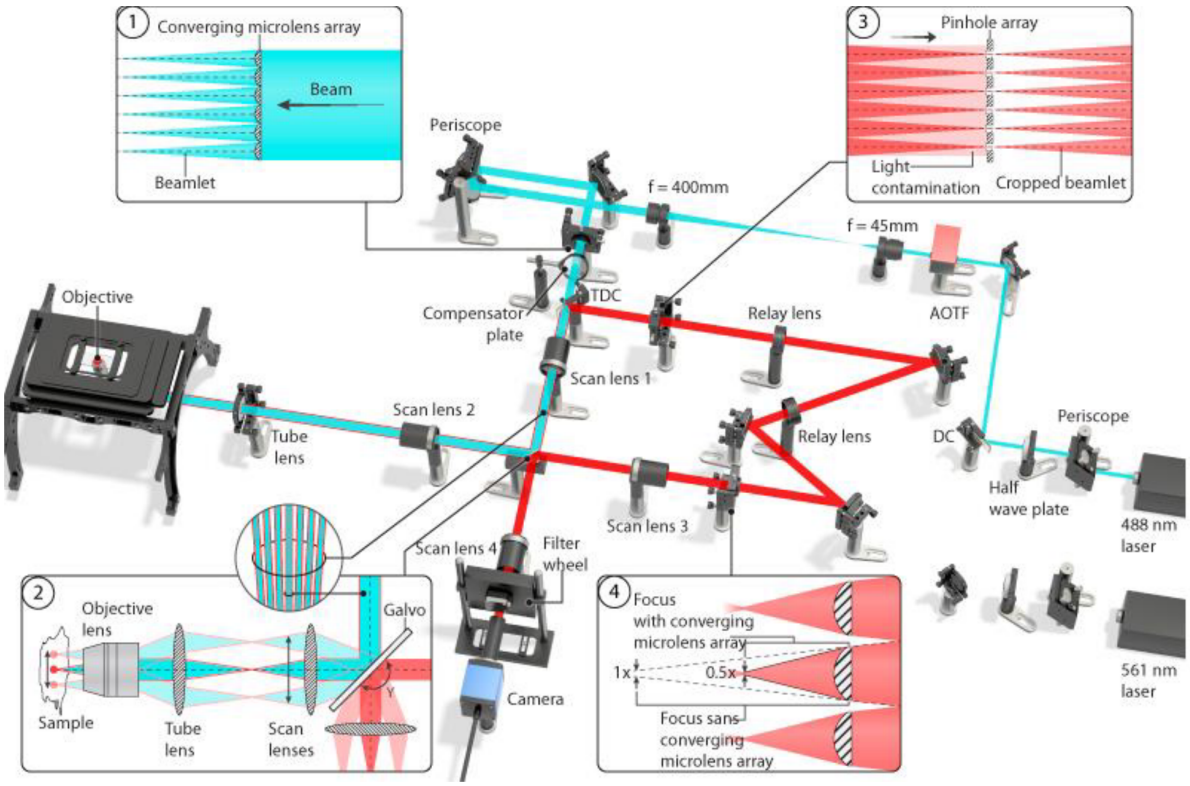

Figure 2.10.: Overview of the original instantSIM setup: The insets show the important components. From the light source to the detector, at first (1) a microlens array forms a multiplicity of excitation foci which are scanned by a galvo-mirror over the sample (2). The pinhole array rejects the out-of-focus emission. Before the foci are rescanned onto a sCMOS camera the second microlens array serves as a twofold contractor for each focus. Taken from [17]

to scan the emitted light over the camera. These scans occur several times during one acquisition step. This means in every frame the sum of the pinholed and concentrated foci are already summed up and give an image with a $\sqrt{2}$ fold resolution. An additional deconvolution step is the final improvement to gain the claimed twofold resolution enhancement. Combining the steps of ISM in a multifocal and optical way makes this imaging technique very fast, which makes it very attractive for biological applications.

This technique was tested to analyze the biological samples discussed in this thesis (see chapter 3.1 and 8). Furthermore the possibility to improve this by combining it with 2-photon microscopy would be of great interest for deep tissue imaging.

Airy-detector technique

As mentioned in chapter 2.2.2 in a confocal microscope the adjustment needs to be arranged by making a compromise between resolution and brightness. Current-generation confocal microscopes employ a segmented single-photon-sensitive detector array instead of a point detector and pinhole. Thus, in these instruments the resolution improvement does not impair the signal level and they otherwise then serve as an improved replacement for a confocal system. The Zeiss 'LSM 880 Airyscan' is a popular commercially

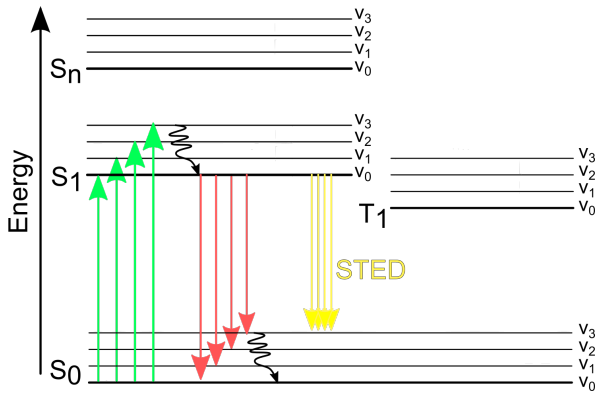

Figure 2.11.: The Jablonski diagram shows the STED process: By using a second laser with a certain STED wavelength the excited fluorophore can be brought back to the ground state by stimulated emission (yellow arrows). The STED wavelength is chosen long enough to not excite the fluorophore (i.e., longer than $S_0V_0 \rightarrow S_1V_0$), but short enough to still be able to detect the bulk of the fluorescent spectrum after filtering out the STED illumination (i.e., shorter than $S_1V_0 \rightarrow S_0V_n$ for low n, red arrows).

available system employing this *'Airy-detector'-technique*.

2.4. Optical super-resolution microscopy

Since biology occurs below 200 nm, methods were developed to circumvent this limit. In 2014 the Nobel Prize in Chemistry was awarded jointly to Betzig, Hell and Moerner 'for the development of super-resolved fluorescence microscopy' [2].

2.4.1. Stimulated emission depletion (STED)

The STED microscopy was invented by Hell et al. 1994 [3] and experimentally realized 1999 [47]. Comparable to confocal microscopes described in chapter 2.2.2 the focused laser beam is scanned over the sample and the spontaneous light is detected by a single-photon sensitive detector (Photoelectron Multiplier Tube (PMT) or Single Photon Avalanche Diode (SPAD)).

The resolution is determined by the diffraction limited focus size of the beam that is used to scan the sample. To enhance the resolution in scanning techniques the probe (e.g. the tip in an AFM) needs to be as small es possible. By taking advantage of fluorophore properties this is possible to reach for the focus laser by deep depletion. An excited fluorophore can be brought back to the ground state by a stimulated emission (see Figure 2.11). This is done by using a second laser with a higher wavelength (yellow arrows) than the excitation wavelength (green arrows) to avoid exciting the molecule, but shorter wavelength than the bulk of the fluorescent emission spectrum (red arrows). The fluorescence light (red arrows) can then be separated from the stimulated emission wavelength by an optical filter with a sharp cutoff in transmission (few nanometers band width). The principle of STED is shown in Figure 2.12. (a) shows the excitation focus

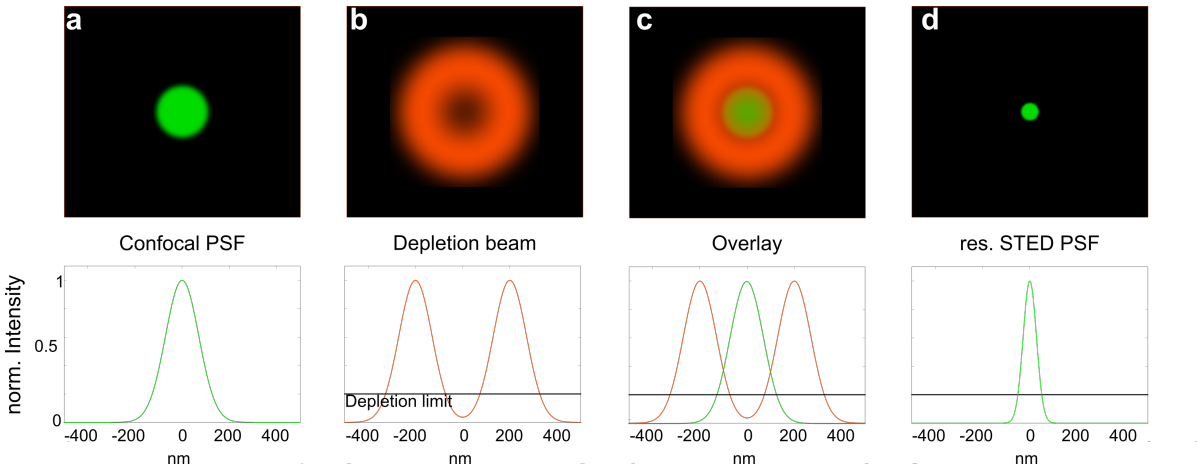

Figure 2.12.: Principle of STED: The excitation focus (a) is overlayed (c) with the STED beam (b). Depending on the STED beam intensity the resulting focus size is decreased (d). In the bottom row the according intensity profiles are shown. The depletion limit (black line) describes the cut-off at almost full depletion.

comparable to a confocal microscope (top) and the according intensity profile. By using a doughnut shaped beam for depletion as seen in (b) the fluorophores in this area do not contribute to the filtered fluorescent signal anymore. The probability for this effect is higher with increasing the intensity of the STED beam. In (c) the overlay shows the overlap of both beams. There is a depletion limit (black line) is a cut-off at (almost) full probability on the STED transition. This means the fluorophores in this area of the doughnut (almost) all undergo stimulated emission and thus are not detected as signal. Only a small area in the middle is available for spontaneous emission. This leads to a smaller effective focus area for the excitation beam as seen in (d). The resolution of this technique can be defined by a variation of the Abbe limit where I_{STED} is the intensity of the STED beam and $I_{\mathrm{sat.}}$ is the depletion limit where the probability of the fluorophores for stimulated emission approaches 1:

$$d = \frac{\lambda}{2NA \cdot \sqrt{1 + \frac{I_{STED}}{I_{sat.}}}} \tag{2.5}$$

Theoretically there is no limit to the resolution if I_{STED} can be chosen high enough. Proof-of-concept experiments performed on highly photostable nanodiamonds show a resolution of about 2 nm. However in reality too high I_{STED} destroy the biological samples even for modest resolutions. Often about 50 nm resolution is gained for relevant samples.

Instead of using the stimulated emission process, the depletion can also occur by moving the fluorophores into the triplet state (Ground State Depletion, GSD). The realization of this method depends on the fluorophore properties. The advantage is that less intensities for the STED-beam can be used, but it is also slower due to the transition time of the fluorophores back to the on-state. In RESOLFT-microscopy (REversible Saturable OpticaL Fluorescence Transitions) switchable proteins are used that undergo

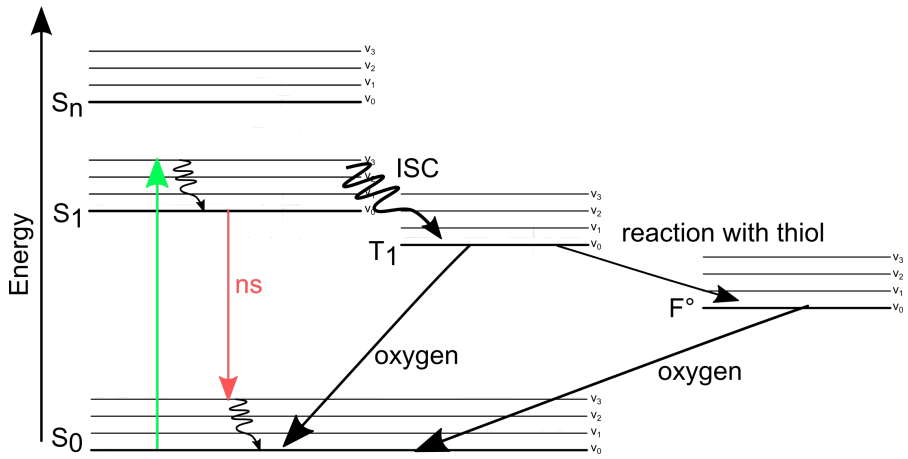

Figure 2.13.: The Jablonski diagram show possible processes during *d*STORM. The absorption excites the fluorophore from the ground singlet state S_0 to the first excited singlet state S_1 (green arrow). The dye then either fluoresces within ns or it can also enter the long-living triplet state T_1. T_1 can either react with oxygen to repopulate the ground state or react with thiol to become a fluorophore radical F°. F° can also react with oxygen to repopulate S_0. According to [51]

a conformation change that leads to a dark state [48].

2.4.2. Single molecule localization microscopy based techniques

Single molecule localization microscopy (SMLM) based techniques such as STORM [5], *d*STORM [49] ((*direct*) stochastical optical reconstruction microscopy) and PALM [4] (photoactivated localization microscopy) can achieve resolutions down to 20 nm and even smaller localization precisions. These methods are dependent on the sample preparation, they require photoswitchable / photoconvertable dyes and in the most cases a special buffer environment. The idea is to separate the fluorophores in time that are inseparable in space with conventional microscopy approaches. In contrast to the beam shaping techniques the setup is comparable to a simple wide-field setup (as shown in Figure 2.4) with a single-photon sensitive camera (EMCCD or sCMOS [50]) and (for *d*STORM) a powerful light source.

The Jablonski diagram in Figure 2.13 explains the process of photoswitching during the *d*STORM-process. With increasing excitation light higher numbers of electrons undergo the fluorescence process and cycle between the ground and the first excited state. The probability to reach the 'forbidden' triplet state also increases and a certain percentage of the excited electrons will relaxate to this 'off state'. The life time of an electron in the off state is long (µs to s) compared to the time of the fluorescence process (ns). During this time these electrons cannot participate in the fluorescence process anymore and the fluorophore remains dark. A thiol reaction quenches the dye and enhances the off time while oxygen reactions lead to a repopulation of the singlet state. To support the switching probabilities the typical switching buffers consist of an oxygen scavenging system (OSS) and a thiol, such as cysteamine, for quenching.

The probability for a transition to the triplet state is for example dependent on the

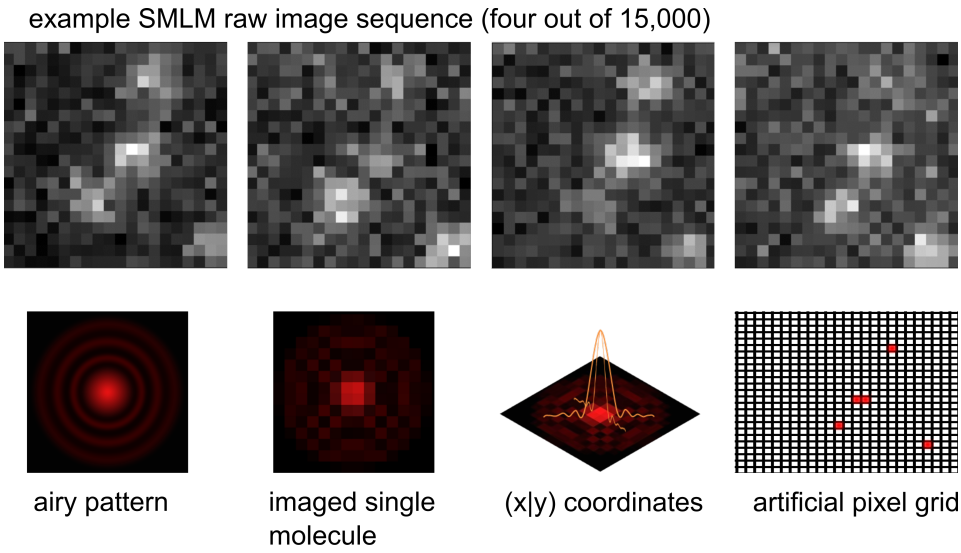

Figure 2.14.: A single emitter is seen as a broadened spot, which can be fitted by a 2D point spread function. The center of this mathematical function can be localized very well and the position can be transferred to an artificial pixel-grid (red spots).

buffer composition (thiol concentration), pH and laser intensity [51]. In many fluorophores the life time of the triplet state can be decreased and by that the fluorophores 'reactivated' with additional excitation with 405 nm (in some also 488 nm) light. This is useful for adjusting the photo-switching behavior during a measurement. An example of a series of raw images from a *d*STORM experiment (seen in Figure 4.1) is shown in the upper row in Figure 2.14. These ROIs are from a densely stained membrane excited with high laser intensities and therefore the main part of the fluorophores are in the off state and remain dark.

For analyzing the data rapidSTORM, a free and open-source localization microscopy software package developed by Steve Wolter in the Sauer lab [52] is used for the main part of the shown data in this thesis. Nowadays there are many free available SMLM softwares [53], even implemented as imageJ plugins such as ThunderSTORM [54].

After noise reduction the subset of fluorophores in the on state can now be separated. The emitters are seen as point sources and the emitted light is assumed as airy pattern distributions (Figure 2.14 bottom left). The imaged molecule is pixelated due to the certain pixel size[3] of the EMCCD camera used for this experiment, and show photon shot noise due to the typical number of photons acquired per molecule (1,000-10,000).

The single objects in each raw image are detected by the software and fitted with a two dimensional Gaussian to the individual PSFs as an approximation for the airy disk:

$$f(x,y) = \frac{A}{2\pi\sigma_x\sigma_y} exp\left(-\frac{1}{2}(\frac{(x-x_0)}{\sigma_x})^2 - \frac{1}{2}(\frac{(y-y_0)}{\sigma_y})^2\right) + B \tag{2.6}$$

A defines the amplitude, B the background, x_0, y_0 the center and σ_x^2, σ_y^2 are the spreads of

[3]The ideal pixel size can be calculated by minimizing the localization precision r (LHS of eq. 1.3) with respect to a. A set of ready-made plots can be found in [55, 56]

the localization [57]. The center coordinates of each so-called localization are stored with additionally information such as the number of emitted photons, localization precision and width of the fit. These parameters can later be used to filter the reconstructed image. In the reconstruction an artificial pixel grid with a selectable pixel width is generated. For example a suitable pixel width of *d*STORM image is the mean localization precision of the measurement. The localizations will be sorted by corresponding coordinates to the pixels and the brightness can be correlated to different properties (e.g. the detected events, localization accuracy, brightness of each emitter,...). The result is a 2D histogram of localizations that represents the super-resolved image.

The resolution depends on the localization precision and the fluorophore density in the stained sample. The localization precision depends on the number of collected photons N due to the shot noise of the camera and the FWHM of the PSF Δ_{PSF}. The pixel size a and the background noise b are other important factors in calculating the possible localization precision [55]:

$$r_{loc} = \sqrt{\frac{\Delta_{PSF}^2}{N} + \frac{a^2/12}{N} + \frac{8\pi\Delta_{PSF}^2 b^2}{a^2 N^2}} \approx \frac{\Delta_{PSF}}{\sqrt{N}} \tag{2.7}$$

Therefore fluorophores with a high quantum efficiency and a camera with low readout noise are of choice. The effect of the labeling density is explained by the Nyquist-Shannon sampling theorem. It postulates that the density of the localized molecules must be at least twice as high as the desired resolution (assuming evenly distributed molecules, higher densities are needed if the distribution is assumed to be random). For example in one dimensional structures (such as actin/tubulin) if the desired resolution is 20 nm then the localization of a fluorophore has to be localized every 10 nm. In a 2D structure such as a membrane (see chapter 4) the required labeling density for 20 nm lateral resolution is 10,000 localizations per μm^2. In the area of a PSF with a diameter of 250 nm 600 fluorophores need to be localized [58](p.112). This value assumes an absolutely homogenous distribution of fluorophores and is therefore an optimistic lower limit.

When increasing the fluorophore density to meet the Nyquist-Shannon criterion, the switching conditions need to be adjusted, to avoid an increasing number of non-separated fluorophores. Additionally more raw data need to be acquired for the same amount of localizations or the software needs to be able to handle multi-emitter fitting (such as ThunderSTORM).

*d*STORM measurements are often acquired in Highly Inclined and Laminated Optical (HILO) or Total Internal Reflection Fluorescence (TIRF) illumination (see Figure 2.15). The laser beam passing through the objective is not centered, but it is shifted to the outer region. The laser beam is then reflected completely when laser light is directed to an interface (cover-glass) with a lower refractive index behind the interface (sample) and the angle of incidence is larger than $\alpha_{critical} = sin^{-1}(\frac{n_1}{n_2})$ (n_1): refractive index of the sample, n_2: refractive index of the cover slip). The sample is thus illuminated by an evanescent wave, i.e. with an exponential decreased intensity profile. This technique is therefore very surface sensitive (up to 200 nm deep in the sample) and has less background. The result is a higher localization precision in the *d*STORM measurements.

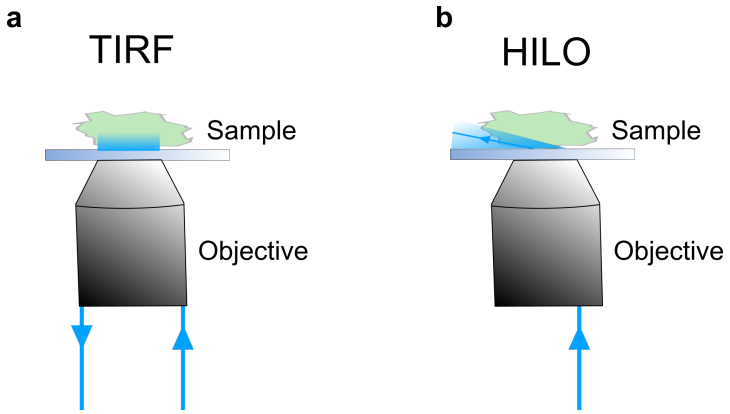

Figure 2.15.: In TIRF illumination the laser beam is shifted to the outer region of the back-focal plane and reflected completely at the coverslip. The sample is illuminated by an evanescent wave which intensity decreases exponentially within the sample. HILO is in-between EPI and TIRF and generates a light sheet with a higher photon density inside the sample.

HILO is in-between EPI and TIRF illumination (see Figure 2.15 b). The advantage of this is generating a light sheet with a higher photon density. This is needed for *d*STORM imaging as explained above.

2.4.3. Structured Illumination Microscopy

High resolution Structured Illumination Microscopy (SIM) is a wide-field microscopy approach employing spatial modulation of the excitation light to provide a two-fold resolution improvement. In contrast to *d*STORM and STED it does not rely on special properties of the fluorophores as it only requires a linear, incoherent response to excitation light intensity. The SIM process shifts the information in frequency space and by changing the phase and angle of the modulated light additional information from different areas of the k room can be collected. By merging the Fourier transformed raw data and subsequent back transformation an image with double resolution can be obtained.

Two dimensional SIM was first shown by Heintzmann [6] and Gustafsson [7] 1999/ 2000. In 2008 Gustafsson expanded the technique to three dimensions [59]. The theory behind the 3D-SIM technique will be described in the next section according to [59]. Mathematically a fluorescence image $D(\vec{r})$ can be described by a convolution of the light emitting object $E(\vec{r})$ with the PSF $H(\vec{r})$ of the imaging system

$$D(\vec{r}) = (E \otimes H)(\vec{r}) \tag{2.8}$$

Considering the object $E(\vec{r})$ as a structure with a certain density distribution of a fluorescent dye $S(\vec{r})$ excited with an illumination intensity $I(\vec{r})$, the E can be described as:

$$E(\vec{r}) = S(\vec{r}) \cdot I(\vec{r}) \tag{2.9}$$

With a linear response of the fluorophore S to the illumination light intensity I. Moving

to frequency space $\tilde{E}(\vec{k})$ becomes a convolution:

$$\tilde{E}(\vec{k}) = (\tilde{S} \otimes \tilde{I})(\vec{k}) \tag{2.10}$$

For a constant excitation illumination, as in wide-field, $\tilde{I}(\vec{k})$ would be a delta function at $\vec{k} = 0$ and $\tilde{I}(\vec{k}) = 0 \, \forall \vec{k} \neq 0$. However, an $I(\vec{r})$ varying along $\vec{r}$ leads to a non-local convolution operation and within $\tilde{E}(\vec{k})$ unobservable components of $\tilde{S}(\vec{k})$ become observable, if the information can be extracted (see Figure 2.16). In this case $I(\vec{r})$ has contributions at non-zero frequencies.

For arbitrary $I(\vec{r})$ $\tilde{I}(\vec{k})$ generally has (multiple) extended non-zero regions, and the equation 2.10 cannot be solved for $\tilde{S}(\vec{k})$ analytically in closed form, i.e. there is no direct calculation of S possible from E and I.

To directly solve eq. 2.10 for $\tilde{S}(\vec{k})$ the excitation illumination pattern must consist of a sum with a finite number of components, which are also separable into axial and lateral functions:

$$I(\vec{r_{xy}}, z) = \sum_m I_m(z) \cdot J_m(\vec{r_{xy}}) \tag{2.11}$$

I_m is a fixed pattern related to the focal plane of the microscope. J_m are simple harmonic waves in xy: $J_m = e^{i(2\pi p_m \cdot r_{xy} + \varphi_m)}$.

$$\begin{aligned} D(\vec{r}) &= (E \otimes H)(\vec{r}) && (2.12)\\ &= (S(\vec{r}) \cdot I(\vec{r}) \otimes H)(\vec{r}) && (2.13)\\ &= (S(\vec{r}) \cdot \sum_m I_m(z) \cdot J_m(\vec{r_{xy}}) \otimes H)(\vec{r}) && (2.14)\\ &= \sum_m \left[(H \cdot I_m(z)) \otimes (S) \cdot J_m) \right](\vec{r}) && (2.15) \end{aligned}$$

The mth component of 2.15 is gained by Fourier transformation for the frequency space:

$$\tilde{D}_m(\vec{k}) = O_m(\vec{k}) \left[(\tilde{S}(\vec{k}) \otimes \tilde{J}_m(\vec{k_{xy}})) \right] \tag{2.16}$$

The transfer function $O_m(\vec{k})$ is the Fourier transform of HI_m. The Optical transfer function $0 = \tilde{H}$ a complex valued and describes the strength and the phase of transformation of the object frequency $\vec{k}$ in the microscope. With J_m as a simple harmonic wave and by employing the shift theorem for δ-peaks, the measured data can be concentrated in equation 2.16:

$$\tilde{D}(\vec{k}) = \sum_m O_m(\vec{k}) e^{i\varphi_m} \tilde{S}(\vec{k} - \vec{p_m}) \tag{2.17}$$

The observed image $\tilde{D}(\vec{k})$ is a sum of copies of the object information which are moved in the k-space by $\vec{p_m} = m\vec{p}$, phase shifted by the phase φ_m and filtered by the transfer function O_m. Since eq. $\tilde{D}(\vec{k})$ contains the sum over the shifted sample information $\tilde{S}(\vec{k} - \vec{p_m})$, the so-called band separation step is used to extract the different contributions. It uses additional data sets $\tilde{D}_n(\vec{k})$ with different known values of the phase φ_m, but constant

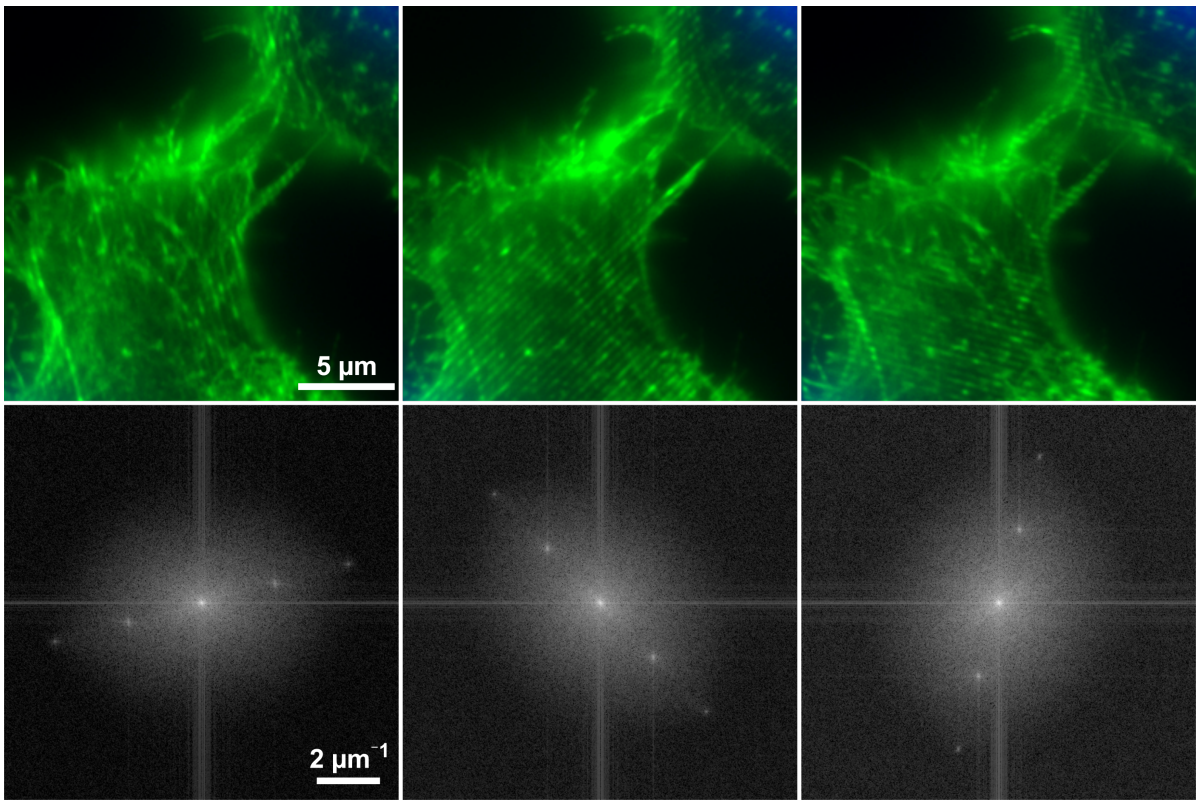

Figure 2.16.: Top row: raw images acquired with the 3D-SIM. The coarse illumination pattern J_m of different angle orientations can clearly be seen (ROIs of 20.5 x 20.5 μm^2). In the bottom row are the corresponding graphic representation of the Fourier transforms that show the additional information in the k-room.

pattern spacing and orientation $\vec{p_m}$. From these, eq. 2.17 can be written in matrix form, with components $M_{n,m} = e^{i\phi_{n,m}}$ and for three-beam illumination:

$$M \cdot \begin{pmatrix} \tilde{S}(\vec{k}) \cdot O_0(\vec{k}) \\ \tilde{S}(\vec{k}+\vec{p}) \cdot O_1(\vec{k}) \\ \tilde{S}(\vec{k}-\vec{p}) \cdot O_1(\vec{k}) \\ \tilde{S}(\vec{k}+2\vec{p}) \cdot O_2(\vec{k}) \\ \tilde{S}(\vec{k}-2\vec{p}) \cdot O_2(\vec{k}) \end{pmatrix} = \begin{pmatrix} D_1 \\ D_2 \\ D_3 \\ D_4 \\ D_5 \end{pmatrix} \tag{2.18}$$

For a set $n \geq m$ of equidistant phase steps in ϕ_n the matrix M becomes invertible and thus a set of measurement $D_{1...5}$ obtained under illumination with these phases can be used to extract $\tilde{S}(\vec{k})$, $\tilde{S}(\vec{k} \pm \vec{p})$ and $\tilde{S}(\vec{k} \pm 2\vec{p})$ as:

$$M^{-1} \cdot \begin{pmatrix} D_1 \\ D_2 \\ D_3 \\ D_4 \\ D_5 \end{pmatrix} = \begin{pmatrix} \tilde{S}(\vec{k}) \cdot O_0(\vec{k}) \\ \tilde{S}(\vec{k}+\vec{p}) \cdot O_1(\vec{k}) \\ \tilde{S}(\vec{k}-\vec{p}) \cdot O_1(\vec{k}) \\ \tilde{S}(\vec{k}+2\vec{p}) \cdot O_2(\vec{k}) \\ \tilde{S}(\vec{k}-2\vec{p}) \cdot O_2(\vec{k}) \end{pmatrix} \tag{2.19}$$

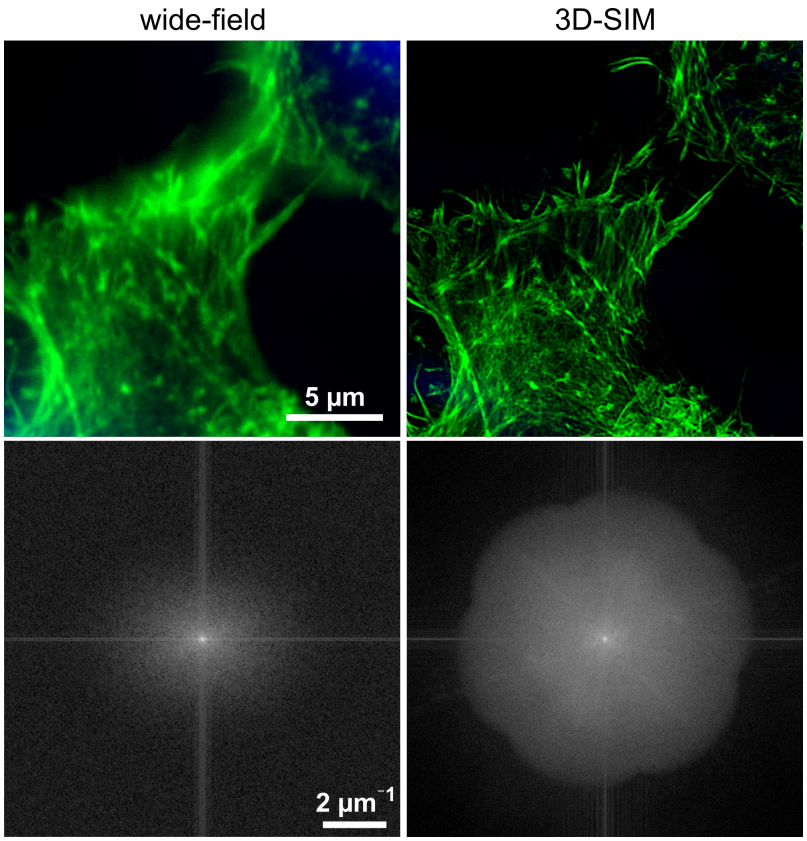

Figure 2.17.: Top row: micrograph images acquired with the 3D-SIM in wide-field mode and 3D-SIM mode. Bottom row: corresponding frequency space, shown as power spectra of the Fourier transformations obtained from the top row. In this visualization, the low frequency components are centered, high frequency extend to the sides of the image. The strength and cut-off of these high frequency components are an indication of the resolution archived by each method.

With the optical transfer function $O_{0,1,2}$ and the known orientation and frequency of the illumination pattern $\vec{p_m}$, the separated bands $\tilde{S}(\vec{k})$ can be shifted to their correct positions in k-space, OTF compensated and merged into a single extended resolution image as shown in the example in Figure 2.17.

3D-SIM pattern generation

The commercial microscope used in this thesis is a DeltaVision OMX V4, a 3D-SIM, using three-beam illumination to generate the pattern in xyz. A simplified schematic of a 3D structured illumination excitation path can be seen in Figure 2.18. The laser beams are diffracted from a grating and focused to the edges of the objective back focal plane. Since three coherent beams, the two side beams, and a central beam, each interfere with each other, this creates a pattern with both lateral and axial components. An exemplary axial view of three-beam intensity pattern is seen in Figure 2.19 k. Figure 2.19 explains the advantage of this illumination strategy. Using a two-beam illumination would result in three shifted copies (Figure 2.19 c) of the conventional 3D-OTF that is seen in Figure

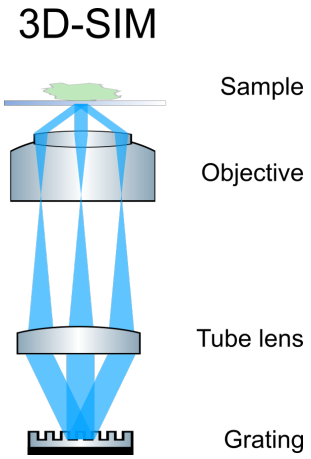

Figure 2.18.: Schematic of a 3D structured illumination excitation path. The beam is diffracted from a grating resulting in three foci in the edges of the objective back focal plane. The three beams are needed to create a pattern with both lateral and axial components.

2.19 a,b. The result is a lateral resolution enhanced image however the axial resolution is suffering from the *missing cone problem* conventional microscopy does. In contrast the three-beam illumination generates a three-dimensional illumination pattern according to Figure 2.19. This leads to an expanded observable region in $\vec{k}_z$ (Figure 2.19 d and i). Using different pattern orientations by rotating the angle of the pattern also eliminates the missing cones of the top and bottom OTFs (Figure 2.19 e and j).

The factor $f_{\text{res.}}$ of resolution improvement over a wide-field microscope can be calculated by:

$$f_{res} = \frac{\lambda_{Abbe} + \lambda_{SIM}}{\lambda_{SIM}} \tag{2.20}$$

$$= \frac{\frac{\lambda_{em}}{2NA} + \lambda_{SIM}}{\lambda_{SIM}} \tag{2.21}$$

Therefore the resolution enhancement is better for smaller wavelength of the illumination pattern. As this pattern is generated by coherent interference as explained in Figure 2.18, its minimum wavelength depends on the same angle and refractive index considerations as the Abbe limit and $\lambda_{SIM} = \frac{\lambda_{em}}{2NA}$ is the smallest possible wavelength. This yields the often-quoted two-fold resolution improvement, as:

$$f_{res} = \frac{\frac{\lambda_{em}}{2NA} + \frac{\lambda_{em}}{2NA}}{\frac{\lambda_{em}}{2NA}} \tag{2.22}$$

$$= 2 \tag{2.23}$$

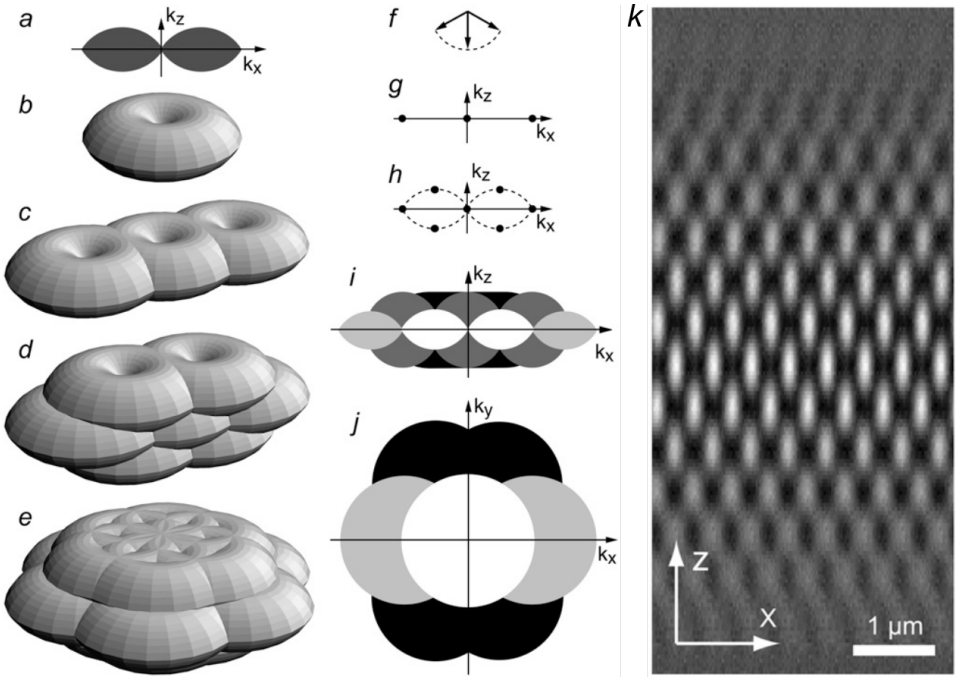

Figure 2.19.: OTF representation in SIM for a conventional microscope a, b and for different types of SIM illumination: two-beam illumination (c, h), three-beam illumination with one (d, i) and with three pattern orientations (e, j). (k) axial view of three-beam intensity pattern. Adapted from [59]

3. LSECs - Liver Sinusoidal Endothelial Cells

The liver plays an important role in storing nutrients and fats and furthermore in drug metabolism. To fulfill this function the liver is well supplied by a branched network of blood vessels (see Fig. 3.1 a and b) [60]. The hepatic sinusoids separate the blood from the hepatocytes and act as permeable functionalized barrier. The walls of this barrier are formed by liver sinusoidal endothelial cells (LSECs). These cells are highly specialized and have unique morphology and functions. They contain numerous transcellular pores with diameters of 50 - 200 mm that cannot be analyzed by conventional optical microscopy. Furthermore, the preparation while maintaining these fine morphological structures for the imaging process is difficult which is exemplified in this chapter.

3.1. Function and morphology

Since the 1950s, LSECs were analyzed by electron microscopy techniques [61, 62] such as transmission electron microscopy (TEM) and scanning electron microscopy (SEM) to visualize their morphological substructures. Discontinuities in the membrane have been observed, however, they were thought to be artifacts. In the 1970s, Wisse used improved fixation protocols and was able to describe the ultrastructure of LSECs in detail [10, 63]. LSECs contain numerous pores that can be seen in Fig. 3.1 c. These so-called *fenestrations* are spread in the membrane with diameters of 50-200 nm. They are arranged in groups and form *sieve plates* that have several µm extent.

Compared to other endothelial cells LSECs have a high endocytic capacity and contain receptors for endocytosis [64]. This enables them to act as scavengers for waste macromolecules and nanoparticles in the body. They also regulate the sinusoidal blood flow, have an important role in triggering liver regeneration and are know to have unique immune functions compared to other endothelial cells, due to expressing various pattern recognition receptors [64], scavenger receptors [65] and toll-like receptors [66]. The affinity for endocytosis made it difficult to find a suitable membrane stain for live LSECs. For instance ULEX is endocytosed before the membrane could be stained (chapter 6.2.1, Fig. 6.4). Mammalian LSECs fulfill similar functions and have a similar morphology as LSECs in birds, reptiles and amphibians [67]. The experimental studies in this thesis are limited to rat LSECs with exception of chapter 3.2.

Isolated LSECs have a smooth surface and are about 150 nm to 170 nm thick [68] (excluding the nucleus). This makes them an ideal sample for *d*STORM imaging due to

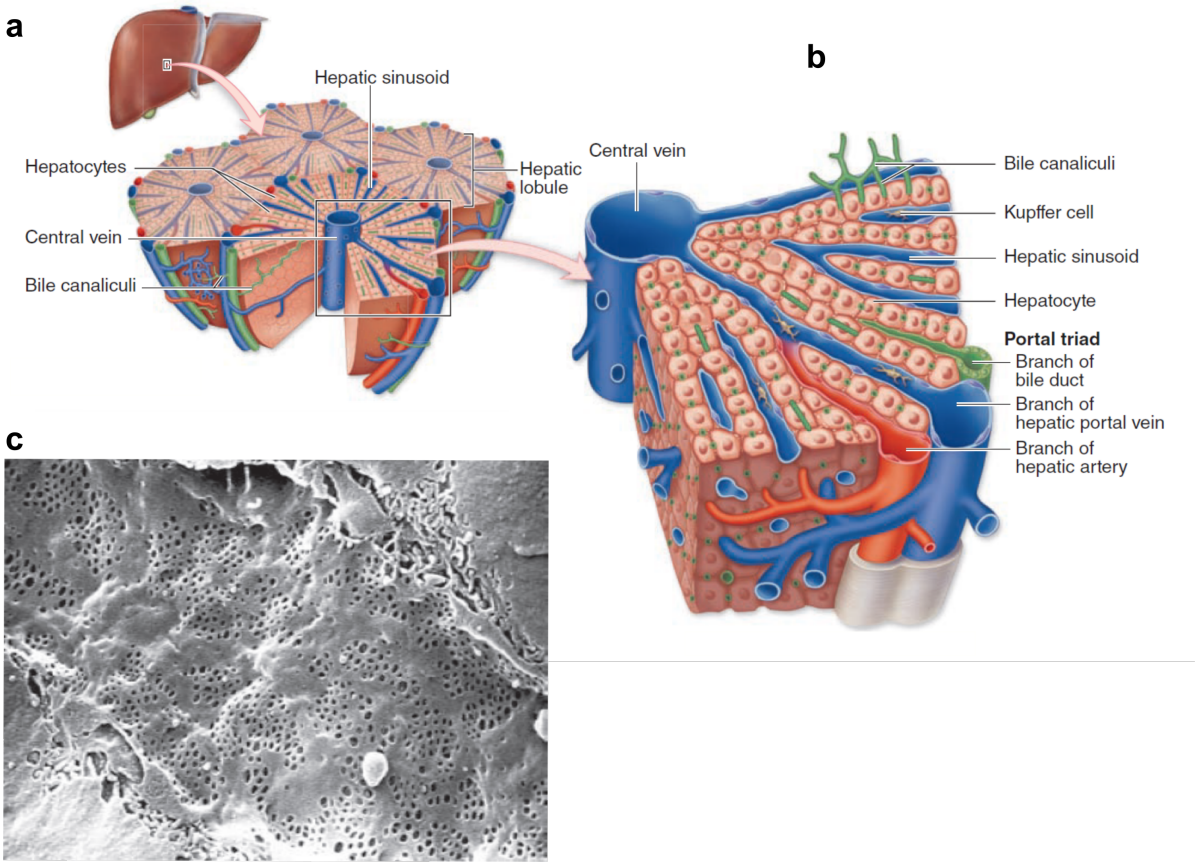

Figure 3.1.: The liver is well supplied by a branched network of blood vessels (a). The hepatic sinusoids separate the blood from the hepatocytes (b). The SEM image shows the luminal surface of the endothelium. It reveals the morphological substructure of liver sinusoidal endothelial cells, which are highly fenestrated (c). Adapted from [60] and [8]

the illumination configuration close to TIRF (HILO) (see chapter 4). Rat LSECs have a round shape with a diameter of about 35 µm. They contain plenty of fenestrations which can also be described as 'nanopores'. In contrast to other porous cells, they are lacking a diaphragm [10]. Without a basal lamina, colloids and solutes inside the blood can directly pass through the endothelium to the space of Disse. This means the semipermeable barrier of the fenestrated endothelium acts as a dynamic selective sieve for lipoproteins, virus particles, soluble molecules and other nanoparticles with diameters below the fenestration diameter, while it is excluding bigger particles such as blood cells [69]. This bidirectional exchange also allows a direct interaction of microvilli of the hepatocytes with e.g. lymphocytes [70].

Changes in diameter and number of fenestrations play an important role in the susceptibility to atherosclerosis, because the lipoprotein traffic between liver and blood is influenced by the porosity of LSECs. Reduced porosity often found in liver cirrhosis, old age and diabetes mellitus is linked to the presence of excessive lipoproteins and an increased cholesterol level in the blood [71]. These are well-known atherosclerosis risk

factors. The number and diameters of fenestrations are depending on age [72], species [69], environmental influences [8] and method of visualization [8, 73]. The method of visualization is influencing the measured diameters of fenestrations. Ten years ago TEM and SEM were the only techniques available to visualize the substructures. While the measured diameters in TEM vary from 150 to 175 nm, the diameters of fenestrations imaged with SEM vary from 105 to 110 nm [8]. This was explained by sample preparation which leads to tissue shrinking. The extensive sample preparation in both techniques can easily lead to artifacts. Optical microscopy did not have the needed resolution for a long time, but this technique uses wet cell preparations which avoids the shrinking and other preparation artifacts of EM methods. The first observations of fixed fenestrations with an optical microscope were shown in 2010 [11, 12]. Cogger et al. used 3D Structured Illumination Microscopy (3D-SIM) for imaging the membrane of LSECs and found diameters of 123 ± 24 nm. This technique is described in chapter 2.4 and also used in this thesis. In chapter 4 I will show that single molecule localization microscopy visualizes fenestrations and reveals diameters of about 120 ± 38 nm [13].

The fenestrations are dynamic structures which change due to e.g. drugs, toxins, diseases and aging. Toxins and diseases can affect defenestration that leads to hyperlipoproteinemia [74]. Especially substances effecting the actin cytoskeleton such as the actin disruptor cytochalasin B have huge effects on the fenestrations [75]. Actin and tubulin are known to play an important role in forming or stabilizing the pores by forming a cytoskeleton ring [76]. Due to lacking spatial resolutions so far and the slow speed of the super-resolution techniques it was not possible to image live fenestration dynamics up to now (see chapter 7.1).

3.2. Human LSECs in 3D-structured illumination microscopy

Human LSECs seem to have a different morphology compared to murine and rat LSEC. The human LSECS we analyzed were provided by our collaborators at UiT through a collaboration with a hospital in Stockholm and derived from biopsies from elderly patients as can be seen in Figure 3.2. The morphology and overall shape is different from rat cells, but characteristics such as fenestrations are also present. The hLSECs are bigger and have less fenestrations than later shown measurements (e.g. chapter 4), however the fenestrations number and diameter is strongly depending on age and health conditions of individuals.

3.3. Preparation of LSECs from rat

LSECs were isolated from rats through liver cell dispersion following enzymatic digestion of the liver tissue. For this procedure, a young, one month old rat was anesthetized, the abdomen was cut open and a canal was inserted into the portal vein. The inferior naval vein was ruptured to enable the blood and the perfusion washing solution to flow out.

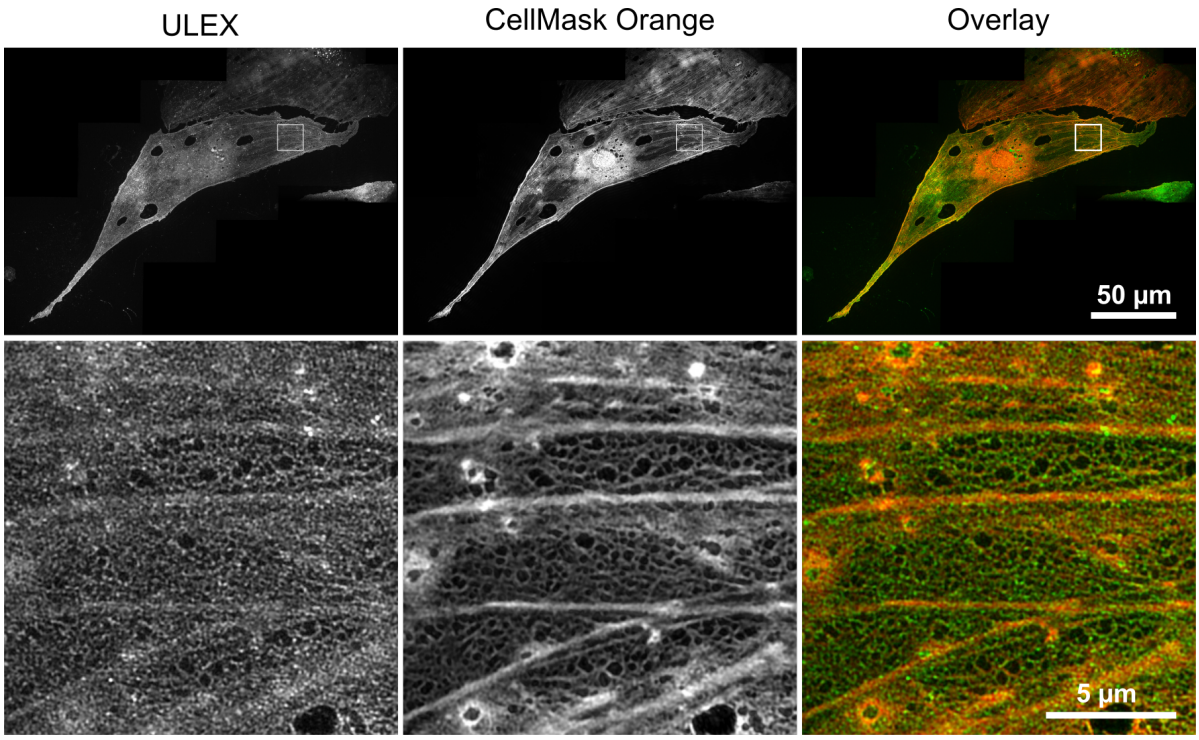

Figure 3.2.: Human LSECs imaged by 3D-SIM. The cells are stained simultaneously with ULEX-FITC and CellMask Orange. The top row shows the entire cell, while the bottom row is a crop corresponding to the drawn ROI. The cells are obviously much larger than rat LSECs however they show also the typical fenestration and sieve plate structures.

The liver was first perfused in vivo at a constant flow rate of 2 to 7 ml per min of perfusion buffer PBC (140 mM NaCl, 7 mM KCl, 10 mM Hepes) for 5 to 10 minutes. The perfusion continued after extraction of the entire liver from the animal for 30 minutes to completely rinse out the blood. Ex situ, the liver was then perfused with Collagenase containing buffer (Collagenase NB4 from Clostridium histolyticum in 90 mM NaCl 9 mM KCl 120 mM Hepes 7 mM CaCl2) for 20 minutes. The cells were resuspended through manual disintegration of the digested liver tissue with forceps in a preservation buffer and kept on ice. The cell suspension was split among two 50 ml conical tubes and centrifuged at 54 g for 2 minutes at 4 degrees. The resulting pellet containing hepatocytes was discarded while the supernatant is further centrifuged a second time at 54 g for 2 min. The second purified supernatant was pelleted at 1350 g for 10 min. The pellet was resuspended in 5 ml of preservation buffer per tube (1% BSA in PBC buffer). The combined cell suspension was layered on top of a Percoll gradient (20 ml each Percoll 50 % and 25 % with 7 to 10 ml of cells). The cells layered on the Percoll were centrifuged for 30 minutes at 1350 g without brake. The non-parenchymal cells (NPC) present at the interface between the two Percoll densities were collected with a pasteur pipette. The NPCs were washed in 50 ml preservation buffer and centrifuged at 1350 g for 10 minutes. The cell pellet was resuspended in 20 ml RPMI 1640 medium without serum.

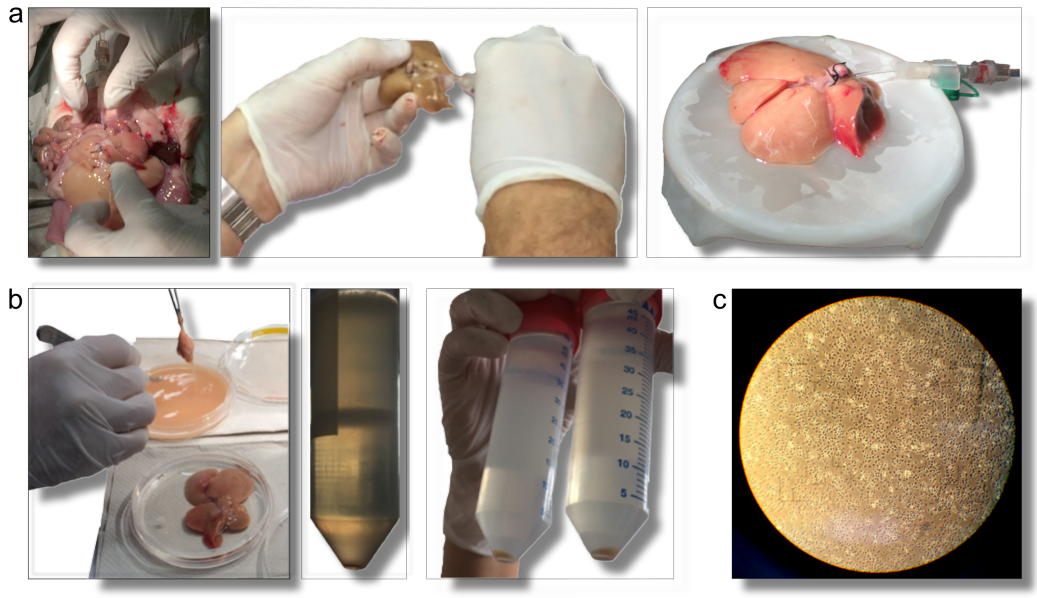

Figure 3.3.: Isolation of cells from rat liver by portal vein of the liver *in* and *ex situ*. First the liver tissue is washed from blood followed by digestion with Collagenase (a). Isolation of LSECs requires various centrifugation steps to isolate non-parenchymal cells including on a Percoll cushion (b). The isolated cell fraction is further purified for LSECs with selective adherence. Kuppfer cells are removed through binding to plastic dishes while the pure LSECs are selected through seeding on collagen coated culture plates and early extensive media washes (c).

The cells were further purified by selective adherence. The cell suspension was seeded on non-treated plastic petri dishes for 30 to 45 minutes. Kupffer cells adhered to the dish while LSECs remained in solution. These were plated onto collagen or fibronectin coated cell culture dishes. After 1 hour the strongly adhered LSECs were thoroughly washed with PBS to remove dead cells, non-adherent cells and contaminating parenchymal cells (PCs) such as hepatocytes. (Figure 3.3, see also [12, 77, 78])

3.4. Freezing and thawing of LSECs

The challenge in researching Liver Sinusoidal Endothelial Cells lies within the first step of the preparation. LSECs only exhibit fenestrations as primary cells, not as cultured cells. Also the preparation of these cells is quite difficult and demands a lot of experience. It is challenging to learn the subtleties required in the protocols.

For investigating living LSECs, the cells need to be newly plated, otherwise they will loose the fenestrations after 12 to 16 hours. This makes it impossible to ship living LSECs from our collaboration partners to us. Furthermore the existing proliferating LSECs available commercially do not possess fenestrations and sieve plates. We choose to have collaborators visiting our laboratories that would be capable of isolating correct and relatively pure fractions of rat LSECs.

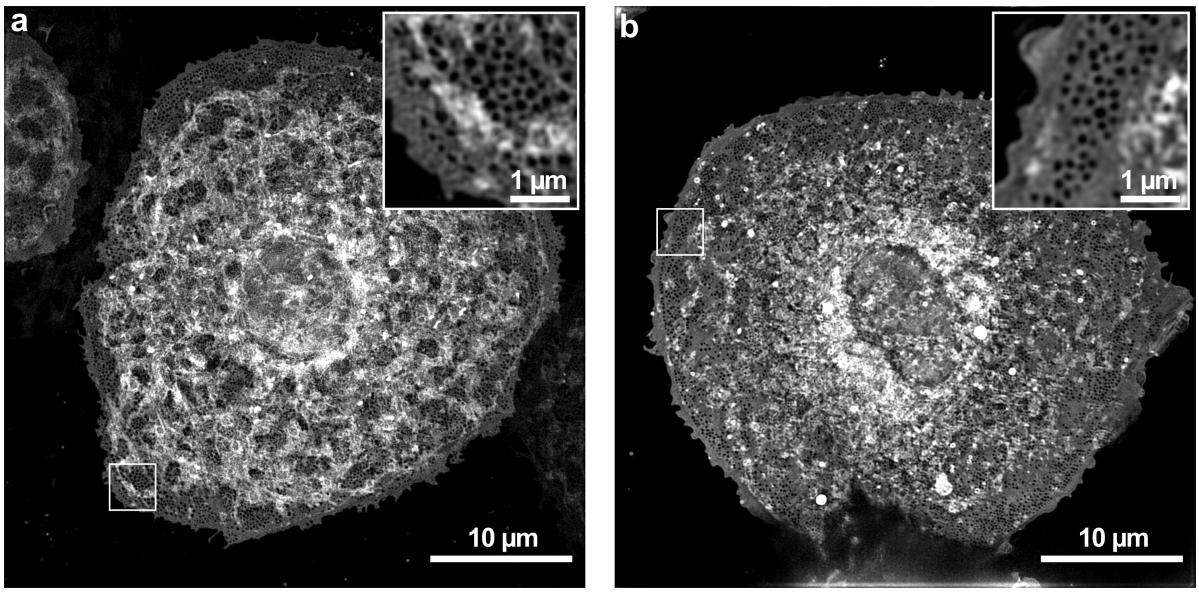

Figure 3.4.: Maximum intensity Z-projections of 3D-SIM data from LSECs under different preparations: (a) The LSEC plated directly after isolation and imaged 4 hours later and (b) the LSEC frozen directly after isolation and thawed months later show typical morphological structures, such as fenestrations which are arranged in sieve plates.

It was nevertheless desirable to find a way to freeze and thaw the freshly isolated LSECs any time an experiment is planned. For freezing fresh LSECs we used a similar protocol which is typically used for other primary cells and common cell lines (the freezing media contains 10% DMSO, 20% FCS and 70% RPMI). After thawing the cells, their viability was checked by observing their typical morphology. The fenestrations arranged in sieve plates are only observed in healthy cells, as any defect in these cells will manifest itself by the reduction and disappearance of their fenestrations and functionality. Due to the freezing process many cells died after thawing. Seeding of 250 000 cells on a 12 mm coverslip should lead to a mean density of 1736 cells per mm^2.

The thawed cells were further characterized by counting their fenestrations per sieve plate and the fenestration diameter. While it is possible to proliferate LSECs in cell culture conditions using specific media with supplements, they initially loose their fenestrations. Plating LSECs right after isolation maintains fenestrations for up to 12 to 16 hours. We applied standard cell culture freezing protocols to our freshly isolated LSECs. We observed that thawed cells behave similarly to cells plated immediately after purification. The most important morphological features, the fenestrations, are preserved. The sizes and numbers are comparable between fresh and thawed LSECs (see Figure 3.4).

3.5. Confocal microscopy images of LSECs

The investigation of LSECs by light microscopy is of great interest due to the fact that living cells and tissue can be analyzed. A common microscopy technique that can be

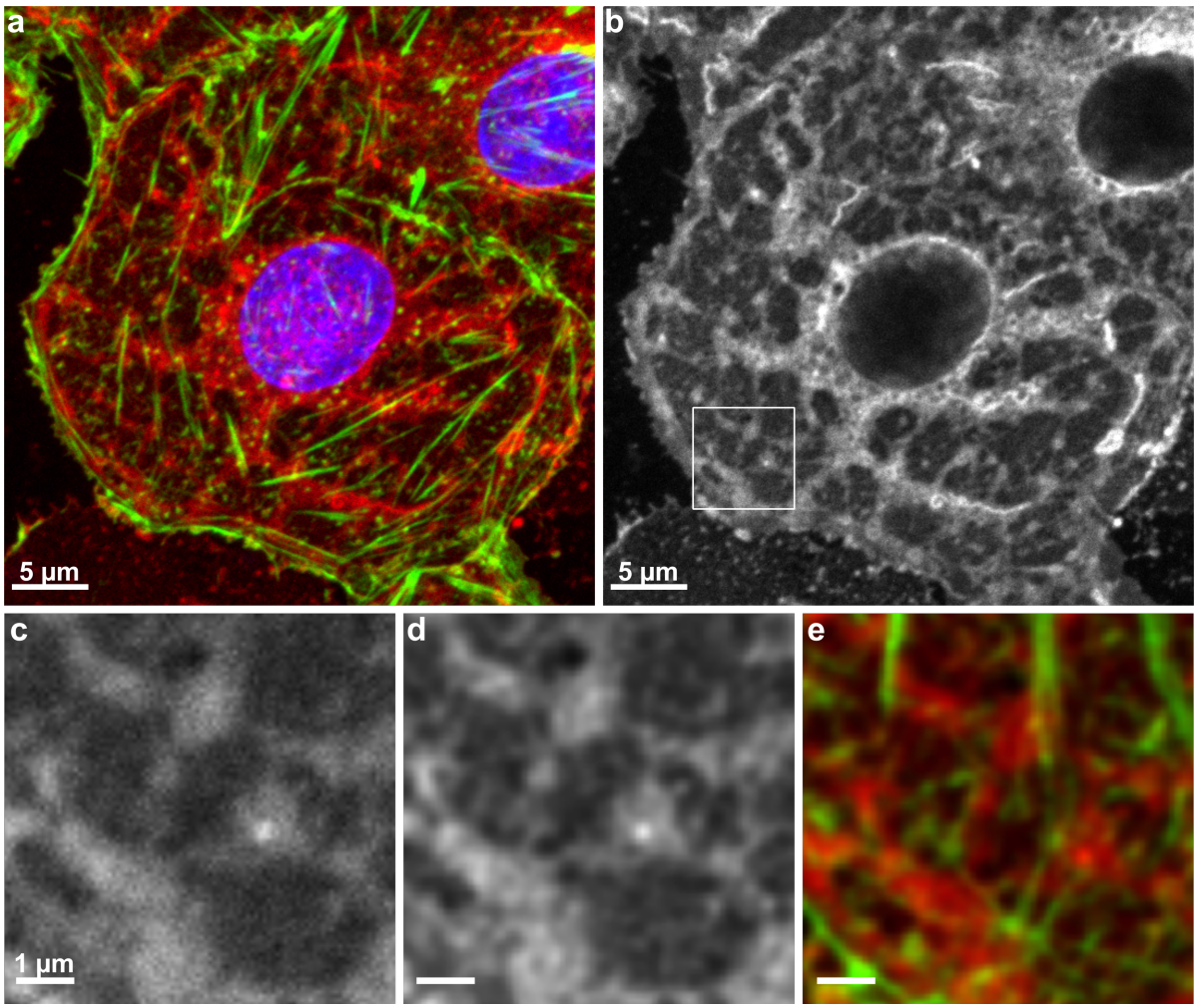

Figure 3.5.: LSM image of an entire isolated rat LSEC (a) with stained nucleus (blue), actin (green) and membrane (red). In (b) only the membrane channel of the same image is shown. The ROI (dashed box) is enlarged in (c) for the membrane LSM raw data as well as in (d) for the deconvolved LSM data. (e) shows an overlay of the deconvolved actin and membrane channels from that ROI area.

found in almost any biology facility is a Laser Scanning confocal Microscope (LSM). LSECs have a very special morphology, fenestrations with diameters of about 120 nm that are arranged in sieve plates with diameters of about a few microns. Microscopy techniques used for investigation of these structures must therefore be capable of resolving the features of interest at different length scales. Transmission electron microscopy (TEM) as well as scanning electron microscopy (SEM) are possibilities for this purpose. However, for these techniques the biological samples must undergo fixation and drying processes i.e. an observation of living cells is not possible. Optical fluorescence microscopy, on the other hand, enables the observation of living cells and ongoing processes. However, in order to observe the membrane features staining with a fluorophore is necessary.

In Figure 3.5 an isolated rat LSEC is imaged by LSM (Zeiss LSM780). The fixed cells

are stained with DAPI for the nucleus (blue), Phalloidin Atto 488 for the actin filament (green) and with CellMask Orange for the membrane (red).

The LSEC shows the typical round flat shape of isolated rat LSECs. Small and dimmed structures are spotted in the entire membrane except for the nuclear area. These structures are the sieve plates containing the fenestrations. In Figure 3.5 (b) the isolated color channel of the membrane is illustrated to obtain a better overview of the cell morphology. The region of interest (dashed box) is enlarged in Figure 3.5 (c) to observe the details inside the sieve plates. Figure 3.5 (d) shows the additionally deconvolved image of the same area. The resolution of the LSM, even in combination with deconvolution, is not good enough to resolve single fenestrations. One can barely make out the sieve plates and some substructures.

The combination of the deconvolved membrane and actin channel of the ROI is shown in Figure 3.5 (e). In order to answer the question how the fenestrations are formed and if actin plays a role in this it is important to investigate the correlation between membrane and actin. One can clearly see a colocalization of both channels which gives an indication for a strong correlation, however, the details cannot be resolved.

To further investigate these samples, super-resolution microscopy techniques such as Structured Illumination Microscopy (SIM) and single molecule based localization microscopy (e.g. STORM, PALM) are needed.

4. LSECs imaged by single molecule localization microscopy compared to structured illumination microscopy

Cogger et al. [11] first showed that structured illumination microscopy offers the possibility to investigate LSECs by surpassing the resolution limit of light microscopy techniques. The spatial resolution of linear SIM reaches about 100 nm (lateral) in the best case. This enables the general visualization of fenestrations, but investigating the shape and precise size of the fenestrations requires much higher resolution. To gain a deeper insight into the structural details of fenestrations in LSECs, direct stochastic optical reconstruction microscopy (*d*STORM) is applied in this work. *d*STORM is a single molecule localization microscopy based technique and enables five times higher spatial resolution than 3D-SIM (see chapter 2.4) for typical biological samples.

In the following, I summarize the revised and supplemented results adapted from my first-author paper 'Imaging fenestrations in liver sinusoidal endothelial cells by optical localization microscopy' published in 2014, see [13].

4.1. *d*STORM on LSECs

The biggest challenge was to find a suitable dye which offers a dense membrane staining and at the same time undergoes a photoswitching process to enable single molecule based localization microscopy. There is no hint in literature that the staining (CellMask Deep Red) used in previous 3D-SIM studies on LSECs [11] has been used for *d*STORM imaging up to now. This stain is a lipophilic fluorophore which stains cellular plasma membranes in live and fixed cells. By optimizing the photochemical behavior of CellMask Deep Red this dye was applied for *d*STORM imaging of LSECs for the first time. Further fluorophores were tested as well (see chapter 6) to investigate their respective advantages and disadvantages for imaging LSEC fenestrations.

An entire isolated rat LSEC reconstructed by *d*STORM is shown in Figure 4.1. For the reconstruction 13483 frames were recorded and analyzed.

In this image characteristic cellular structures can be identified precisely. The nucleus in the center is readily distinguishable from the circumference of the cell. Filopodia reaching out of the neighboring cell as filigree, thin structures on the right hand side of the figure are clearly defined. This cell contains a large number of sieve plates with dimensions of up to several microns (see Figure 4.1 (a)). The ROI in 4.1 (a) is enlarged

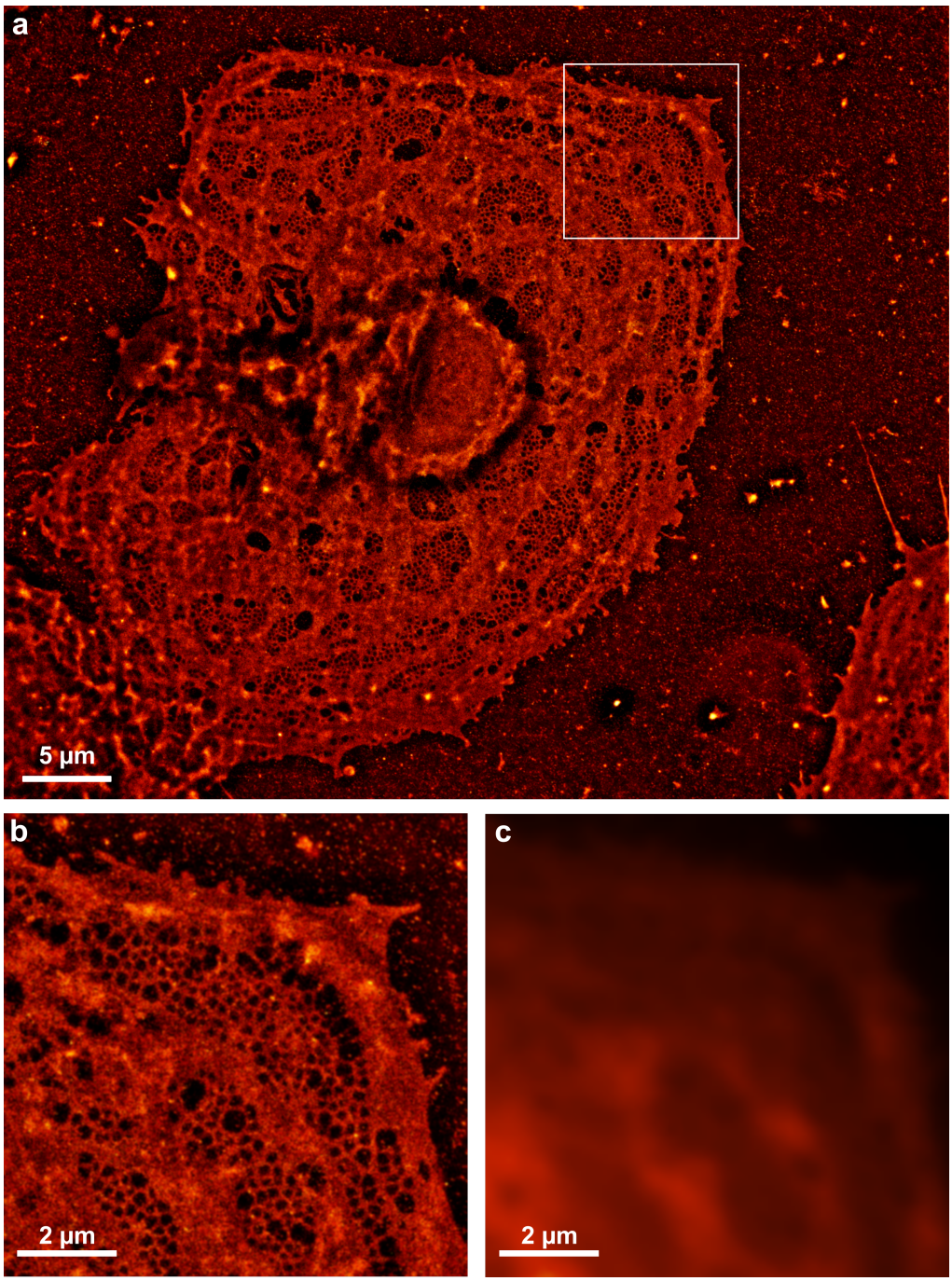

Figure 4.1.: (a) *d*STORM image of a liver sinusoidal endothelial cell (LSEC) plated on a fibronectin-coated glass coverslip, stained with 5 µg/ml CellMask Deep Red, and post-fixed with 3.7% PFA. The single frame exposure time was 29.55 ms, and a total of 13 483 frames were used in this reconstruction, resulting in a total acquisition time of about 7 min. The region highlighted in (a) is shown magnified in (b) and compared to the conventional wide-field microscopy image (c). Sieve plates and individual fenestrations can be seen as dark spots against the bright background from the plasma membrane.

in 4.1 (b). Each sieve plate contains tens of fenestrations with a mean diameter in the order of approximately 100 nm. The image acquisition was performed under a TIRF/ HILO configuration which worked well for the outer cell region due to the thinness of the plasma membrane. In the neighborhood of the nucleus less details are observed for two reasons: First, the main part of the nucleus is outside of the focal plane due to its larger dimension in z direction. Second, due to agglomeration of the CellMask stain close to the nucleus the dye concentration is too high to resolve this region with single molecule based localization methods. The stain is clustering in this region due to the presence of multiple membranes surrounding the nucleus as well as the endoplasmic reticulum.

The conventional fluorescence wide-field image of the magnified ROI, acquired in the same TIRF/HILO configuration is shown in Figure 4.1 (c) for comparison. In contrast to the *d*STORM image (Figure 4.1 (b)) the wide-field image is almost featureless and only dark regions embedded in brighter surroundings are visible adumbrating the location of sieve plates. Only by verification with the complementary *d*STORM image these regions can be identified as sieve plates. In the super-resolved image the fenestrations appear as well-defined holes in the membrane with dimensions below the optical diffraction limit.

4.2. Evaluation of the fenestration diameter in *d*STORM vs. 3D-SIM

Another entire LSEC imaged by *d*STORM can be seen in Figure 4.2. In order to evaluate the obtained results a comparison to another state-of-the-art super-resolution microscopy technique is made: 3D structured Illumination Microscopy. Figure 4.3 (a) and (b) show a 3D-SIM image and a magnified view of a similar (but different) LSEC, also stained with CellMask Deep Red using the same protocols as for *d*STORM imaging.

In contrast, other *d*STORM images are shown in Figure 4.3 (c) and (d). Both methods are clearly capable of resolving the fenestrations, however it is quite apparent that *d*STORM is able to resolve even smaller fenestrations that cannot be resolved by 3D-SIM. Furthermore *d*STORM is able to reveal very thin membranes that divide individual fenestrations that are seen as one single feature in 3D-SIM (see Figure 4.4 and 4.5 for such examples).

By utilizing a pore area analysis tool (Volocity, PerkinElmer) both super-resolution microscopy methods permit a quantitative analysis of the fenestration diameter. Since *d*STORM can in principle achieve a localization precision of below 20 nm it enables the observation of smaller structures than with SIM, which is limited to about 100 nm.

Interestingly, the mean pore diameter of 129.1 $\pm$ 33.1 nm, obtained by 3D-SIM, is very similar to that observed by *d*STORM with 119.8 $\pm$ 37.6 nm (see Figure 4.4 (a) and (c). The *d*STORM measurements result in a broader distribution of pore diameters, especially towards smaller pore sizes. This is related to the improved spatial resolution that allows the measurement of a wider range of fenestrations. In a few cases, fenestrae with a diameter of less than 50 nm can be identified.

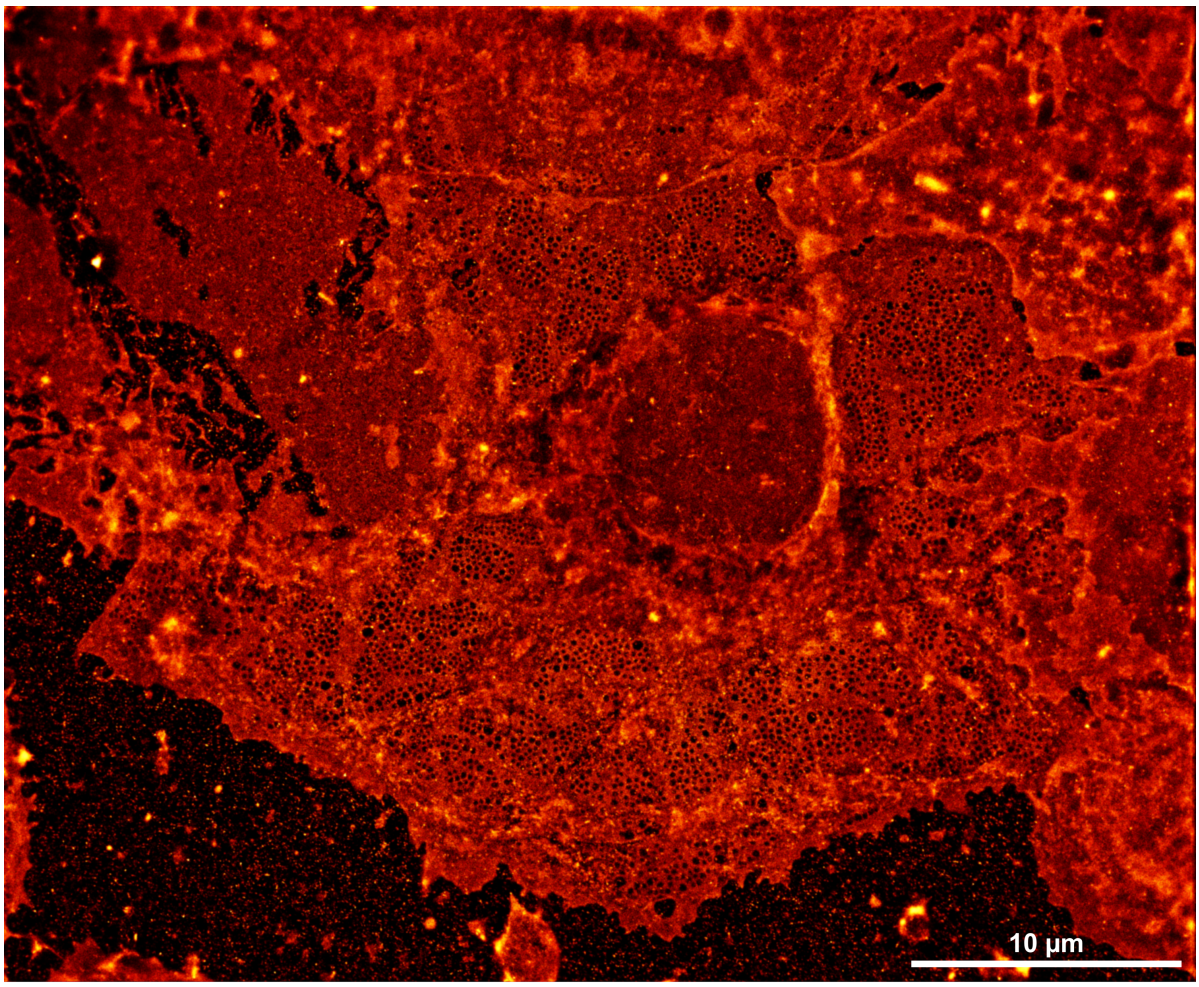

Figure 4.2.: *d*STORM image of an entire cell where the intrinsically higher resolution of localization microscopy becomes apparent. Single frame exposure time: 20.40 ms, 40 000 frames, total recording time: about 14.5 min.

In summary, the submicroscopic morphological structures of LSECs, so-called cellular fenestrations, can be visualized by single molecule localization microscopy of the cell membrane stain CellMask Deep Red in combination with a specifically adapted staining protocol (see 9.3). The challenge concerning the visualization of the fenestration structures is their negative contrast. Since there are no markers for fenestrations available yet, the complete membrane will be stained around the fenestrations. The reproduction of an inverse structure such as pores in a membrane is a challenge for single molecule based microscopy techniques such as *d*STORM and PALM. Until now, *d*STORM was usually applied in order to image defined cellular structures whose constituents can be stained, such as the cytoskeleton, mitochondria, vesicles, or nuclear pore complexes. In contrast, for reconstruction a surface containing holes successfully, it has to be stained with a dense and homogeneous distribution of a fluorophore (see Nyquist-Shannon criterion, chapter 2.4.2) that can undergo rapid photoswitching. The lack of specific markers for fenestrations and the required high fluorophore density make it difficult to ensure no

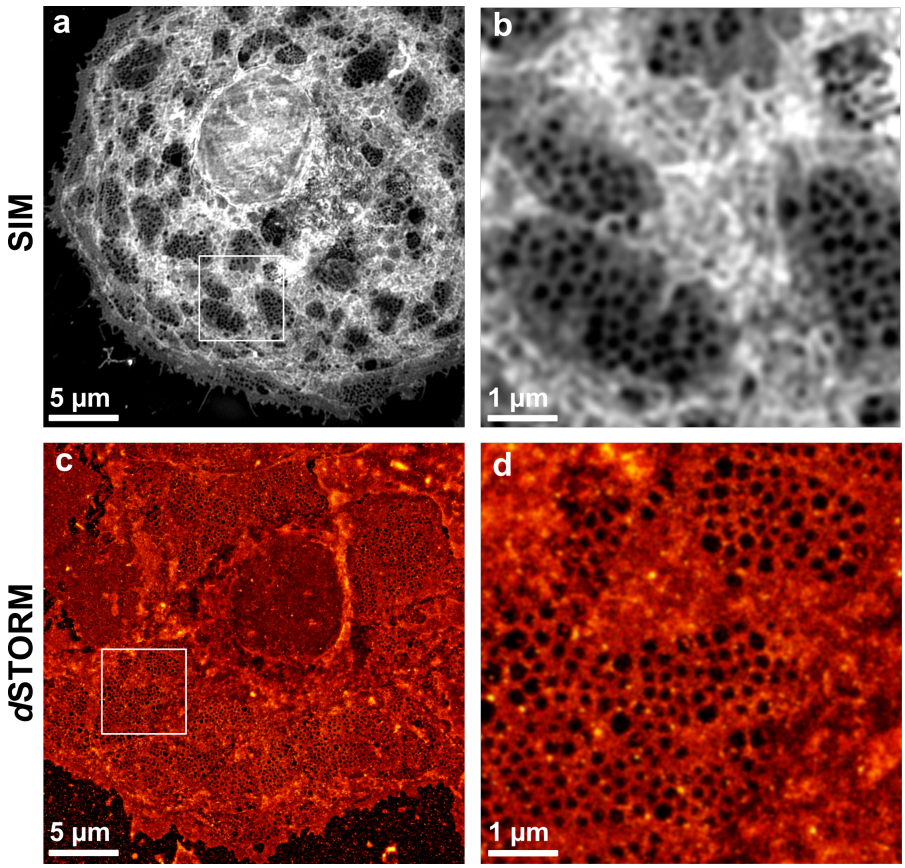

Figure 4.3.: (a) Structured illumination microscopy image of a representative single LSEC stained with CellMask Deep Red. (c) *d*STORM image of a similar cell where the intrinsically higher resolution of localization microscopy becomes apparent. Single frame exposure time: 20.40 ms, 40 000 frames, total recording time: about 14.5 min. (b) and (d) are magnifications of the regions highlighted in (a) and (c), showing several sieve plates.

secondary, unlabeled regions appear as artificial (i.e. not existing) holes in the surface. Additionally overlaps between single blinking events need to be avoided at this time, because the reconstruction software rapidSTORM was limited to single emitter fitting.

A further challenge was the minimization of unspecific fluorophore binding to the substrate (e.g. fibronectin on glass coverslips), since this leads to background fluorescence and makes it impossible to image very small structures. When positive structures are labeled the requirements for appropriate staining protocols are therefore easier to fulfill than in this case. In these experiments, after investigating a range of fluorophores, only the lipophilic dye CellMask resulted in reliable staining of LSEC membranes that enabled the visualization of fenestrae over a wide range of diameters (an alternative dye is discussed in chapter 5). The result of using this dye combined with TIRF/HILO excitation of the fluorophores, allowed me to observe fenestrations with diameters as small as 50 nm (see Figure 4.4).

A closer look at the level of individual sieve plates shows the rather nonsymmetric substructure of fenestrae, which typically appeared as round holes when imaged by 3D-

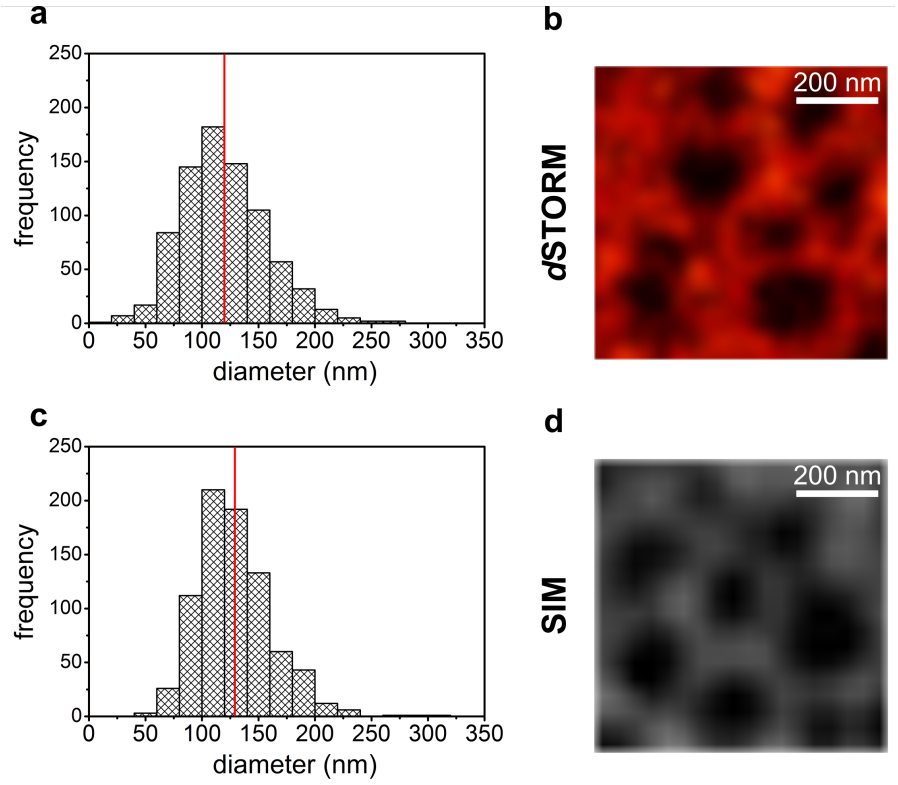

Figure 4.4.: (a) Histograms of the fenestration diameters imaged by *d*STORM (evaluated from Figure 4.3 (c)) and 3D-SIM (evaluated from Figure 4.3 (a)) measured by determining the full-width half minimum of 800 fenestrae, each. Both histograms show a normal distribution with a mean diameter of 129.1 nm (SIM) and 119.8 nm (*d*STORM) (red lines). (b) Enlargement of a 720 x 720 nm^2 area to show differences in details of *d*STORM and SIM reconstructions. *d*STORM (upper right) performs localization with 20 nm accuracy, resulting in the resolution of fine details such as dividing membranes.

SIM. This is demonstrated in Figure 4.5, where *d*STORM images of sieve plates are compared to similar data (again, from different cells) obtained by scanning electron microscopy (SEM).

For instance in the upper half of Figure 4.5 (a)) thin membranes crossing fenestrae can be observed, similar to structures which can be seen in Figure 4.5 (d), that indicate the three-dimensional nature of these structures crossing the cell's cytoplasm.

In future, *d*STORM and other optical super-resolution microscopies can be used to replace the more elaborate and expensive procedures required to view fenestrations by SEM. Another advantage of optical microscopy is that multiple structures can be stained and imaged simultaneously, and it has the potential to ultimately enable imaging of fenestration dynamics in living LSECs while for SEM fixation of cells is required.

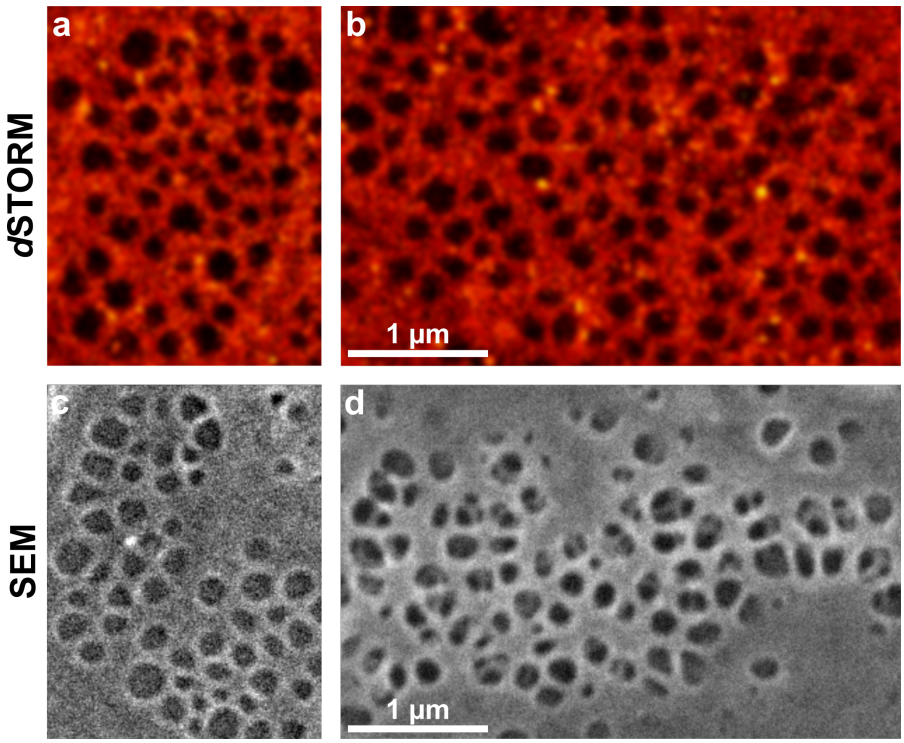

Figure 4.5.: Comparison of LSEC fenestrae and sieve plates imaged by (a, b) *d*STORM and (c, d) scanning electron microscopy (SEM). This direct comparison demonstrates nicely how *d*STORM achieves a resolution similar to that obtained by SEM, but in wet, fixed LSEC preparations. Remarkably, the non-circular substructure seen by SEM is now also resolved optically.

4.3. Acquisition speed

The extension of 3D-SIM to living cells is straight-forward and has been demonstrated multiple times, since only 9 to 15 SIM frames have to be acquired in order to reconstruct a single plane [79, 80, 81], but live cell imaging by *d*STORM is more cumbersome, because even in the best of cases thousands of frames have to be acquired in order to reconstruct useful images from *d*STORM data [52].

Especially the visualization of image structures with negative contrast, such as fenestrations, will likely require the acquisition of even more individual frames. In Figure 4.6 the exploration of the minimum number of frames required to resolve fenestrae is shown. Therefore we took one of the data sets and consistently reduced the total number of frames that were used for image reconstruction. One important step to achieve the lowest possible number of frames was to employ an automated drift correction routine for the image sequence.

Figure 4.6 shows a sequence of images, where the number of frames used for the final reconstruction has been consistently lowered from 10 000 to 2000. It can be seen from this figure, that still some fenestrae can be identified even if only 2000 frames were used for the reconstruction.

This shows that the possibility of live *d*STORM can be realized by additional improve-

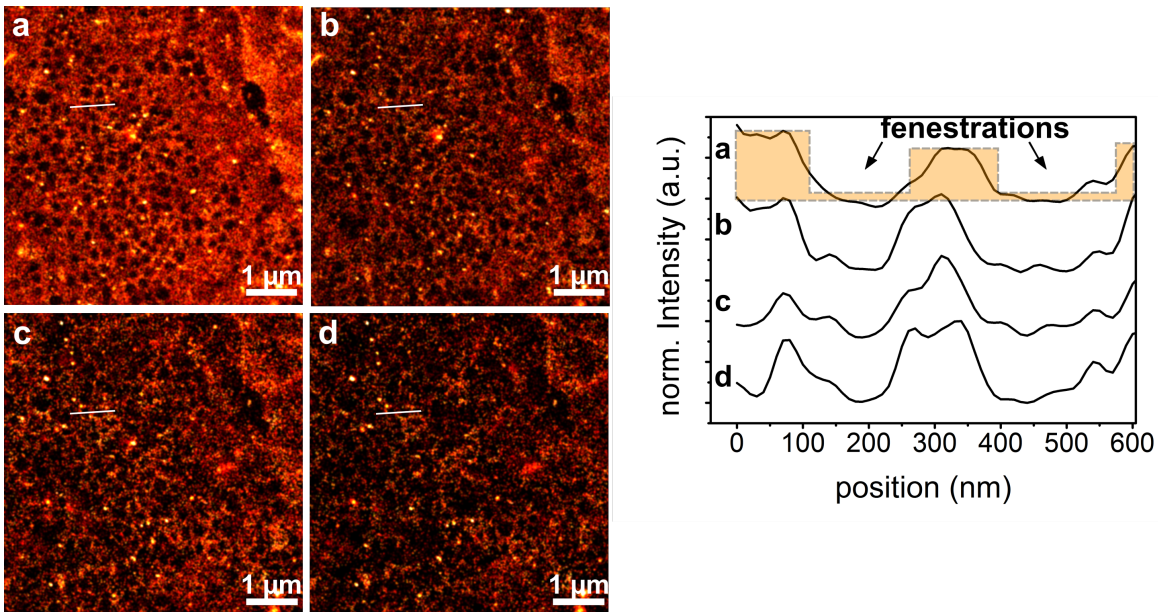

Figure 4.6.: Continuous reduction of the number of frames used to reconstruct a sieve plate. The number of frames are (a) 10 000, (b) 5000, (c) 3000, and (d) 2000. Cross-sections of the same location in each image are shown below the image sequence. This indicates that some fenestrae can still be identified if as few as 2000 frames have been acquired, potentially enabling rapid live cell imaging of fenestration dynamics.

ments of setup and data processing. On the one hand by employing faster EMCCD or sCMOS cameras approximately 1000 frames can be acquired in 1 s, which indicates that even *d*STORM imaging of fenestration dynamics could be achieved on the order of 1 to 2 seconds for each final, reconstructed image. On the other hand a software for multi-emitter fitting for the reconstruction enables even faster imaging, due to finding more localizations in less time.

4.4. Conclusion

In this chapter I demonstrated that with single molecule based super-resolution techniques such as *d*STORM it is possible to image morphological features in the cellular plasma membrane that provide negative contrast, i.e. which cannot be stained directly. This technique allows the identification of fenestrations with diameters of less than 50 nm. The investigation also showed that the fenestrations are not necessarily round holes as they were seen in 3D-SIM, the results showed non-circular substructures comparable to SEM.

The cognition that 2000 frames are deemed necessary to successfully reconstruct sieve plates in the plasma membrane of LSECs by *d*STORM shows that live *d*STORM imaging of these cells is possible after some improvements of setup and software. The reduction to even fewer frames is conceivable by employing other means of analyzing and reconstructing the data, e.g. super-resolution optical fluctuation imaging (SOFI).

The fluorophore I used in this work, CellMask Deep Red, is perfectly capable of staining the membrane of living and fixed cells. The effect on the structures of fenestrations and LSECs itself depends hardly on the concentration of the dye and additional factors such as radiation (see chapter 6).

These results show that imaging of LSEC fenestration morphology is possible, based on a technique that can be used to equip even standard fluorescence microscopes with super-resolution capabilities at a very low cost especially compared to SEM and SIM. This makes it accessible to a much larger range of biomedical research laboratories all over the world.

5. LSECs imaged by single molecule localization microscopy and structured illumination microscopy on the same setup

Super-resolution microscopy techniques often require certain trade-offs with respect to sample preparation or the use of fluorescent stains. The SMLM-techniques, such as *d*STORM (see chapter 4), provide very high spatial resolution but require rather long overall signal accumulation times, as they need several thousands of frames to achieve their high resolution. In contrast, three-dimensional structured illumination microscopy (3D-SIM) can be utilized in a fast acquisition mode, but only offers a limited increase in spatial resolution (about 2x compared to wide-field).

Many applications, in particular live cell imaging applications, require a rapid search mode that enables the identification of cells/areas of interest, which is then followed by more time-consuming, super-resolution microscopy measurement of the relevant features. One way by which this can be achieved is using a conventional fluorescence microscopy platform in combination with an integrated SMLM-super-resolution modality.

In the following, the revised and supplemented results adapted from my 2015 published first-author paper 'Multimodal super-resolution optical microscopy visualizes the close connection between membrane and the cytoskeleton in liver sinusoidal endothelial cell fenestrations', are presented (see [82]), where two super-resolution techniques (3D-SIM and *d*STORM) were implemented on the same microscopy platform.

5.1. Correlative SMLM and 3D-SIM on the same setup

SMLM measurements, such as *d*STORM, are typically carried out by selection a region of interest (ROI) with wide-field imaging (limited to 200 nm resolution, and then carrying out the *d*STORM experiment. However, if the targets of interest such as the cellular fenestrations of LSECs in the study, are only visible at resolutions well below the optical diffraction limit, then a combination of super-resolution techniques is needed. One modality provides the ability to rapidly survey the sample, ideally in multiple color channels, and can then easily be switched to an even higher resolving technique if needed. Such a combination of 3D-SIM and *d*STORM, however, in order to take advantage of

the specific strengths of each technique, had not been utilized until now.

A few attempts in multi-modal super-resolution microscopy have been demonstrated so far. Matsuda et al. used a 3D-SIM platform to acquire data for single molecule localization microscopy, but did not compare the two modalities [14]. Rossberger et al. combined structured illumination microscopy and single molecule localization microscopy into a single platform and demonstrated this by imaging identical regions of HEK293 cells [15]. The structured illumination microscopy part was, however, only demonstrated in two dimensions and for a single color. Most recently, Hamel et al. used a commercial 3D-SIM platform to obtain multi-color SIM data and compared them with the higher resolution obtained by single molecule localization microscopy [16]. These authors did, however, not demonstrate a rapid 3D-SIM search and stitch mode to survey large samples.

I used the ability of a single optical platform to rapidly search, survey, and stitch large sample areas for relevant feature sizes in multi-color operation on fixed freshly isolated rat LSECs. Once areas with sieve plates were identified, the illumination and acquisition mode of the microscope was switched to *d*STORM to revisit these locations and enable the acquisition of images of the LSEC cytoskeleton and fenestrations with up to 20 nm localization accuracy. The combination of both methods also enabled to perform cross-modality correlation of areas that can only be imaged by one modality, which ultimately enables us to directly compare the association between the LSEC cytoskeleton and the plasma membrane.

The first evaluation of whether complimentary *d*STORM and 3D-SIM imaging of multiply stained samples is possible on our commercial 3D-SIM system was done with fixed rat LSECs stained with four different fluorophores. I stained the nucleus with DAPI, actin filaments with Phalloidin-Alexa488, membranes with CellMask Orange and microtubules with an anti β-tubulin antibody visualized by using a secondary antibody coupled to Alexa Fluor 647.

Alexa Fluor 647 is well suited for *d*STORM imaging so it was chosen for single molecule localization microscopy on our existing commercial 3D-SIM platform. The 642 nm diode laser in our setup provides the highest intensity compared to the other available lasers (300 mW vs 100 mW). These high excitation intensities are necessary for successful *d*STORM image acquisition and subsequent reconstruction. The addition of specific hardware modules was avoided to keep the experiments as simple as possible.[1]

In comparison to the most *d*STORM images that are shown in the literature and which are collected by total internal reflection-excited fluorescence (TIRF), the following *d*STORM images are obtained in ringTIRF illumination mode. RingTIRF continuously excites the sample from all directions to ensure a more even illumination of the sample, which further improves the performance of this system for single molecule localization analysis. None of the following *d*STORM images shown in this chapter used true TIRF illumination, where the illumination arrives at the sample at an angle slightly beyond

[1] Nowadays a additional motorized optical component, a so-called field concentrator is available as an official add-on to the OMX v4. It reduces the size of the field-of view illumination by the laser (by 2x in each dimension) and this increases local field strength about 4x at the same laser output power.

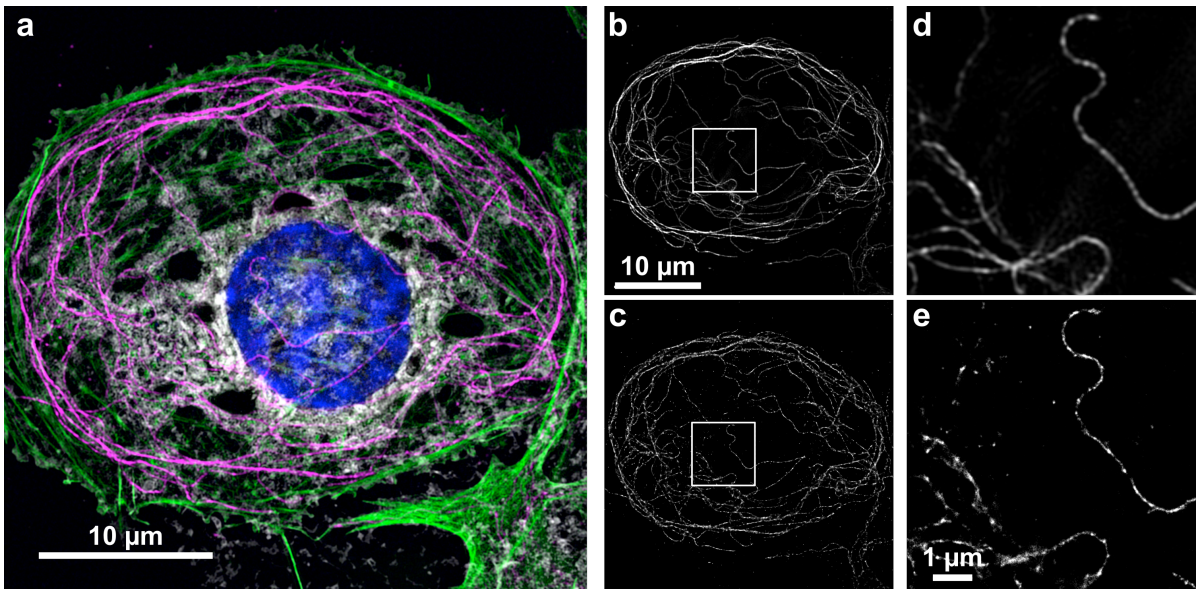

Figure 5.1.: (a) Maximum intensity z-projection 3D-SIM image of a 4-color-stained fixed rat LSEC. The nucleus was stained with DAPI (blue), actin filaments with Phalloidin-Alexa488 (green), membranes with CellMask Orange (white), and tubulin structures with anti β-tubulin mouse antibody followed by an anti-mouse IgG-AF647 antibody (magenta). The maximum intensity z-projection corresponds to a sample thickness of 750 nm. (b) Maximum intensity z-projection 3D-SIM image of the tubulin channel from (A) compared to the *d*STORM reconstruction (c) of the same cell. (d) Enlarged 3D-SIM and (e) *d*STORM images of the ROIs (dashed-line boxes) shown in (b) and (c). The *d*STORM image shows a direct correlation with the corresponding 3D-SIM image, but with an optical resolution of approx. 20 nm. The single frame exposure time of the *d*STORM image was 20 ms and a total of 10000 frames were used for the reconstruction. The sample was mounted in Vectashield.

the angle of total internal reflection. Instead, an angle only below the angle of total internal reflection was chosen to create highly inclined laminated optical sheet (HILO) illumination. This mode avoids the background issues from excitation of fluorescence by evanescent waves, which pronounces sample structures and non-specifically bound probes near the glass slide and also leads to an increased laser intensity density due to the smaller light sheet through the sample.

Ideally a comparative analysis of 3D-SIM and *d*STORM would use a switching buffer system that is suitable for both super-resolution methods, especially since the chemical environment is crucial to facilitate successful *d*STORM reconstructions. Most measurements are therefore conducted using Oxygen Scavenging System (OSS) buffers. For 3D-SIM imaging, *Vectashield* (Vector Labs) is commonly the preferred mounting medium mostly due to its well suited index of refraction that enables aberration-reduced imaging of cells. On the other hand it turns out that Vectashield coincidentally works well with several different dyes (e.g. Alexa647) to enable single molecule based localization microscopy with excellent blinking behavior of Alexa Fluor 647. Another advantage of Vectashield is that the mounted samples are more photostable than with aqueous OSS-buffers. Even weeks after mounting, DiD showed a photoswitching behavior comparable

to that of freshly prepared samples. The result of our 3D-SIM followed by *d*STORM imaging experiment applied to the tubulin cytoskeleton in fixed LSECs is shown in Figure 5.1.

Figure 5.1 (a) shows the 4-color maximum intensity projection of a 3D-SIM reconstruction of a 750 nm thick z stack of an entire LSEC. The plasma membrane of the cell is seen here in white stained by CellMask Orange. The Actin filaments (here in green) form a network throughout the cytosol and at the cell circumference. The Microtubules are arranged in nicely separated filaments spanning the cell, here visualized in magenta. For better visualization of the Microtubules we isolated the color channel in which the fluorescence of the stained tubulin fibers was recorded by 3D-SIM (Figure 5.1 (b)) and the same image recorded by *d*STORM (Figure 5.1 (c)). For better comparison of the capability of both super-resolution microscopy modes to precisely register the same structures and to compare their respective spatial resolutions, an enlarged overlay of the areas highlighted by dashed-line boxes is shown in these images (Figure 5.1 (d) and 5.1 (c)).

Figure 5.1 proves the extension of our commercial 3D-SIM setup (DeltaVision OMX v4 BLAZE) to apply two different, but complementary super-resolution techniques, 3D-SIM and *d*STORM, to the same sample for comparative analysis of LSEC ultrastructures. This was accomplished without any modifications to the microscope. *d*STORM image acquisition was performed using HILO illumination as it is typically performed on our custom-built STORM/PALM setup (see chapter 4).

The greatest challenge is the fact that single molecule based localization microscopy becomes very difficult using the low laser powers. The commercial platform provides a laser power density at the sample of less than 0.5 kW/cm which is approximately twofold less than what is typically required for successful *d*STORM reconstructions with home-built setups. It depends on the fluorophore what minimum laser power is needed to enhance the photoswitching rate of the respective fluorophores in order to adjust the blinking rate.

5.2. Correlative SMLM and 3D-SIM of LSECs

Since I have demonstrated the ability to visualize LSEC fenestrations by *d*STORM using CellMask Deep Red (CMDR) as a plasma membrane stain in chapter 4, but this was carried out on a dedicated custom-built *d*STORM setup (with high laser power). Apparently the next step is to evaluate the ability of our commercial 3D-SIM platform to perform *d*STORM imaging of plasma membrane stains. The result is shown in Figure 5.2, where I compared the performance of two different plasma membrane stains: CMDR (Figure 5.2 (a)), and Vybrant DiD (Figure 5.2 (b)). It is obvious that both dyes stain sieve plates and fenestrations quite well.

However, compared to Vybrant DiD, CMDR produced significant background due to nonspecific binding of the probe to the substrate. CMDR appears to have a considerable affinity to fibronectin or collagen coated glass slides, limiting its use for *d*STORM imaging in TIRF mode.

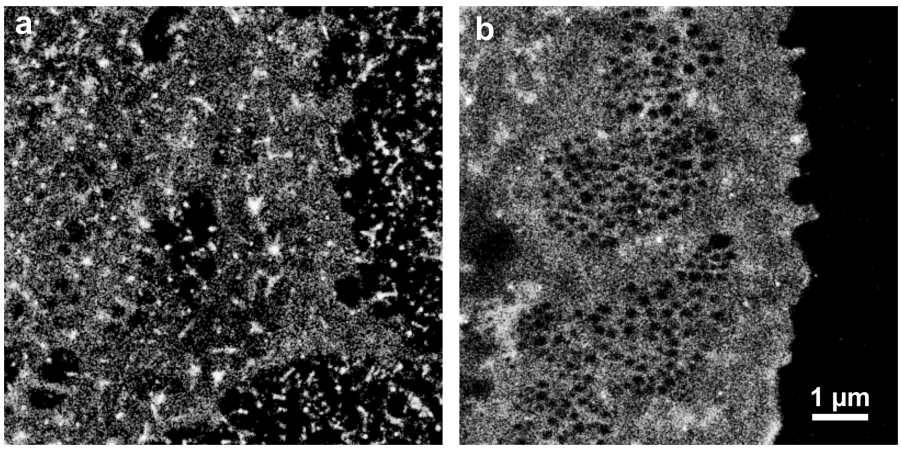

Figure 5.2.: (a) *d*STORM image of a fixed rat LSEC stained with CellMask Deep Red. Note the significant unspecific binding of the stain to the substrate which makes it nearly impossible to discern cell and background. (b) *d*STORM image of another fixed rat LSEC stained with Vybrant DiD. Note the reduced unspecific binding to the background.

For investigating in structures with negative image contrast by *d*STORM, such as fenestrations in the cellular plasma membrane, it is important that the sample has to be stained with a dye coverage that is as uniform and dense as possible to avoid potential artifacts such as non-existing holes that might appear due to spotty membrane staining. I previously showed in chapter 4 that CellMask Deep Red (CMDR) is a useful membrane stain for this application. The imaging of a densely labeled cellular membrane can be compared to imaging an extended 2D structure. Each fluorophore has multiple neighboring fluorophores, increasing the likelihood of overlapping single molecule emissions in single frames. Unless multi-emitter fitting algorithms are employed to analyze such data, these overlaps between blinking events of single molecules need to be avoided by appropriately adjusting the laser exposure power. In the case of CMDR the use of an even higher laser power than what is available with our commercial 3D-SIM platform is necessary. This lack of power results in less than ideal *d*STORM measurements (Figure 5.2), which explains the 'granularity' of the *d*STORM images compared to our previous results.

Even though CMDR is an excellent plasma membrane stain, well suited for fixed and live cell experiments, it leads to high background contributions from regions outside the cell in the *d*STORM reconstructions as shown in Figure 5.2 (a). It turns out that CMDR exhibits an affinity for fibronectin and collagen coated glass slides. Recording in TIRF mode only enhances this effect.

Interestingly, Vybrant DiD labeling of membranes is very well suited for *d*STORM acquisitions (Figure 5.2 (b)). With this fluorophore, 50% of the full laser power of the 642 nm diode laser (see B.3) was sufficient to induce appropriate blinking rates of the fluorophore. If required, Vybrant DiD can be activated using 405 nm or 488 nm in order to adjust the density of blinking emitters in a single frame. DiD appears to be highly specific for cell membranes and thus shows extremely low background contributions.

Because of the excellent staining of sieve plates by Vybrant DiD we next evaluated its

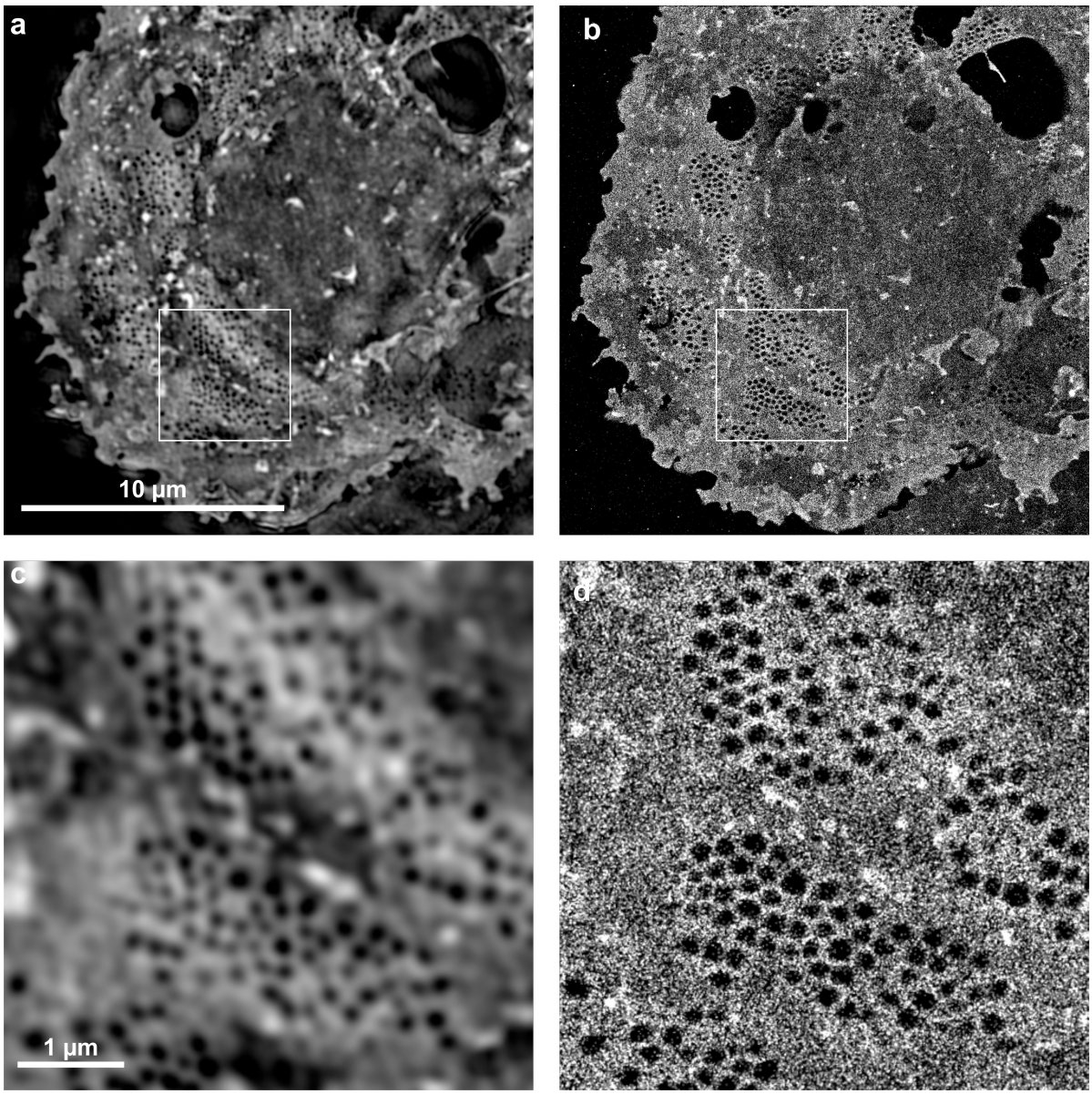

Figure 5.3.: (a, c) 3D-SIM and corresponding (b, d) *d*STORM images of a fixed rat LSECs stained with Vybrant DiD. The cells were mounted in the reducing buffer OSS+MEA (see Materials and Methods). (c) and (d) show enlarged views of the corresponding ROIs shown in (a) and (b). The 3D-SIM image is a maximum intensity z-projection image of a 500 nm thick part of the cell. The exposure time for a single *d*STORM frame was 20 ms and 15000 frames were processed to reconstruct the images shown in (b, d).

potential for multi-modal imaging by 3D-SIM and *d*STORM. This is shown in Figure 5.3, where an entire LSEC was first imaged by 3D-SIM (Figure 5.3 (a), (c)), and then by *d*STORM (Figure 5.3 (b), (d)). Figures 5.3 (c) and 5.3 (d) show enlarged views of the ROIs highlighted in Figures 5.3 (a) and 5.3 (b). In this direct comparison the significantly improved spatial resolution of the fenestrations by *d*STORM can be easily seen. It should be noted, that the 3D-SIM images are a maximum intensity projection

of the entire cell (500 nm in z), whereas the *d*STORM image picks a specific focal plane within the cell due to the HILO excitation light sheet and is therefore not influenced by contributions from other vertical planes within the sample.

In this 3D-SIM vs. *d*STORM comparison of Vybrant DiD stained LSECs the 3D-SIM reconstructed super-resolution image clearly depicts fenestrations arranged in sieve plates. Only the area in the immediate vicinity of the nucleus lacks fenestrations (see Figure 5.3 (a) and Figure 5.3 (c)). A clear resolution gain can be observed in the corresponding *d*STORM image. Although the cell was illuminated at a slightly inclined angle in HILO mode, the *d*STORM reconstruction (which does not use cylindrical lens-induced astigmatism to enable 3D reconstruction) produces a pure 2D image[2]. Here, Vybrant DiD labeling shows excellent membrane specificity and appears to be devoid of background contributions (Fig 5.3 (b), 5.3 (d)).

5.3. Rapid multi-color 3D-SIM overviews combined with super-resolution of SMLM

The ability of 3D-SIM to rapidly create a large super-resolved overview of a sample is demonstrated in Figure 5.4 (a). It shows seven 3D-SIM images of several multi-color labeled LSECs, stitched together using Fiji to provide an overview of all cells within a specific sample location (Figure 5.5).

This is very useful because 3D-SIM is limited in its maximum field of view (41 x 41 μm^2) by the objective lens that is used to create the illumination pattern at the sample. The sample location is moved each time by approx. 40 µm laterally which enables us to rapidly acquire images with a small overlap that can then be stitched together to a single overview image. This huge super-resolved overview is used to identify areas of interest for even higher-resolution *d*STORM imaging, which is considerably more time-consuming than 3D-SIM.

Here for example a specific area of interest, i.e. a collection of sieve plates, is outlined by the dashed box in Figure 5.4 (a). To permit a direct comparison, Figure 5.4 (b) shows an enlarged view of the region of interest in the 3D-SIM image, while Figure 5.4 (c) shows the subsequently acquired *d*STORM image of the tubulin structures stained with an Alexa Fluor 647 coupled to antibodies (primary + secondary). Figure 5.4 (d) shows an overlay of the 3D-SIM tubulin channel (magenta) with the *d*STORM tubulin image (green), and a line section is identified, which is shown in Figure 5.4 (e). By this direct comparison one can clearly see that *d*STORM reproduces the tubulin fibers with much finer structural detail due to its high spatial resolution. It is also remarkable that in some locations the tubulin fibers appear as double-track structures of about 40 nm width (see Figs. 5.4 (d) and 5.4 (e) in the *d*STORM reconstructions. The reason for that is the thin illumination sheet and linear polarization used for *d*STORM excitation excites those fluorophores more efficiently that are attached to either side of tubulin by

[2]As the fit algorithm used in SMLM provides the FWHM of the PSF fitted to the emitters, it can easily reject out-of-focus emitter, as their PSF widens due to defocusing.

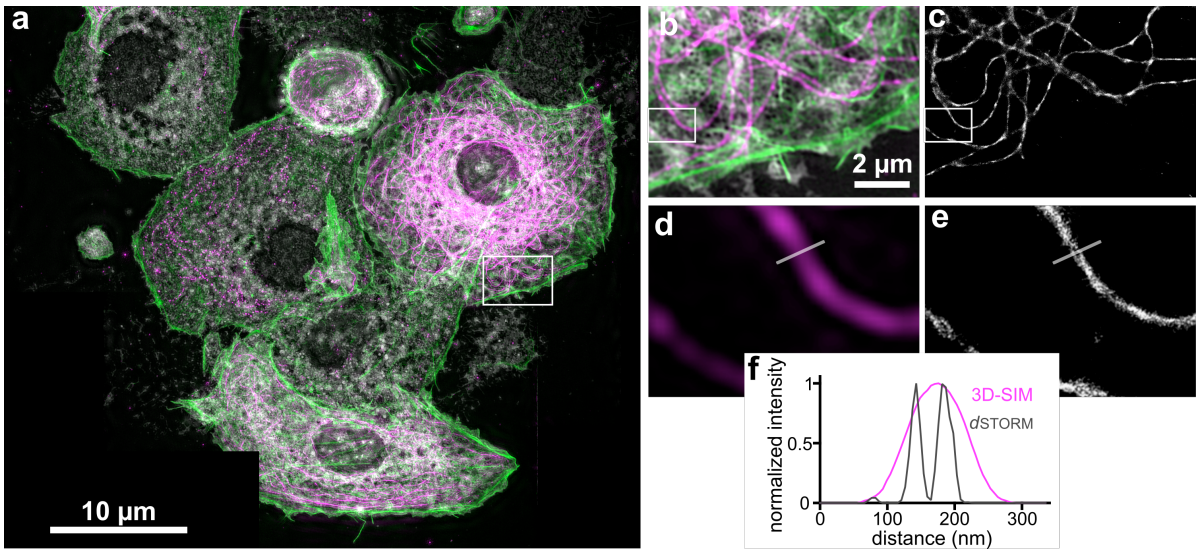

Figure 5.4.: Stitching of multicolor 3D-SIM super-resolution images aids in the search for sieve plates in LSECs. (a) Seven multi-color maximum intensity z-projection 3D-SIM images of LSECs were stitched together to produce a large-scale overview image. The fixed rat LSECs were stained for membranes (CellMask Orange, white), actin (Phalloidin-AF488, green) and tubulin (mouse anti-*beta*-tubulin and anti-mouse- AF647 antibodies, magenta). Scale bar: 10 µm. (b) Enlarged view of the ROI shown in (a). Tubulin is shown in magenta. (c) Corresponding *d*STORM reconstruction of the tubulin network. (d) Zoomed view of the *beta*-tubulin channel (magenta) outlined in the 3D-SIM image in (b). (e) Corresponding *d*STORM image of *beta*-tubulin. The line indicating the location of the cross-section has a length of 330 nm. (f) The line sections of the 3D-SIM and *d*STORM tubulin channels show the resolution enhancement achieved by *d*STORM (green line) compared to 3D-SIM (magenta line). The exposure time for a single *d*STORM frame was 20 ms. 10000 frames were used for the reconstruction.

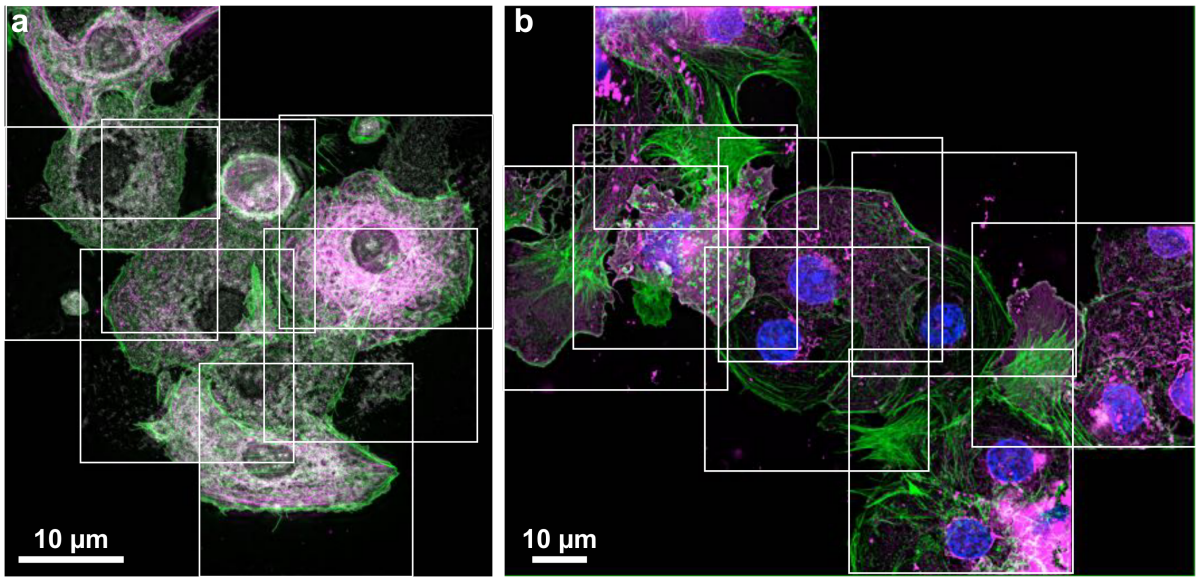

Figure 5.5.: Single images for stitching process are marked for (A) Figures 5.4 and (B) 5.6

the primary-secondary antibody system rather than the fluorophores that are attached along the vertical direction.

Compared to membrane imaging *d*STORM imaging of distinct cellular structures such as microtubules can be achieved more readily because the labeling density is restricted to only a single optical plane (for very flat cells). Accordingly, our resulting images showed highly resolved tubulin structures,(Figure 5.1 and Figure 5.4) that were well defined in isolated filaments but slightly less so at points where crossing filaments overlap. This is one effect of the low laser powers available in this setup, as the lack of laser power leads to a maladjustment of the blinking rate of the fluorophores especially in the areas of higher fluorophore density such as microtubules crossings.

5.4. Correlation between the membrane and cytoskeleton in LSECs

In order to determine if there is a connection between the plasma membrane of the fenestrations and the actin cytoskeleton I compared super-resolution fluorescence images collected by both super-resolution techniques (Figure 5.6).

Figure 5.6 (a) is a large multi-color image of several stitched 3D-SIM measurements with a total size of 125 µm x 105 µm (Figure 5.5). In this overview different constituent parts of the LSECs are stained: the nuclei (DAPI, blue), actin filaments (Phalloidin-AF488, green) and the plasma membrane (Vybrant DiD, red). Fig 5.6 (b) shows an enlargement of the ROI highlighted in Figure 5.6 (a), representing two LSECs in close contact. The fenestrations are arranged in sieve plates as visualized by the membrane stain in the 3D-SIM image. The actin filament is highly resolved and appears to surround the fenestrations. The plasma membrane of the same ROI was also imaged by *d*STORM (Figure 5.6 (c)). An overlay of the 3D-SIM channels with the *d*STORM image is shown in Figure 5.6 (d) and was further analyzed by displaying a line section that allows one to better judge the degree of overlap between the different cellular constituents (Figure 5.6 (e)). The line section shows that the actin cytoskeleton co-localizes well with the membrane stain obtained by *d*STORM while the 3D-SIM membrane signal lacks the resolution to truly make this conclusion.

This shows again that the combination of two super-resolution optical modalities on the same setup fuses the great practical abilities of 3D-SIM, which makes it so attractive for rapid multi-color bioimaging, with the significantly higher spatial resolution of *d*STORM. 3D-SIM enables fast (0.5 s for a 0.8 µm stack) three-dimensional measurements with a lateral spatial resolution of about 100 nm in up to 4 different color channels. It allows for rapid scanning of large sample areas with subsequent image stitching in software to compose large super-resolved overview images. After pre-scanning samples with SIM, *d*STORM imaging of selected ROIs permits us to revisit selected sample locations with even higher spatial resolution. In the commercial system I used, the built-in autofocus unit supports the stability in the vertical direction to avoid drift, while drift in the lateral direction could be corrected afterwards in the reconstruction software. Re-

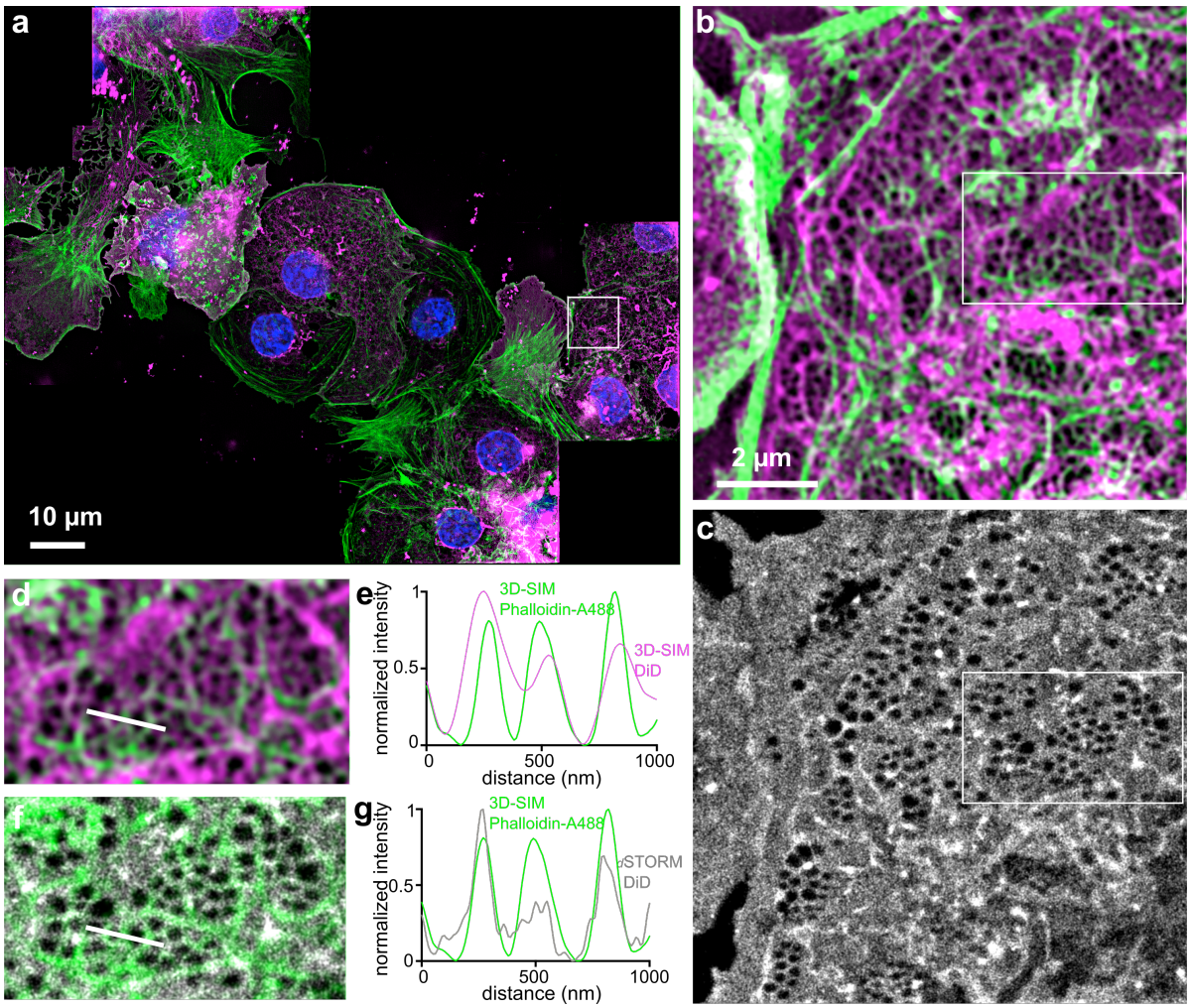

Figure 5.6.: Comparison of cellular features imaged by different super-resolution microscopy modalities: (a) Nine multi-color maximum intensity z-projection 3D-SIM images of fixed rat LSECs were stitched together to produce this overview image. The cells were stained for nuclei (DAPI, blue), actin (Phalloidin- AF488, green) and membrane (DiD, magenta). (b) Enlarged 3D-SIM view of the ROI shown in (a) highlighting how fenestrations are surrounded by actin fibers. (c) is the corresponding *d*STORM image of the DiD membrane channel. (d) is an enlarged view of the ROI shown in (b). (e) Plot of the line section shown in (d) comparing the actin (green) and membrane (magenta) channels of the 3D-SIM image. (f) Overlay of the actin channel from 3D-SIM (d) shown in green and the membrane channel of *d*STORM ((c), outlined box) shown in gray. (g) Plot of the line section shown in (f) comparing the 3D-SIM actin (green) and *d*STORM membrane (gray) channels. (g) The actin line (green) shows the same trend as the membrane *d*STORM line (gray), which suggests that actin filaments support fenestrations.

markably, multi-color staining of LSECs clearly shows that the microtubules appear to surround and separate sieve plates (see Figure 5.4 (b)), while actin filaments surround each fenestration within a sieve plate (see Figure 5.6 (d)). This further confirms the hypothesis that the cytoskeleton is of great importance for either stabilizing or even defining fenestrations in LSECs such as mentioned in chapter 3.1. From the *d*STORM/3D-SIM

	3D-SIM	*d*STORM
Lateral resolution	100 nm	10 - 40 nm
Acquisition time	1 - 10 s	10 - 15 min
Fluorophores	photostable as possible	photoswitchable / photoconvertable
Buffer system	matching refractive index (glycerol, Vectashield)	photoswitching buffer (MEA, enzymes,..)
Live cell imaging	possible, but depending on dyes, buffers, sample contrast...	restricted due to long acquisition times and high laser intensities
Comments	reconstruction bears risk of artifacts, algorithm assumes a perfectly matched PSF (matching immersion oil is important)	labeling density critical, performs better on particles- and filaments-, membrane-imaging (negative contrast) is difficult

Table 5.1.: The table concludes the advantages and disadvantages of 3D-SIM and SMLM. SMLM gains better resolution using specialized dyes and buffers, while 3D-SIM can reach much higher acquisition rates with any dye.

overlay image and corresponding line section shown in Figures 5.6 (d) and 5.6 (e) it can be seen that the actin filaments appear to build a scaffolding that surround and possibly support the fenestrations. The tubulin structures create borders for fenestrations that assemble in sieve plates, while actin appears to stabilize the membrane which is extremely thin in these areas.

In conclusion both techniques have advantages and disadvantages that are illustrated in table 5.1.

6. Fluorescence stains and their effect on living cells

The biggest challenge in imaging living cells is to find a suitable dye that can stain the required region. This dye needs to be bright and stable and should not influence the functionality of a target or the viability of the cell. As shown in previous chapters CellMask Deep Red and CellMask Orange turned out to be excellent SIM and STORM dyes for fixed cells. But testing them on living cells (U2OS) already shows a huge influence on the viability of cells as the cells started blebbing very fast. Membrane blebbing is a first indication of poor cell health and often leads to cell death. Interestingly the cells outside the illuminated area have not been affected by this, so the conclusion is that CellMask dyes in combination with laser illumination leads to blebbing, and subsequently to cell death. There are many possibilities to fluorescently stain a cell's plasma membrane. Many of those dyes are readily commercially available and especially described as compatible with fixed and live cell staining. In this chapter I describe the testing and the application of several dyes for the staining of LSEC membranes and their suitability for fixed and live cell measurements.

6.1. The plasma membrane

The plasma membrane of a mammalian cell is about 8 nm thick and its principal components are lipids and proteins while carbohydrates also play an important role. The structure of the cell membrane is depicted in the liquid mosaic model in Figure 6.1. Phospholipids are the most common lipids and form the lipid bilayer. They are amphiphatic molecules and therefore have a hydrophilic and hydrophobic region. The membrane proteins are embedded in the phospholipid bilayer and protrude from it with their hydrophilic parts.

There are several possibilities to stain the membrane of a cell. Either the membrane is stained by intercalating dyes (see chapter 6.2.3) or molecules on the membrane are densely labeled for a homogenous stain. Sugar molecules (glycoproteins), for instance, are distributed all over the membrane surface, which can be stained by lectins (see chapter 6.2.1).

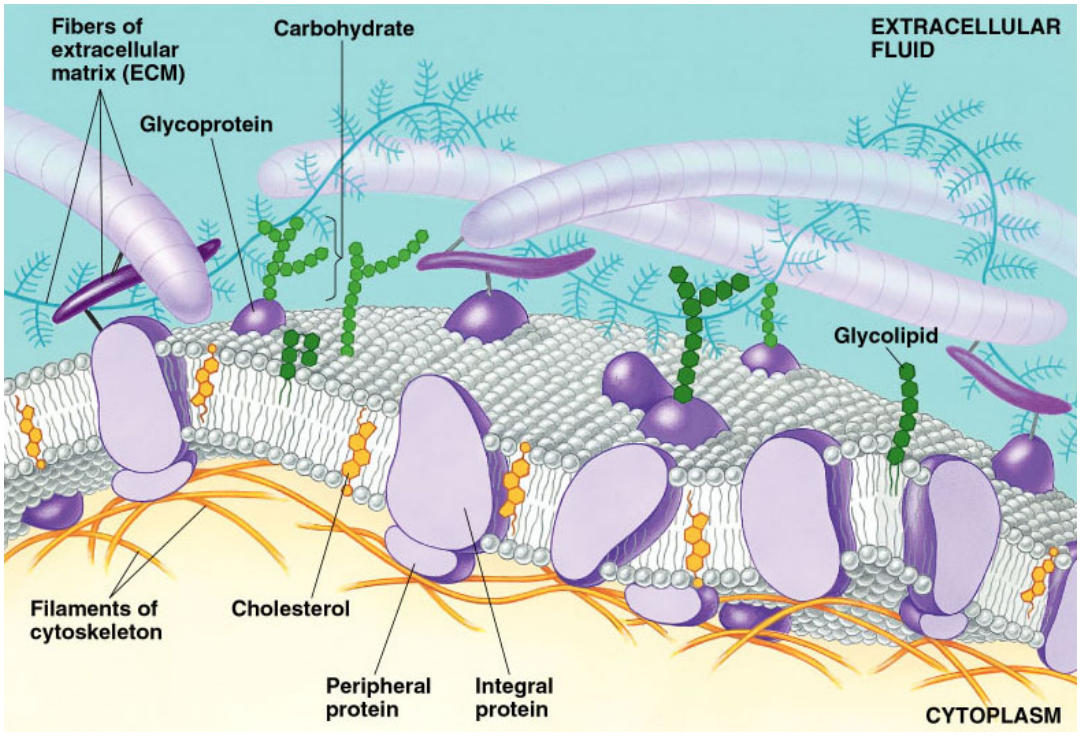

Figure 6.1.: Structure of the plasma membrane of a mammalian cell (from [83], p. 168)

6.2. Lectins

6.2.1. Wheat germ agglutinin

There are several types of fluorescent lectins commercially available, e.g. Wheat Germ Agglutinin (WGA) conjugated to Alexa Fluor dyes. WGA is a lectin which binds selectively to N-acetylneuraminic acid and N-acetylglucosamine residues [84]. It is typically used for detecting glycoconjugates in flow cytometric and in histochemical applications as well as standard microscopy. Xie et al. found out that WGA binds preferentially to periportal LSECs (in mouse) and that it is colocalized to CD45 rich regions [85].

I initially used WGA Alexa Fluor 647 to stain the membrane sugars in the hope of obtaining an even membrane stain for imaging the fenestrae of LSECs in 3D-SIM. A typical, representative result is seen in Figure 6.2. As a control the membrane is also stained with CellMask Orange, as CellMask dyes turned out to be very reliable dyes for fixed cells (as mentioned in the previous chapters) and serves as indicator for a successful membrane stain in comparing different stains.

In Figure 6.2 (a) an entire LSEC can be seen, with all its fenestrations arranged in sieve plates and both stainings as a composite. CellMask Orange is shown in green while WGA-Alexa Fluor 647 is depicted in red. In 6.2 (b) the ROI is enlarged and (c) and (d) show the particular stainings (CellMask: green, (c) and WGA: red, (d)). The magnification illustrates the differences in the stainings. CellMask stains the membrane very well in (c), showing a sieve plate with its fenestrations, while the WGA-stain of

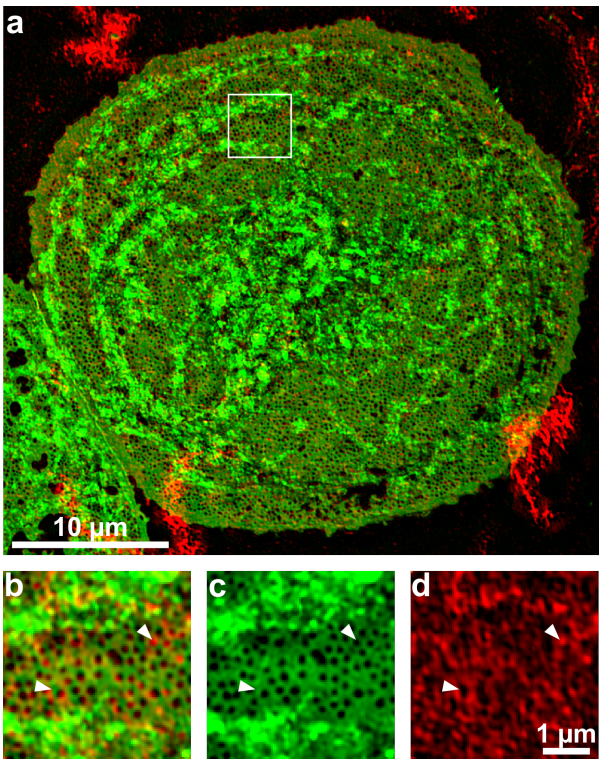

Figure 6.2.: 3D-SIM maximum intensity projection image (B.3) of a fixed LSECs stained for the plasma membrane: (a) Overview composite of CellMask Orange (green) and WGA-Alexa Fluor647 (red) stained LSECs. ROI is presented in (b) as an overlay, in (c) the CellMask Orange channel and (d) the WGA Alexa Fluor 647 channel. The arrow heads mark an apparent difference between both stainings; in both channels holes appear that do not co-localize. CellMask Orange appears to define fenestrations and sieve plates well whereas the WGA-signal seems to be randomly distributed.

the same region appears totally random. The arrowheads show examples for the lack of colocalization of the stains: Either there is a hole in the WGA whereas in the CellMask channel there is a closed membrane (left arrowhead) or in the CellMask channel defined fenestrations can be seen which are filled with WGA in the red channel (right arrowhead). Experiments with *d*STORM of WGA-Alexa Fluor 647 also showed similar results of entirely randomly distributed dye over the entire membrane. Therefore, the lectin WGA and its conjugates were deemed to not be suitable for homogenous membrane-staining of LSECs for super-resolution studies.

6.2.2. *Ulex europaeus* agglutinin

An excellent marker for human endothelial cells is *Ulex europaeus* agglutinin. ULEX is a lectin that binds to many glycoproteins and glycolipids with a preference for α-linked fucose residues [86]. To investigate the ability for membrane staining I stained fixed LSECs with a lectin from *Ulex europaeus* conjugated to FITC together with CellMask Orange.

The result of this experiment is shown in Figure 6.3. The composite of both stains is

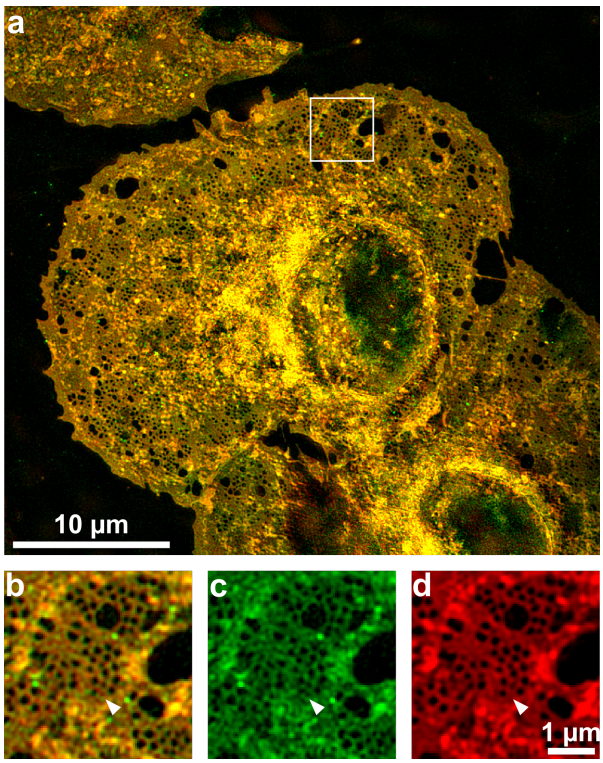

Figure 6.3.: 3D-SIM maximum intensity projection image (B.3) of fixed LSEC plasma membrane stained with ULEX-FITC: (a) Overview Composite of ULEX-FITC (green) and CellMask Orange (red) stained LSECs. ROI is presented in (b) as an overlay, (c) ULEX-FITC channel and (d) CellMask Orange. The arrow head marks an appearing difference between both stainings; in the green channel there are two fenestrations which are not present in the red channel.

seen in Figure 6.3 (a). The frozen LSECs were thawed (see chapter 3.4) and fixed after 3h culture on collagen coated glass. In (b) the ROI of an overlay of both channels is pictured, while the representation of the ULEX-FITC (green) (c) and of the CellMask Orange (red) (d) clarifies the differences between both stains. The arrow head e.g. shows an area where fenestrations appear in the green channel but not in the red channel. This is either result of the better resolution in the shorter wavelength range compared to the longer wavelength range or the staining with ULEX is not as dense as CellMask which gives false positive results for this negative contrast. Another observation is that fenestrations in the ULEX stain do not appear as round as they appear in the CellMask channel. This could, again, be due to the better resolution of the green channel. This result has some similarities to the *d*STORM measurements of LSECs which also revealed a non-circular shape of fenestrations which was also confirmed by scanning electron microscopy. Another reason could be that the ULEX cannot stain samples with a comparable distribution as the CellMask membrane stain. This would lead to thinner membrane bridges between fenestrations and therefore to less overlapping dye molecules which would show smeared and apparently roundish fenestrations.

In conclusion, ULEX applications on fixed LSECs show promising results, but the main goal is the use of ULEX as a dye for live-cell imaging. Unfortunately, for this

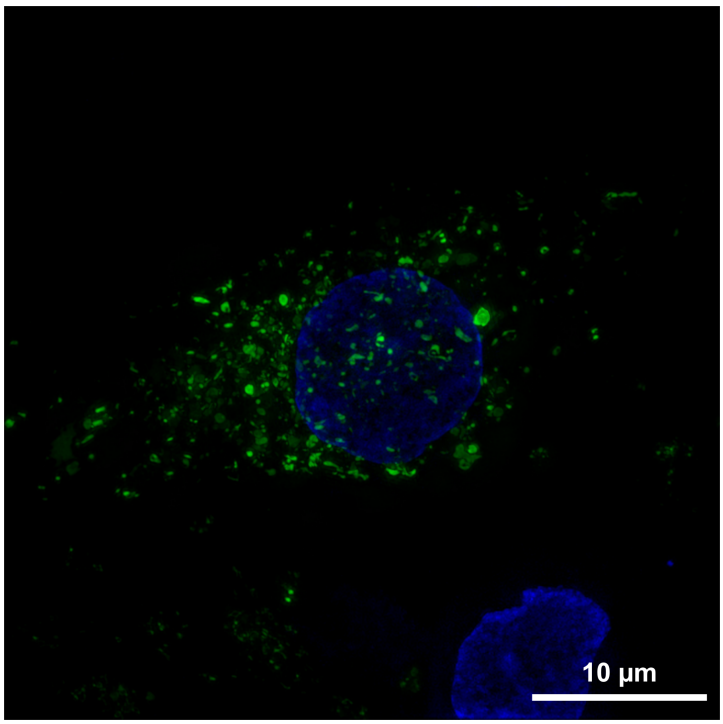

Figure 6.4.: 3D-SIM maximum intensity projection image of living LSEC stained with ULEX-FITC. The fluorescent lectin does not remain at the plasma membrane but appears to be internalized rapidly by the cell.

application the result is seen in Figure 6.4. As mentioned in chapter 3.1, LSECs have high endocytic activity. Receptors at the surface, such as DC-SIGN contain a lectin binding domain and will lead to the uptake of its ligand. A few minutes after treating living LSECs with ULEX-FITC, the dye was already taken up thus completely failing to stain the plasma membrane. Therefore it is not possible to use ULEX-FITC for longterm live membrane staining of these cells, yet.

6.2.3. Intercalating dyes

CellMask

For the work presented in chapter 5 I already used two different intercalating dyes to show the comparative imaging of *d*STORM and 3D-SIM. CellMask Deep Red and Vybrant DiD turned out to be very well suited even for super-resolution imaging with *d*STORM, which poses some demands on the dyes themselves and the buffer conditions. In summary, Vybrant DiD turned out to be background-free and to provide great photoswitching behavior even with lower laser powers. In contrast, CellMask Deep Red leads to some background even with several washing steps and it requires more laser power to achieve suitable *d*STORM imaging.

Nevertheless, both dyes provided good membrane staining on fixed samples and can be imaged in 3D-SIM very well. The next step is to evaluate the feasibility of staining

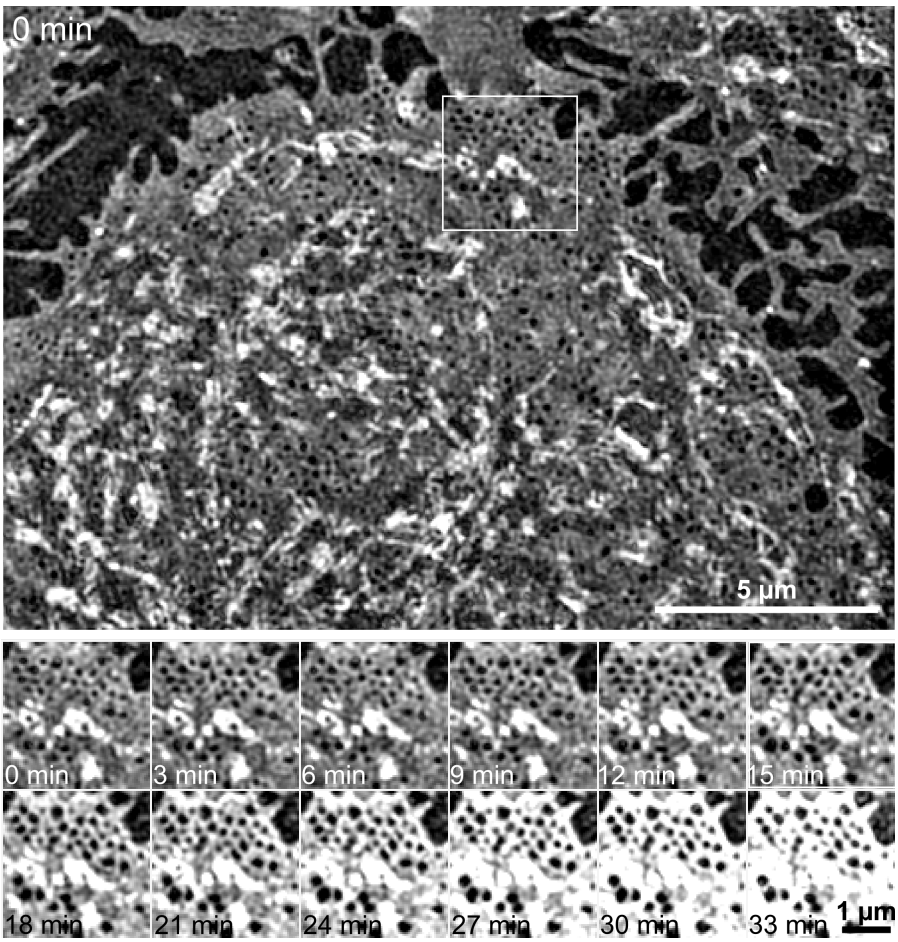

Figure 6.5.: 3D-SIM maximum intensity projection of a living LSEC stained with CellMask Orange as overview (up) and the time lapse of the ROI in the lower two rows after every 3 minutes. The fenestration size and the emission intensity are increasing with time. The cell shows no dynamics at all and seemed stiffed due to the CellMask and illumination.

living LSECs. Preliminary tests were done on the standard cell line U2OS.

These tests with U2OS revealed that CellMask - especially in combination with light exposure - leads to severe damage to the cells. In any case, live cell imaging in 3D-SIM could not be done for a higher number of time points. First, apparent cell movements became frozen and were followed by blebbing. In 3D-SIM imaging of whole cells at least 1 µm imaging depth in z is acquired which requires 8 slices in 125 nm steps. For each z-slice 15 images are recorded to obtain a successful SIM reconstruction. Consequently, at least 120 frames per time point with e.g. 20 ms acquisition time are recorded. This corresponds to 2.4 s illumination per time point, which will induce photochemical effects on the cells and the dye.

To reduce the photodamage, the amount of light exposure can be reduced by either a reduction of laser power (if possible, see B.3) or exposure time. However, to still obtain enough signal for a successful SIM reconstruction, now higher staining concentrations has to be used. The acquisition time may be reduced to 1ms by using a higher stain

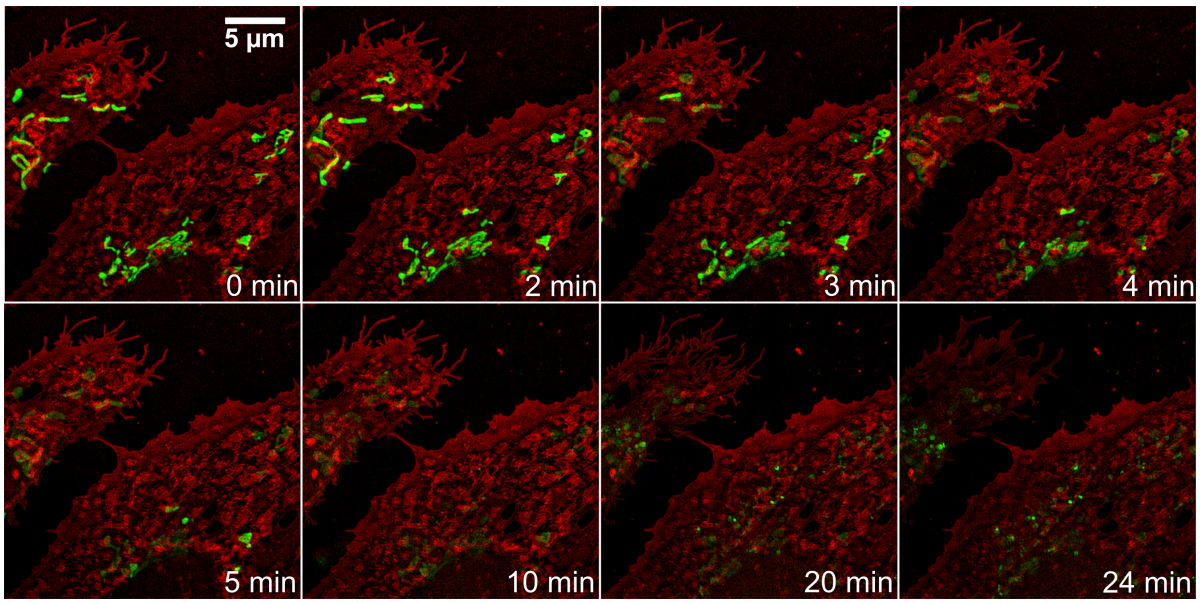

Figure 6.6.: Living LSEC stained with CellMask Deep Red and MitoTracker Red as a time lapse (recorded as 3D-SIM maximum intensity projection). The membrane of the CellMask stained LSEC appears stiff and the MitoTracker Red fluorescence is already rapidly disappearing, pointing to a loss of mitochondrial activity and indicating imminent cell death.

concentration which would decrease the total illumination time to 120 ms. But with a higher intercalating dye concentration, the physical effect (stiffness) on the membrane is much higher, and it will likely become more sensitive to lower laser intensity.

U2OS cells are a widely used immortal cell line originating from osteosarcoma. It carries multiple mutations and chromosomal duplications and translocations. The apparent phototoxicity of CellMask might be particular to these cells and not reflect a general behavior for such stains. LSECs, in contrast to U2OS, are primary endothelial cells with a high sensitivity to ambient environmental changes. The isolation and preparation of LSECs is challenging. Fenestrations arise within the first hours after plating on collagen or fibronectin coated surfaces but, without the addition of factors such as VEGF, they lose these very rapidly after 8 to 14 hours. The observation of fenestration number and shape constitutes a great visual marker for environmental changes. In Figure 6.5 a representative projected 3D-SIM image of a living LSEC is shown. In this sample, the cell density was quite high but the LSECs could still spread out and form their characteristic fenestrations. The staining was performed with a CellMask Orange concentration of 2.5 µg/ml. The bottom row of Figure 6.5 shows a time-lapse acquisition in 3 minute intervals. The illumination was done at 568 nm (10 mW before optics), the acquisition time is 2 ms for each frame (total 9 x 15 = 135 frames) and the represented images are projections of 9 z-slices. The dynamics appear absent, the cells seem to be frozen in its movements. But after several minutes the fenestrations are getting bigger and the emission intensity is increasing (contrast adjustment is the same in every image). The increase in fenestration size could be explained by a compression of the membrane that leads to a compression of the dye and to an increase in the intensity.

To assess the phototoxicity of CellMask, I imaged a living LSEC stained together with MitoTracker Red for an extended time. This dye only stains mitochondria in living cells as it is dependent on the mitochondrial membrane potential. A loss of fluorescence indicates a loss of membrane potential and mitochondrial activity prior to cell death. In Figure 6.6 in timepoints 0 to 5 minutes, before the membrane of the CellMask stained LSEC appears stiff (e.g. no filopodia movement), the MitoTracker Red fluorescence is already rapidly disappearing. The membrane is contracting with time (left cell, 20 min) and blebbs between 20 min and 24 min. These results obviously disqualify CellMask as a universal live cell dye. CellMask shows dramatic consequences for a cell in combination with illumination leading to a rapid cell death.

Vybrant dyes

Another promising dye described in chapter 5 is the Vybrant DiD. As the resolution increases with decreasing wavelength and as I am not depending on the strong 642 nm laser, here, I used Vybrant DiO for live cell 3D-SIM analysis (Figure 6.7).

Figure 6.7 shows a part of a living LSEC stained with Vybrant DiO (upper left). During imaging, the DiO bleaches continuously and exponentially which is shown in the plot (upper right). A time lapse of this cell was taken every 1 minute and is shown for the ROI in the lower rows. The exponential fluorescence decay is corrected for the shown time points with the image processing package Fiji (using an exponential fit and subsequent adjustment).

The viability can be assessed through the very active movements of the filopodia. There is no sign of stiffness compared to the CellMask stained cells. The fenestrations are not getting bigger but they are disappearing (e.g. in the lower region). This is the expectation after temperature decrease (from 37° C to 23° C) and may also be an effect of the illumination. Isolated LSECs have been shown to lose their fenestrations after some time anyway (disintegration effect).

As mentioned in Chapter 5 the Vybrant dye does not lead to background staining of the substrate due to the fact that its fluorescence is increased after intercalating in the membrane (Figure 6.8 and 6.9).

One drawback of the dye is the fast photo-bleaching in 3D-SIM. After 20 time points (under other, gentler, imaging conditions maximum 30 time points) the signal drops to a third and the lack of contrast makes it hard to still define fenestrations. The imaging conditions are chosen in a way to minimize the bleaching effects by adjusting the lowest laser power possible with low acquisition times and still satisfying reconstructions (here 1% of full power 488 nm at 40 ms exposure time, see B.3).

The long-term stability of the dye stored in solution is also a problem. The staining of living cells appears to be very selective. Five months after the initial stock solution was prepared, the staining seems to work on injured cells and non-LSECs only. It was difficult to find suitable cells for the experiments. In order to circumvent these issues, I searched for another dye with similar photophysical properties but works very fast (avoiding long staining procedures) and is intercalating in the unsaturated regions of the membrane [87].

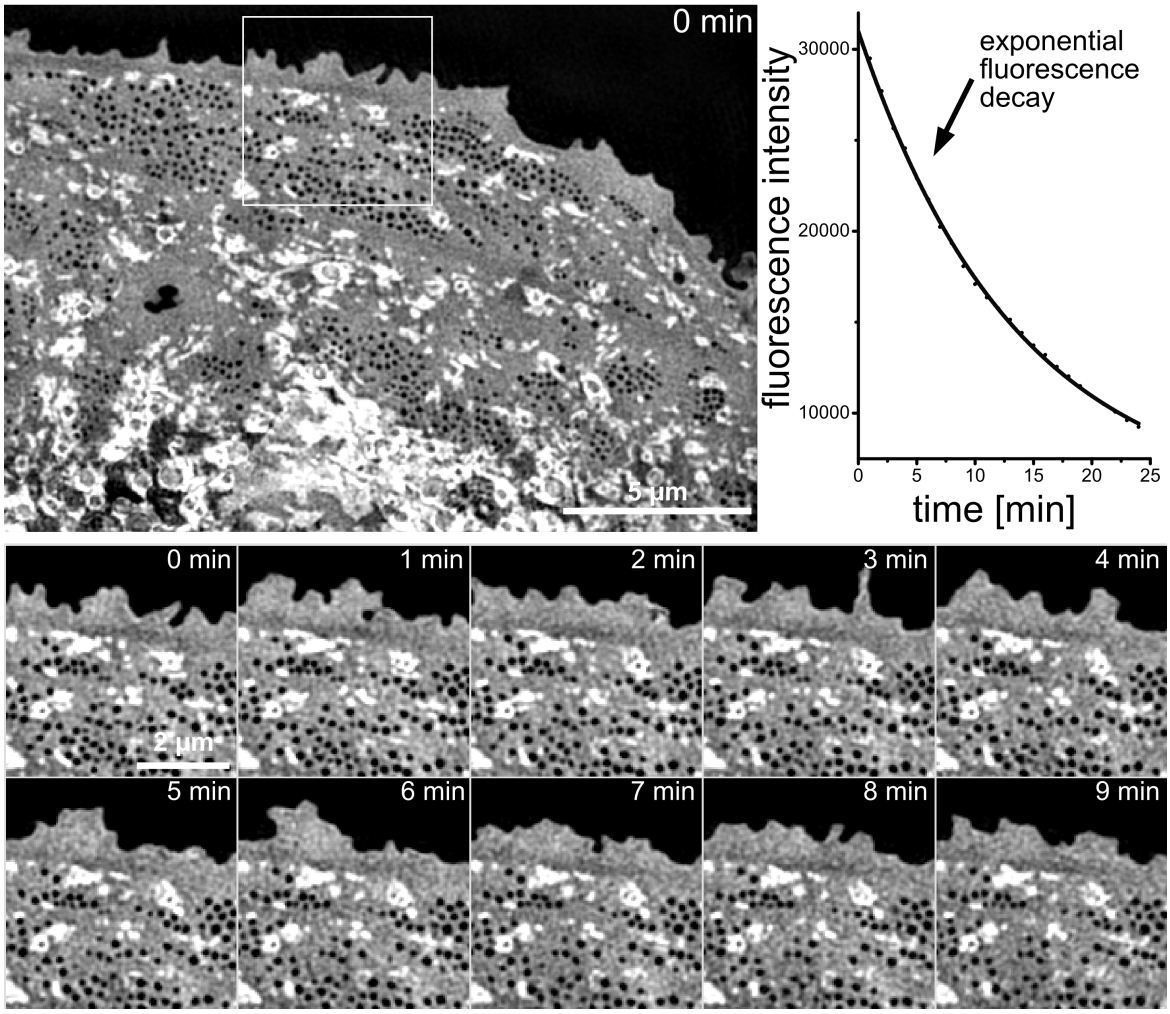

Figure 6.7.: Living LSEC stained with Vybrant DiO as overview (up) and the time lapse of the ROI in the lower two rows for every minute. The plot on the right shows the exponential bleaching over time. The shown time lapse is corrected for this bleaching effect.

FastDiO

Here, FastDiO is described as an unsaturated analog of DiO that migrates up to 50 % faster and shows a high increase in fluorescence when incorporated into membranes.

Unfortunately, the staining with FastDiO turned out to be very inhomogeneous in our experience. The manufacturer protocol with the recommended solutions of 12.5 µg/ml in DMEM resulted in a nearly non-stained sample, on fixed as well as on living cells.

First, the FastDiO stain applied to fixed LSECs shows a stronger affinity for mitochondrial membranes than others. Fixation with paraformaldehyde ruptures the plasma membrane, thus making the staining of all membranes of the cells possible. Consequently, CellMask Orange intercalates in a nearly uniform way into all the membranes of the cells, not only the plasma membrane (Figure 6.10).

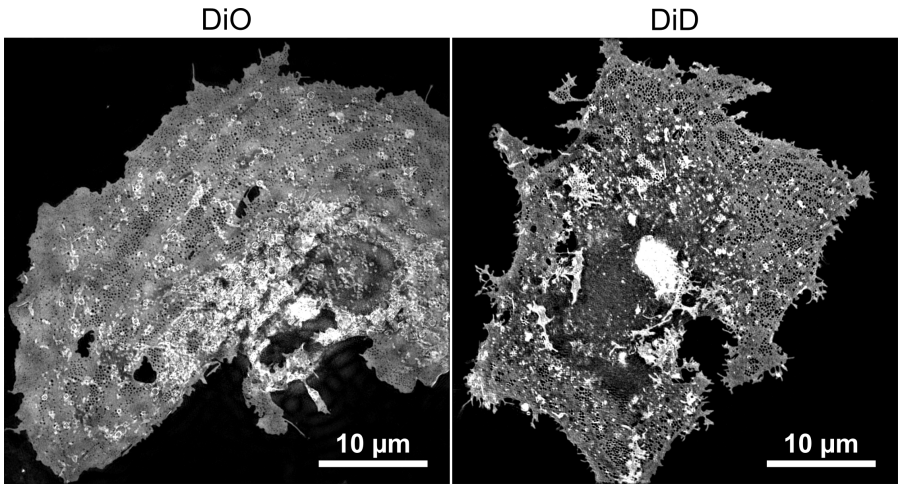

Figure 6.8.: The 3D-SIM maximum intensity projections of living LSECs stained with Vybrant DiO and DiD show very low background, due to the fact that the dye increases its brightness after binding to the membrane.

Applied to live cells, FastDiO only attached to a few apparently damaged/broken cells. A higher concentration of FastDiO applied through dilution in the media did not work out satisfyingly. Therefore, the dye was directly added undiluted to the living cells inside the dish on the microscope. This resulted in a good staining in the region of the dropping point. However, the emission of the stained cells then decreases with distance in intensity at a close range.

Furthermore, I observed that the LSECs close to the dropping point look disrupted and stressed. The filopodia look frayed and the fenestrations are strongly increased in size. My hypothesis is that the FastDiO staining process is responsible for this phenomenon, and that this is not caused by an unsuccessful LSEC isolation procedure, grew stronger with the experiment shown in Figure 6.11. Figure 6.11 (a) shows a part of a living isolated rat LSEC stained with a moderate CellMask Orange concentration and imaged with 3D-SIM. The peripheral zone of the LSEC has fenestrations of a reasonable size (100-200 nm). In Figure 6.11 (b) the same cell at the same position is shown after adding 2 µl of FastDiO-DMSO solution to this region of the dish. The image is recorded under the same conditions in the CellMask Orange channel right after adding the DMSO dye mixture directly to 500 µl RPMI medium. The effect is quite obvious: the fenestrations are nearly destroyed and their size increased instantly to an about 5 times larger diameter. The plasma membrane looks battered and shredded and membrane tatters lie above an actin skeleton which is still intact and stable at this time point. The assumption is that DMSO has an instantaneous effect on the membrane such as a 'bursting balloon' while the visible effect on actin is much slower and does not appear within a few minutes. The membrane also appears contracted which leads to a higher dye density and a stronger emission signal. The LSEC appearance can be compared to figure 6.5 where the fenestration size and emission of the CellMask stain increases with continuous illumination. It is known that DMSO is toxic to living organisms down to single cells. Studies show strong influence on cell viability already at 1 % DMSO concentration in

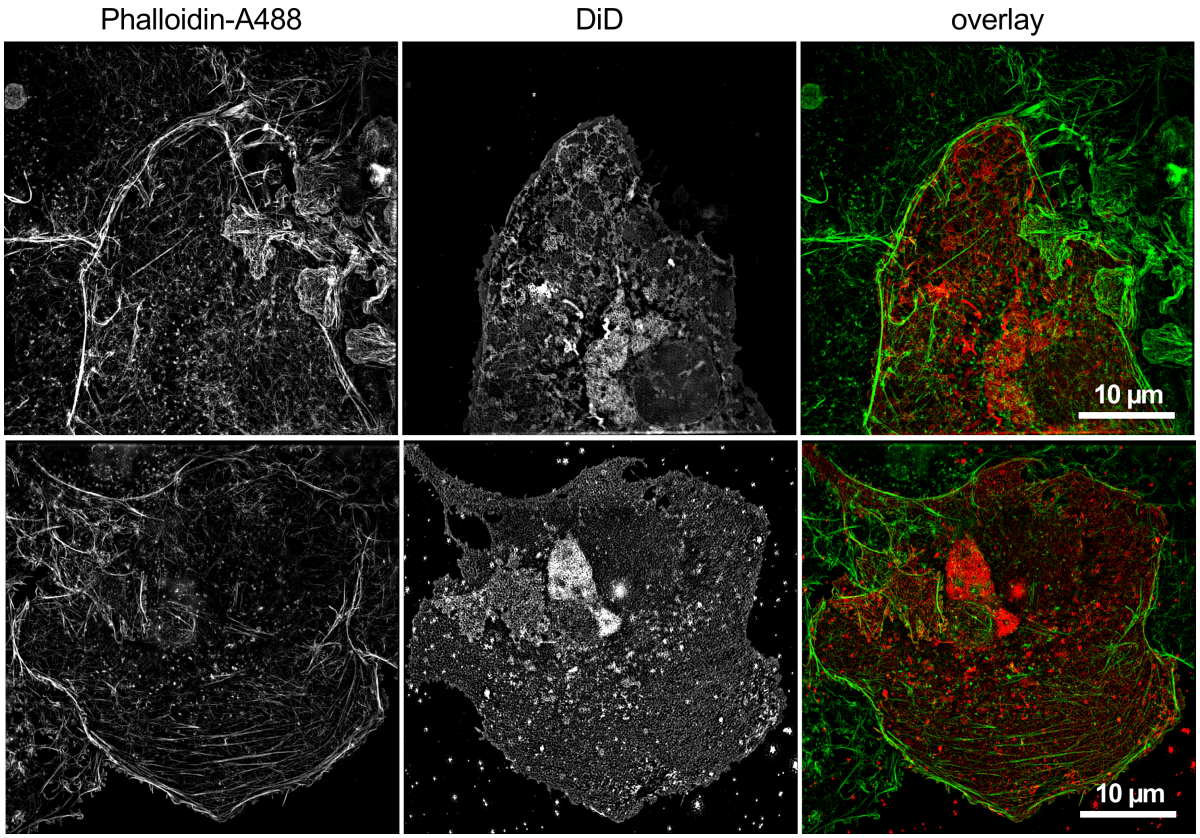

Figure 6.9.: 3D-SIM maximum intensity projections of fixed LSECs stained with Vybrant DiD. Two densely plated LSECs areas are shown stained for Actin filaments with Phalloidin-Alexa488 (green) and Vybrant DiD (red). The individual channels and the overlay are shown. Vybrant DiD shows no background in unstained regions. On the other hand, after a few months of storage, the solution appears to stain cells selectively in a non-uniform way. In both depicted regions, several cells are present and stained for Actin, whereas only one cell is intercalating Vybrant DiD successfully.

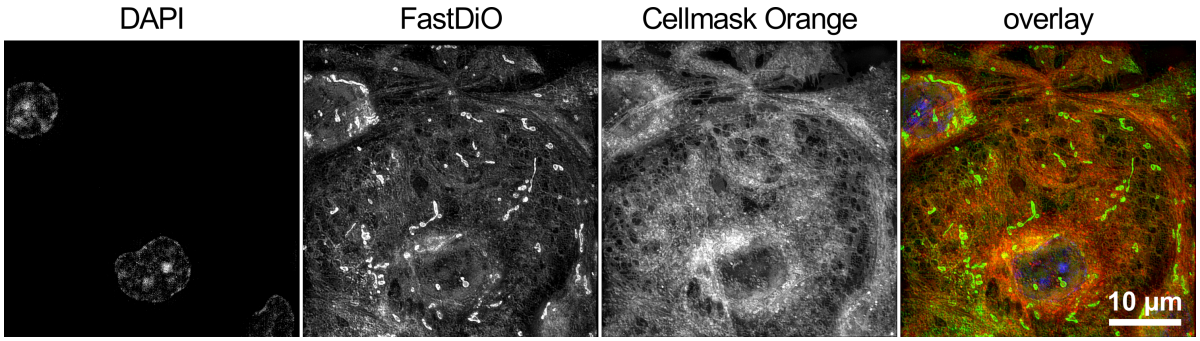

Figure 6.10.: Comparison of FastDiO and CellMask Orange staining of fixed LSECs imaged by 3D-SIM. FastDiO and CellMask Orange do not have the same staining affinities for different types of membranes. An overlay and the individual channels of the nuclear DAPI, FastDiO and CellMask Orange stains are shown. FastDiO appears to intercalate well in mitochondrial membranes leading to a strong signal whereas CellMask Orange depicts a more uniform global membrane stain.

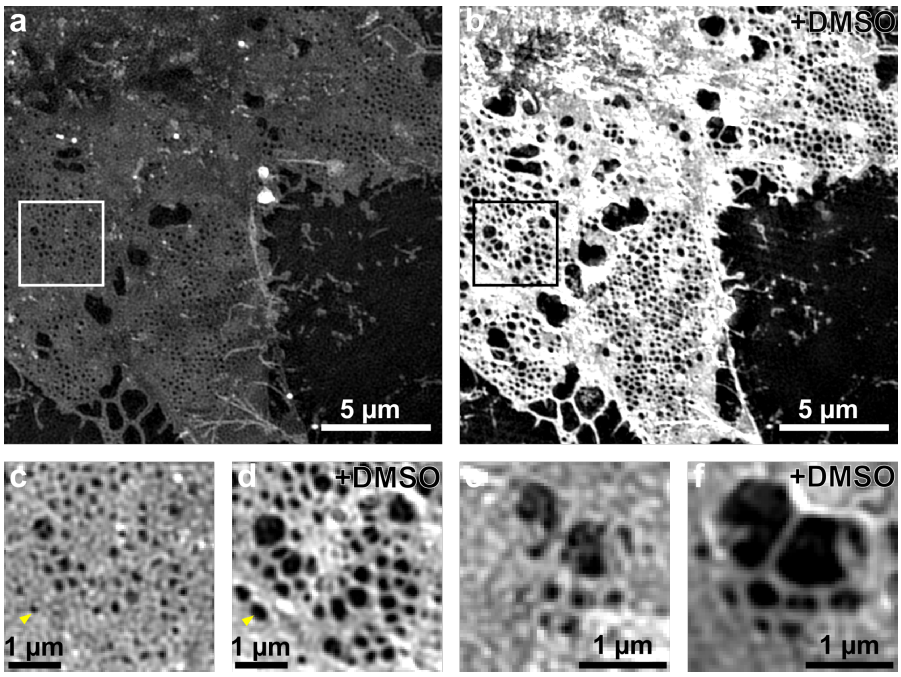

Figure 6.11.: Effect of DMSO on LSECs. (A) 3D-SIM maximum intensity projections of live rat LSEC stained with CellMask Orange at a low concentration. (B) The same cell imaged about 5 minutes after addition of 2 µl (5 µg) of FastDiO DMSO stock solution show highly increased fenestrations.

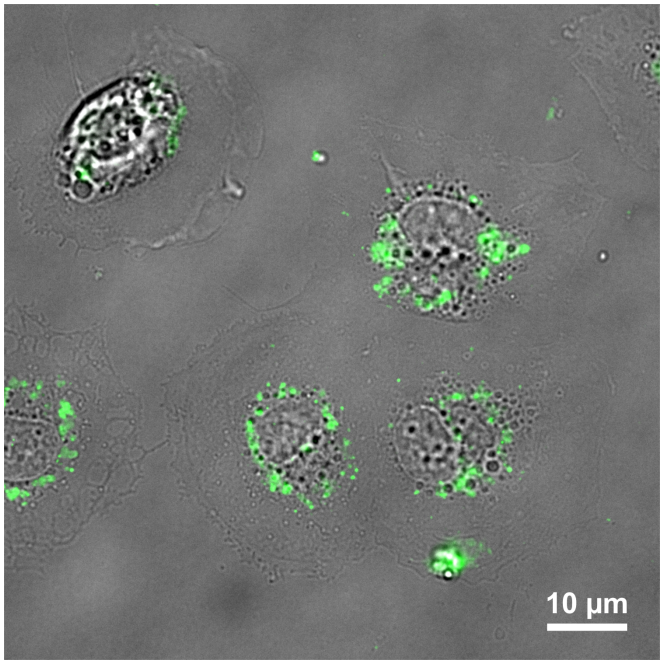

Figure 6.12.: . FastDiO wide-field epi-fluorescent signal (green) overlayed with the corresponding, non fluorescent differential interference contrast conventional image (gray) on living LSECs after a few minutes incubation. Apparently FastDiO can be rapidly endocytosed by live LSECs

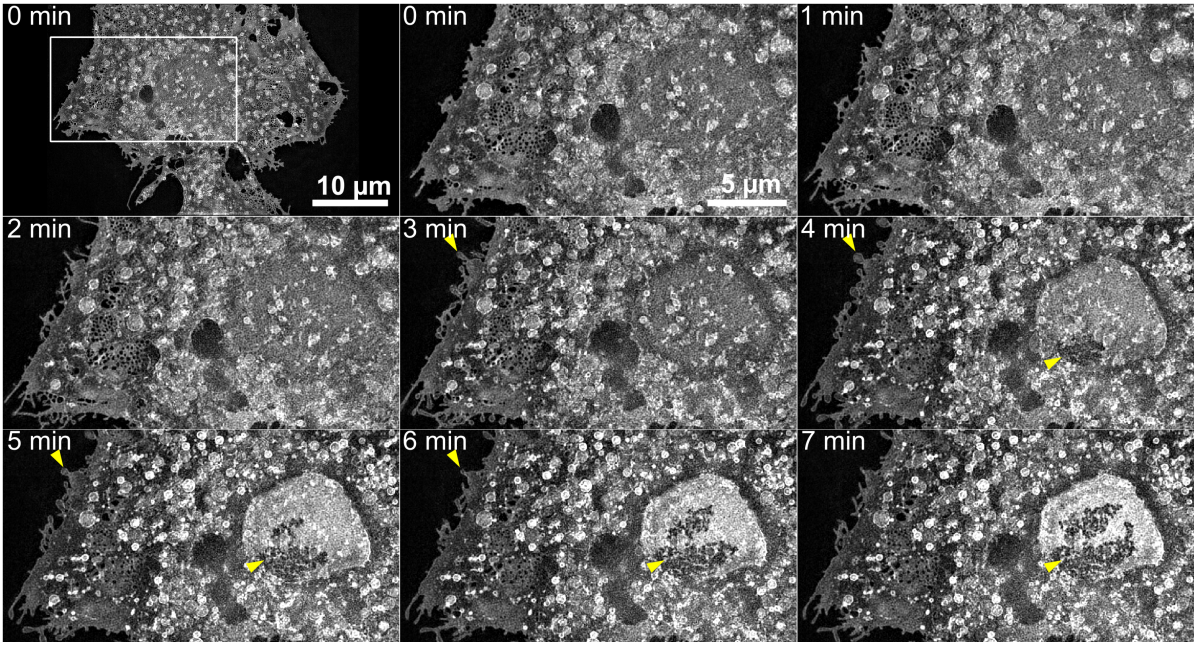

Figure 6.13.: Blebbing of a LSEC due to FastDiO staining. 3D-SIM of a FastDiO stain LSEC images every minute. Images shown here are a maximum intensity projection of a 1 µm thick z stack. Top left images shows the cell at the beginning of the time series. The other images depict the region of interest drawn on the first panel at the indicated time points. The yellow arrow indicates a point of blebbing of the plasma membrane at a filopodia.

the medium [88, 89]. By dropping DMSO to the cells directly without any premixing the DMSO concentration is strongly increased locally as DMSO sinks 'nearly straight' down because of its slightly higher density than water (1104 kg/m^3 vs. 1000 kg/m^3).

In addition to the lack of homogenous membrane affinities, selective cell staining that appears to correlate with the prolonged storage of the stock solution and DMSO related toxicity at high local concentration, FastDiO can be incubated with cells at non-toxic concentrations. Fast DiO is then endocytosed by living LSECs. This results in the obvious absence of the stain at the plasma membrane in favor of very bright internal vesicles located around the nucleus (Figure 6.12).

Even cells that appear not to be directly affected by DMSO poisoning suffer during the imaging process, due to light exposure and subsequent phototoxicity effects. Figure 6.13 shows a time series of a FastDiO stained living LSEC. The cell at time point 0 appears already slightly disrupted but still has fenestrations of the expected size and sieve plates.

With time the fenestrations are increasing in size and begin to disappear and after 3 to 6 minutes as blebbing of the outer regions of the cell starts. The filopodia indicated with a yellow arrow in Figure 6.13 starts to blow up and burst like a balloon.

The membrane at the nucleus starts to change at minute 4. Ruptures are spreading over the entire nucleus until minute 7. The damage to the nuclear membrane is a clear indication for the very bad health condition of the cell. Even though scattered fenestrations are still visible, the cell shows clear signs of occurring cell death. Another

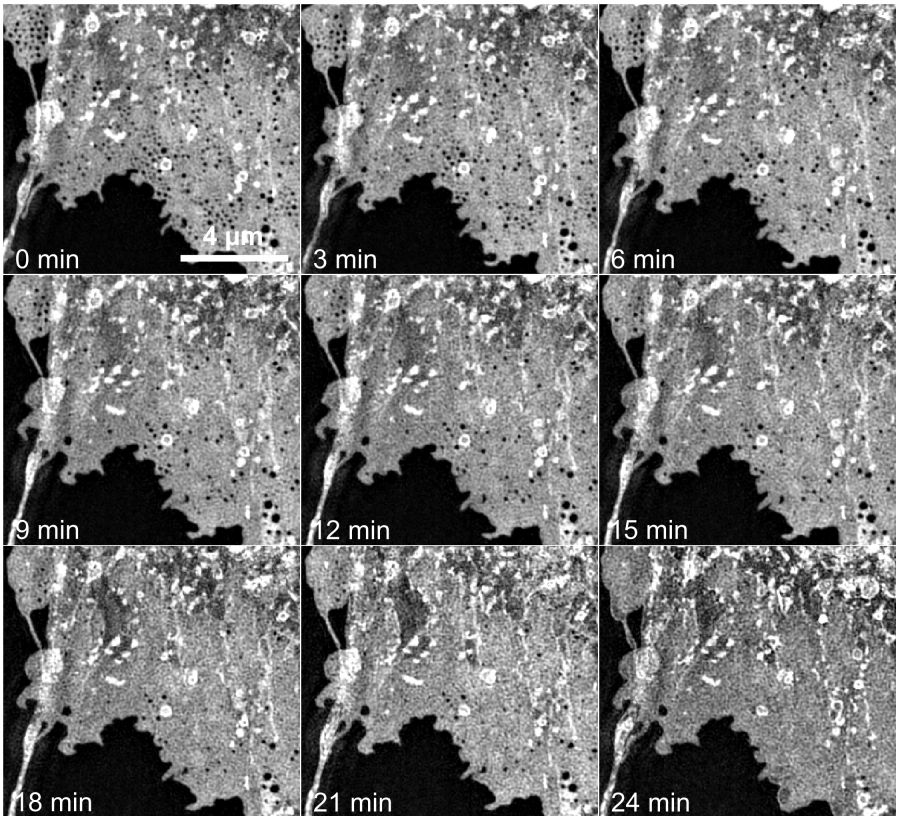

Figure 6.14.: 3D-SIM time series of a FastDiO labeled LSEC shows the rapid loss of fenestrations over time.

observation after the staining with FastDiO could be made over a time range of about 1 hour. After some time all LSECs in the sample lost their fenestrations, leaving lower areas within sieve plate size behind but with closed membranes. This process of losing fenestrations is presented in Figure 6.14.

The time lapse of a small area of a FastDiO stained LSEC shows the disappearance of fenestrations over a time range of 24 minutes, leaving an apparently closed homogenous membrane area behind. At minute 24 the blebbing starts at the lower right corner of the image. This indicates a significant stress acting on the cell, especially due to the light exposure during this time lapse. However, the disappearance of the fenestrations was observed in all LSECs in this sample over time, including those that were not illuminated. While in all our experiments the LSECs are losing their fenestrations within 10-16 hours after isolation from the rat, this effect did not lead to lowered membrane areas within sieve plates as seen in the FastDiO staining experiments.

In conclusion, FastDiO did not result in satisfying and reproducible live cell experiments, thus making it unsuited for these applications.

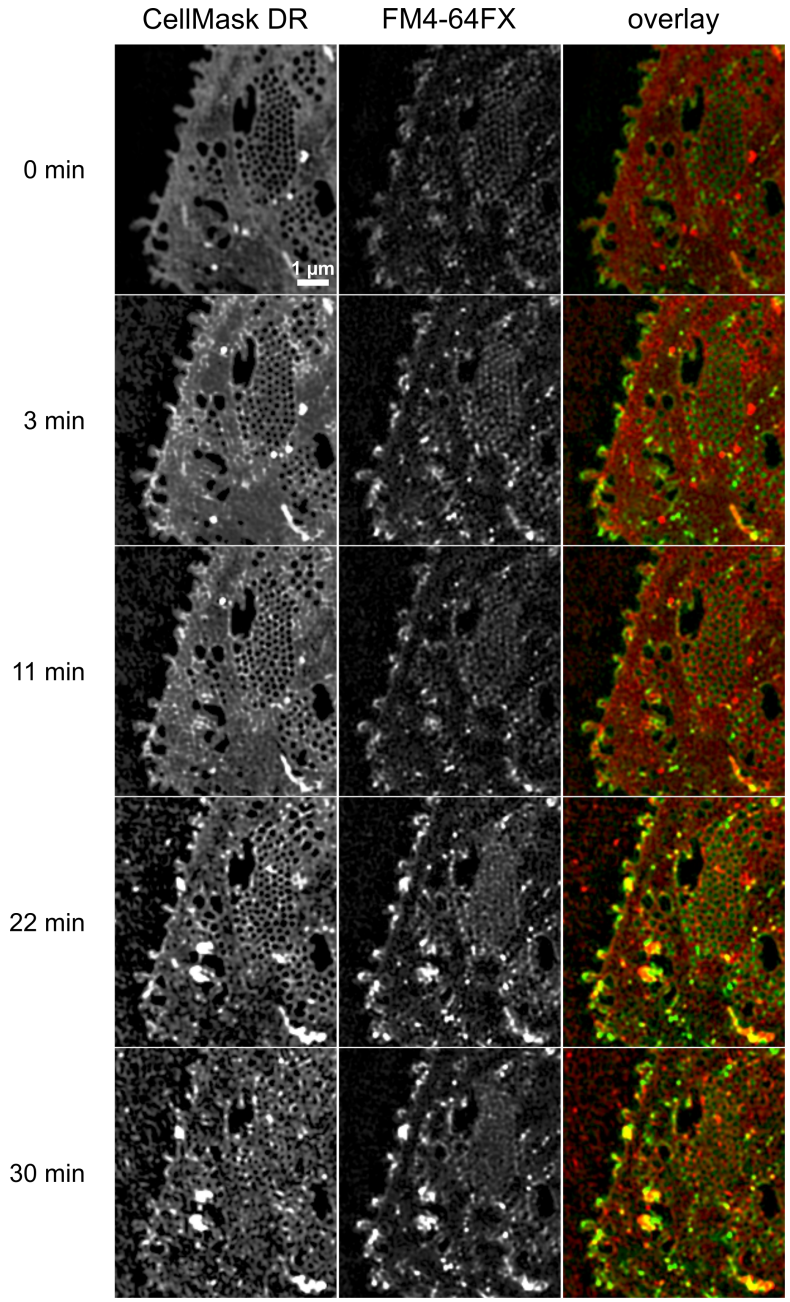

Figure 6.15.: 3D-SIM time series of a live LSEC stained with FM4-64FX (green) combined with CellMask Deep Red (red). The individual channels as well as the overlay are shown. Over the course of 30 minutes, the CellMask signal bleaches as expected, but the fenestrations still appear well defined. In contrast, the FM4-64FX stain vanishes around its initial staining of the inside of fenestrations.

FM4-64FX

Another common membrane stain is FM4-64. FM dyes are fluorescent molecules which are often used in neuroscience for staining the plasma membrane and observing endo- and exocytosis. These lipophilic styryls are known as being nontoxic to cells and non-

fluorescent in aqueous media such as buffers and culture medium. They become fluorescent after intercalating in the outer leaflet of the surface membrane. This probe has therefore great potential for super-resolution microscopy because of the low intrinsic background.

In Figure 6.15 I used a FM4-64FX probe which is a fixable red-fluorescent FM dye. The excitation is achieved with 568 nm and the emitted light is recorded at around 683 nm.

The staining was done directly on the microscope and imaged directly. According to the manufacturer, the endocytosis of this dye can occur within 10 minutes of staining. Unfortunately the fluorescence was so weak that time lapse imaging was not possible but the result was interesting anyway: Interestingly though, the dye accumulates in formations that are reminiscent of sieve plates with fenestrations. But it appears as a positive stain for fenestrations. Unfortunately, the fluorescence was so weak that time lapse 3D-SIM imaging was hardly possible. Figure 6.15 shows a 3D-SIM time lapse of a LSEC stained simultaneously with CellMask Deep Red for the plasma membrane and FM4-64FX, a fixable variant of FM4-64. Immediately after addition of the FM4-64 dye, a positive structure in the interior of the fenestrations is observed. With time, the signal vanishes and gets blurred around the sieve plate. It is possible that the dye is endocytosed locally at the fenestrations. FM4-64 is described as binding to the outer leaves of the plasma membrane. A possible explanation is that it has a significantly higher affinity for the membrane composition of the interior of fenestrations compared to other plasma membrane areas. Nevertheless, it gets rapidly endocytosed by the cell but remains at the sieve plate.

SNARF-1

Another possible approach for staining LSECs is to stain the entire cytoplasm so that the whole membrane is filled with dye from the inside leaving the fenestrations unstained. For that purpose, I tested SNARF-1. SNARF-1 is a pH indicator that is found in the cytoplasm and undergoes an emission peak shift from 580 nm to 640 nm according to a changing pH after excitation with 488 nm. The SNARF dye is used in this application is in the form of a carboxylic acid, acetate, succinimidyl ester. Living cells can be loaded with SNARF-1 and it is often used for flow cytometry, but its use in super-resolution imaging has yet to be described. As we are generally not expecting a great pH-change, we used it for staining the cytoplasm in LSECs. The result of a human LSEC stained with SNARF-1 and DAPI is seen in Figure 6.16.

The image shows part of a hLSEC with the nucleus stained in blue and the cytoplasm stained in green. Unfortunately, the background appears to be very high indicating high unspecific binding while the cytoplasm is very weakly stained. The dye seems to cluster and is not evenly distributed inside the cell. The recognition of fenestrations or any other membrane structures was not possible, thus this stain is not suited to the needs of LSECs studies. Further adaptions to the staining protocol might improve the usefulness of the SNARF-1 in the future.

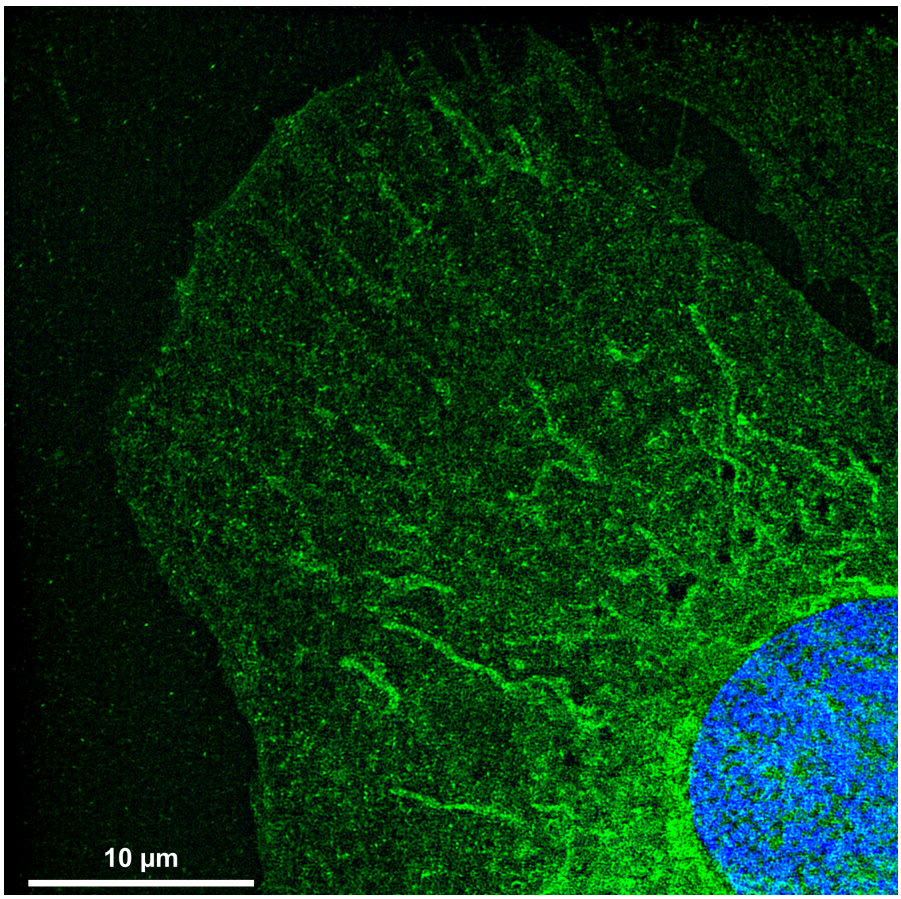

Figure 6.16.: Fixed human LSECs stained with SNARF-1 and DAPI imaged by 3D-SIM. Section of a hLSEC with a nucleus staining (DAPI, blue) and an apparently inhomogeneous cytoplasm staining (SNARF-1 green) shown as a maximum intensity projection of a 1 µm thick z stack.

DPPE

We finally used an ATTO647N fluorescently labeled phosphoglycerolipid called DPPE (1,2-dipalmitoyl-sn-glycero-3- phosphoethanolamine). Mixed with the cell culture media, this lipid incorporates into the plasma membrane of cells [90]. Unfortunately I observed a rapid deterioration of the signal around the nucleus region with 3D-SIM on ATTO647N-DPPE labeled live LSECs. There, the signal is orders stronger than in the desired fenestration areas that remain less stained. The dye seemed to bleach over time, but most importantly the fenestrations appeared to widen before the low intensities began to rendered the SIM reconstruction difficult (Figure 6.17).

In conclusion, I tested a multitude of fluorescent dyes meant for membrane staining. These have been mostly previously described in the literature and by their manufacturers as very well suited for fixed conventional low resolution microscopy applications. For super-resolution of LSECs specifically, WGA, FM4-64FX and DPPE failed to resolve fenestrations in even fixed samples. While capable of staining relatively well fixed samples, most develop obvious phototoxic effects on the cells in live imaging measurements.

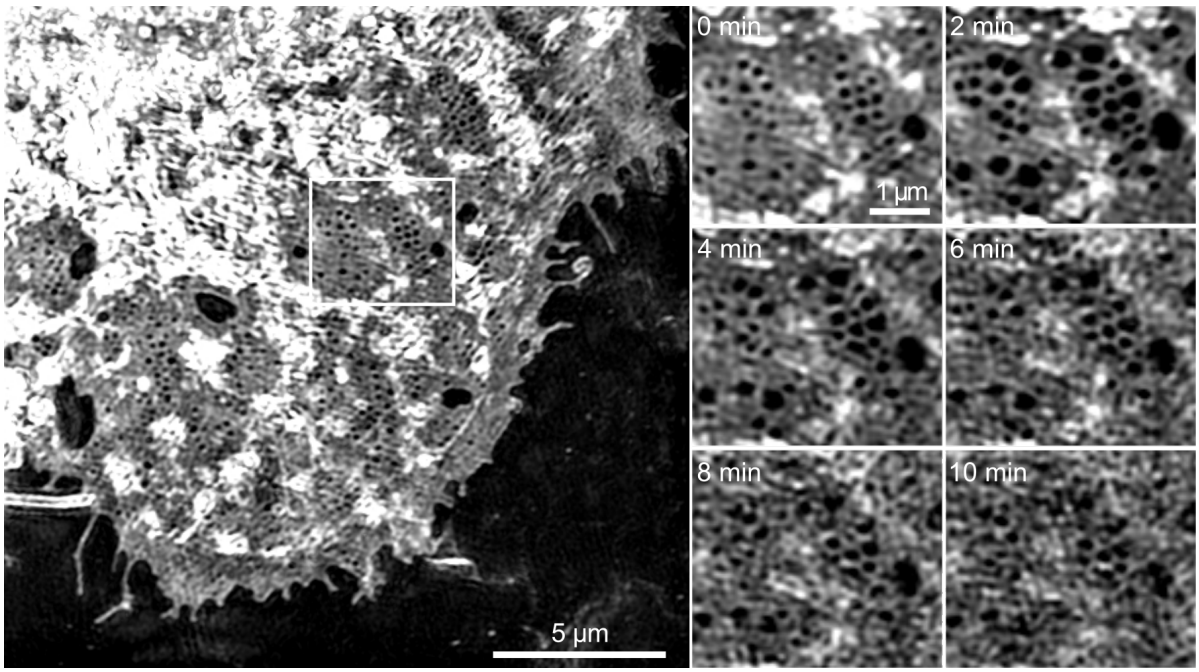

Figure 6.17.: 3D-SIM time lapse of LSEC labeled with the phosphoglycerolipid ATTO647N-DPPE. The left panel shows an LSEC at time 0, the panel on the right represents the ROI in the left over time. The images represent a maximum intensity projection of 7 z slices with 125 nm distance. A 7 image stack was recorded every 30 seconds. The fenestrations increase significantly in size after a few minutes, while the stain bleaches and reconstructions become difficult within 10 minutes. To achieve reasonable contrast for imaging in the depicted ROI, the overall illumination intensity was set so high that the camera saturation courses SIM reconstruction artifacts in other parts of the image, especially near the nucleus.

Very impressive are the rapid dye and light dose dependent effects of CellMask leading to membrane stiffness followed by blebbing. Finally, the most promising dye for further studies turn out to be Vybrant based DiO, DiD or DiI. Their only major drawback for now is the rapid photo-bleaching limiting the length of imaging recordings.

7. Fenestration dynamics and structural changes following drug treatment of living LSECs

Super-resolution imaging of live LSECs is possible by employing carbocyanine dyes (e.g. DiO and DiD, see chapter 6). Using these dyes I managed to obtain the first live LSEC images, which enabled me to determine and analyze fenestration formation and dynamics. With a suitable dye and a robust staining protocol in place, further studies become possible. Different treatments of live LSECs are tested, such as the actin disruptor Swinholide A. Live imaging of the actin and the membrane reveal the dramatic effects of this toxin. In addition preliminary experiments on ethanol and paracetamol poisoning are analyzed by 3D-SIM.

7.1. Fenestration dynamics of living LSECs

As of now, the dynamics of fenestrations in living LSECs are currently completely unknown due to their sub-diffraction size. Below the diffraction limit they are not able to be seen with conventional fluorescence microscopy techniques which would allow for fast live cell imaging. The analysis by electron microscopy techniques - which easily provides the required resolution - allows only the observation of dead (fixed) biological materials which makes live cell imaging impossible.

Previous work of Cogger et al. showed resolving of fenestrations of LSECs in light microscopy for the first time [11]. Due to the slow setup, live cell imaging was not possible at that time. It is unknown how fast fenestrations form and close or if they can move within the membrane.

The best results of membrane stains that affect live cells the least obtained with carbocyanine dyes e.g. DiO. In Figure 7.1 a living LSEC stained with Vybrant DiO is pictured as a 3D-SIM z-projection. The overview shows the cell at the beginning of the time lapse image acquisition. Images are acquired every 30 s showing a ROI with one sieve plate in the three rows below. The images are bleach-corrected via an exponential bleach correction fit, as DiO revealed photo-bleaching (see chapter 6.2.3).

At 0 s there are a couple of fenestrations marked by a yellow arrow which are translating and rotating simultaneously in the next 30 s to a slightly different position (marked again by a arrow) while the neighboring fenestrations remained nearly still. This shows that the dynamics of fenestrations inside the sieve plate are occurring in a time range below 30 s. While the other fenestrations kept their position, two of them seem con-

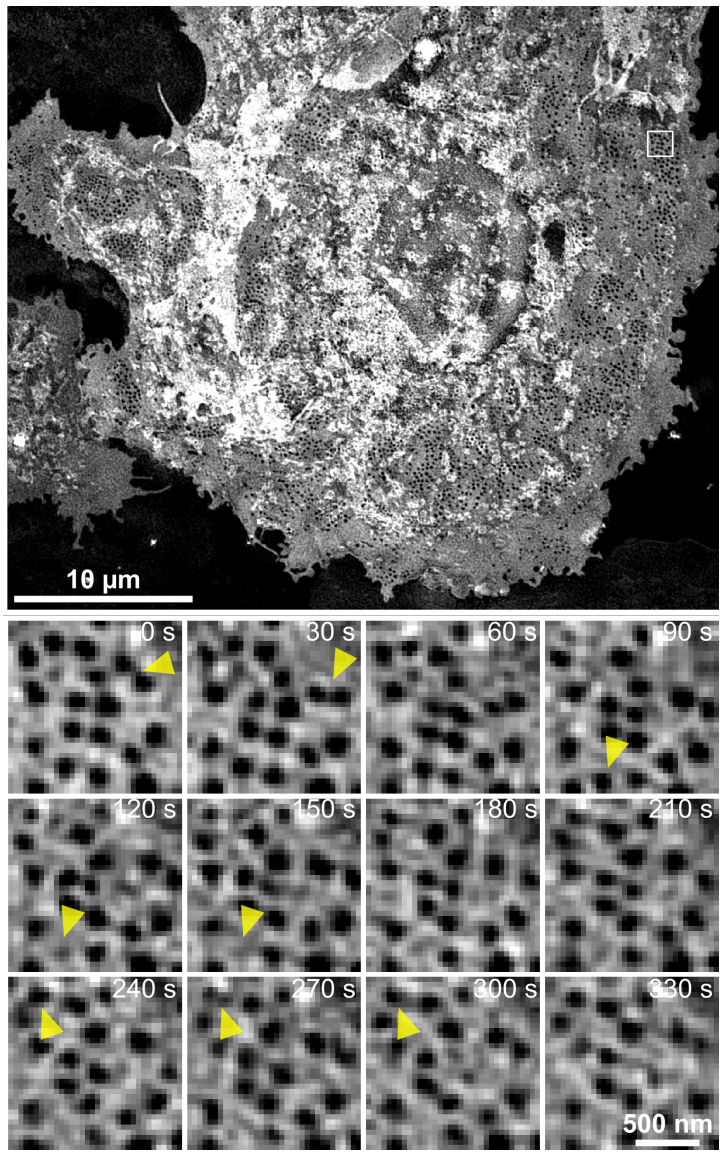

Figure 7.1.: 3D-SIM of a living LSEC stained with Vybrant DiO: Overview of the whole cell at the starting point of the time lapse in the uppermost image. Lower three rows show the time lapse from 0 s to 330 s. The yellow arrows indicate prominent points of changes (moving, closing, dividing and fusing of fenestrations).

nected and moved together as a pair. During the 90 s to 150 s time points, a fenestration is observed to be closing. The fenestration is fully open at 90 s (yellow arrow head) is vanishing at 120 s and entirely disappears at 150 s. The total closing process took less than 60 s at room temperature. The fenestration marked at 240 s, divides into two fenestrations at 270 s that fuse together to a single one at 300 s.

These results show that sieve plates are not fixed structures in the membrane. They constantly undergo rapid changes. The experimental conditions differ from the in situ situation of a living rat. The temperature of the described experiments is about 23°C

instead of the physiological 37°C. Evidently, the extraction, isolation and plating of a near pure fraction of LSECs, does not guarantee the biological relevance of such a cell culture model. Finally, the laser illumination as well as the staining procedure could dramatically affect the function of the cells in terms of morphology and dynamics

Despite these possible experimental drawbacks, these are the first live cell observations of LSECs and their fenestration dynamics. These experiments lay the foundation for further studies with nanoscopy as a readout technique on the mechanisms of fenestration dynamics in LSECs as well as responses to environmental changes.

7.2. Effect of different substances on living rat LSECs

The dynamics of fenestrations in LSECs are influenced by many effects. At first it has to be clarified that the dye can have a huge effect on the membrane dynamics such as demonstrated in chapter 6. The CellMask dyes, for example, lead to a stiffening of the membrane coupled with an increased phototoxicity. This then leads to an increase in the number of fenestrations, blebbing and ultimately cell death.

The dye which shows the least influence on apparent cell morphology and dynamics is Vybrant DiO. The treatment experiments on living LSECs are either done with Vybrant DiO or SIR actin [91] labeling.

One often used treatment for LSECs and analyzed by electron microscopy is the application of Swinholide A [76]. Swinholide A (sigma, S9810) is an actin disruptor extracted from the sponge *Theonella swinhoei*. It severs the F-actin network and sequesters actin dimers thus leading to actin depolymerizing effects.

Braet et al. [76] showed that with Swinholide A treatment the diameters of fenestrations decrease while the number of fenestrations increases. Figure 7.2 shows an entire LSEC after 70 minutes of Swinholide A treatment. The living cells were stained with 5 µM Vybrant DiO and treated directly on the microscope with 25 nM Swinholide A. Here, fenestrations vanish but it is unknown if they are shrunken below the SIM resolution limit or if they actually disappeared. Conspicuous is a contraction of the outer regions to the cell center that can be seen in Figure 7.2.

The time point labeled with '0 min' corresponds to the starting point of the experiment 10 minutes after addition of Swinholide A. Below the overviews in Figure 7.2, a time series of the ROI is pictured. The time-lapse between the images is 5 minutes and shows the changes of a sieve plate due to the Swinholide A treatment. At 0 minutes the sieve plate with a size of about 8 μm^2 contains about 50 fenestrations. Within the sieve plate is a membrane knob surrounded by fenestrations (yellow arrow) that increases over time. While the fenestrations decrease in size and disappear over time, I could not observe an increase of the total number of fenestrations.

I also observed the effects of Swinholide A on the actin cytoskeleton of living LSECs. Figure 7.3 shows a LSEC stained with the actin binding fluorescent compound SIR-Actin during a Swinholide A treatment. As in Figure 7.2 the cell was imaged with 3D-SIM every 5 min for up to 2 hours. Within 20 min of Swinholide A treatment, drastic changes in the actin cytoskeleton are observed. Fine filaments disappear while actin concentrates

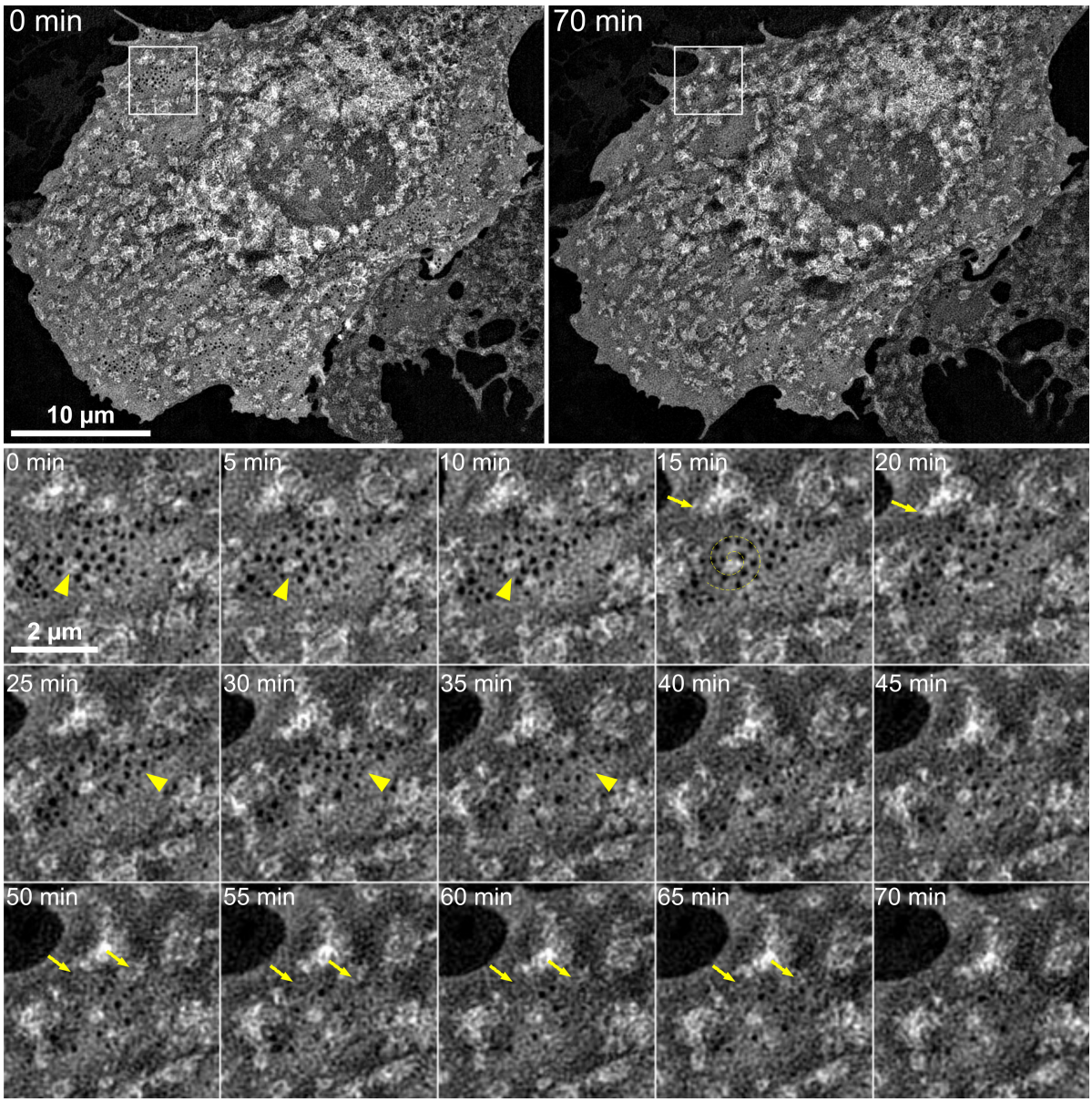

Figure 7.2.: 3D-SIM imaging of plasma membrane labeled LSEC treated with Swinholide A. The cells have been stained with Vybrant DiO. The top panels show a LSEC at the beginning of the imaging on the left (0 min) and 70 minutes later at the right. A stack of 7 slices was recorded every 5 minutes. The drawn region of interest is shown on the bottom half of the figure with an image every 5 min. Between time point 0 and 10 min the yellow arrow indicates the appearance of a membrane knob. The other arrows point to disappearing fenestrations. The time point '0 min', at the start of the image acquisition process, corresponds to 10 minutes after addition of Swinholide A.

into asterisk like formations (Figure 7.3, yellow arrows).

Given the close correlation of actin filament structures with sieve plates and their fenestrations (see also chapter 5), the disappearance of fenestrations as actin filaments depolymerize should not come as a surprise.

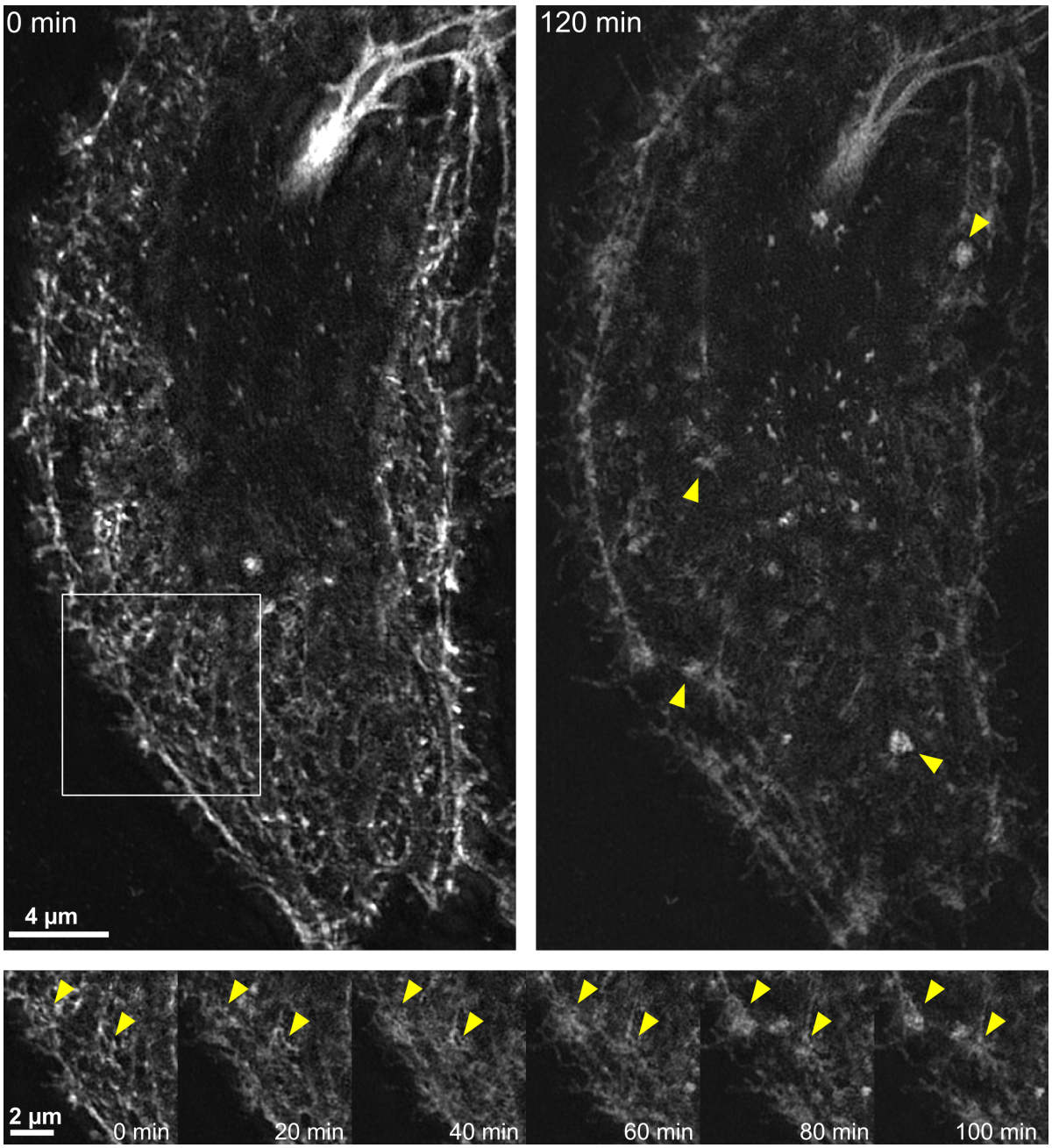

Figure 7.3.: 3D-SIM imaging of actin filaments labeled LSEC treated with Swinholide A. The cells have been stained with the actin binding dye SIR-Actin. The top panels show a LSEC at the beginning of the imaging on the left (0 min) and 120 minutes later at the right. A stack of 7 slices was recorded every 5 minutes. The drawn region of interest is shown on the bottom half of the figure with an image every 20 minutes up to 100 minutes. The yellow arrows point to actin filaments bundling into aster formations. The time point '0 min', at the start of the image acquisition process, corresponds to 10 minutes after addition of Swinholide A.

7.3. Ethanol and paracetamol treatment

It is known that high doses of paracetamol causes liver damage especially in the hepatocytes where the paracetamol is metabolized [92]. The effect on liver sinusoidal endothelial cells in tissue is a gap formation between the LSECs causing a leakage between space of Disse and blood [93].

To evaluate the effect of paracetamol treatment on the fenestrations including the actin skeleton and membrane, as well as a combination with ethanol poisoning, the LSECs were treated in different ways with very high concentrations of both substances. At first the effects of high doses of either ethanol (0.2%) or paracetamol (2000 mg/kg) on LSECs alone were tested[1]. The results are shown in Figure 7.4.

The first row illustrates untreated LSECs as a control in which the medium was exchanged under the same conditions as for the ethanol and paracetamol treated cells. The ethanol treatment of LSECs for 30 minutes at a very high concentration (corresponding to the consumption of two bottles of wine) showed very little to no apparent changes in the number and sizes of fenestrations as well as actin cytoskeleton. On the other hand 30 minutes of incubation with Paracetamol (APAP) led to a visible rearrangement of the actin into asterisk clusters. Fenestrations appear smaller and sieve plate formation vanished. Based on earlier publications paracetamol poisoning causing severe health issues leading up to death of the affected person are due to the combination of alcohol consumption followed by paracetamol uptake. I tested the effect of ethanol treatment followed by APAP as well as the reverse on LSECs in culture. Figure 7.5 shows SIR-Actin labeled cells treated for 30 minutes with 0.2% ethanol followed by a toxic concentration of APAP (2000 mg/kg) for 90 minutes on the top panel. The lower panel depicts cells incubated first with APAP for 30 minutes and then for 90 minutes with ethanol. In both cases, the actin filament mesh characteristic of fenestrations and sieve plates appears to be disrupted. In the case of APAP followed by ethanol, the sieve plates were not defined anymore, leaving a dense actin cytoskeleton mesh. Most interestingly, the cells treated first with ethanol and then with APAP showed a more pronounced rearrangement of the filaments into asterisk reminiscent of the APAP alone treatment. Nevertheless, in both conditions (ethanol and then APAP or APAP and then ethanol), the fenestrations vanished and could not be resolved by 3D-SIM anymore after fixation and CellMask labeling. Figure 7.6 shows the different treatment conditions with a CellMask Orange membrane staining.

These preliminary studies on live fenestrations dynamics and changes following drug treatment have never been described in the literature. It validates super-resolution 3D-SIM applied to living LSECs as a valid assay to answer fundamental biomedical questions in the field that remain yet unanswered. In addition, the molecular mechanisms involved in fenestrations formation and disappearance are undefined. Further studies on LSECs with 3D-SIM as an experimental assay should help tremendously in solving these questions.

[1] It has to be mentioned that the here performed experiments are done with very high and toxic concentrations of ethanol and APAP on isolated LSECs. Other experiments in vivo even show a preventive effect of alcohol on paracetamol-induced hepatoxicity [94].

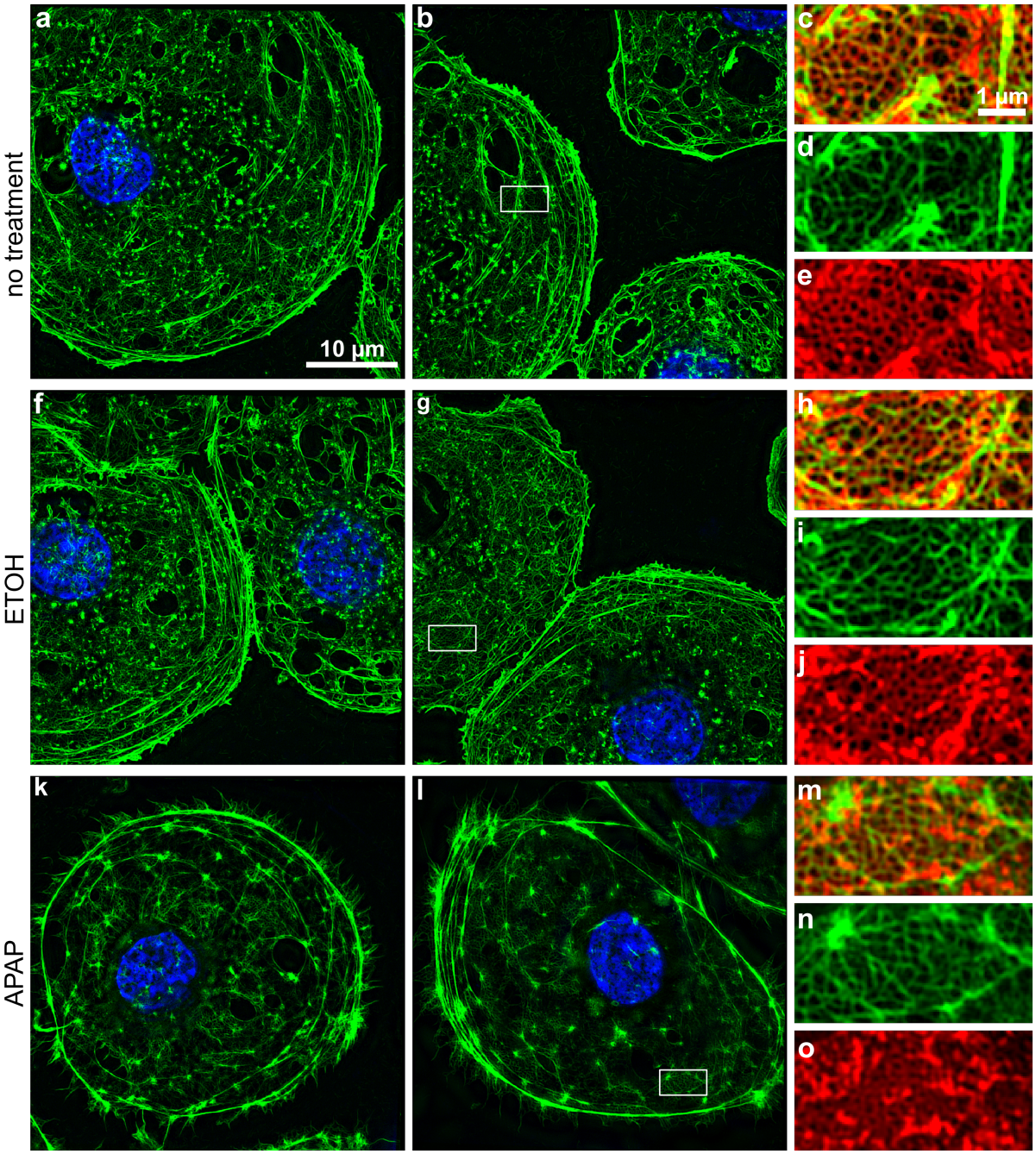

Figure 7.4.: 3D-SIM of LSECs treated with either ethanol 0.2% or paracetamol (APAP, 2000 mg/kg) for 120 min. LSECs were fixed after treatment and labeled with CellMask Orange (red) and Phalloidin Alexa 488 (green) as well as DAPI (blue). The top panel (a - e) represents untreated control cells, middle ethanol (f - j) and bottom APAP (k - o) treated cells. DAPI and actin stain are only shown in the uncropped cells. Panels (c - e), (h - j) and (m - o) are overlay, actin and membrane stains of the corresponding ROI in (b), (g) and (l).

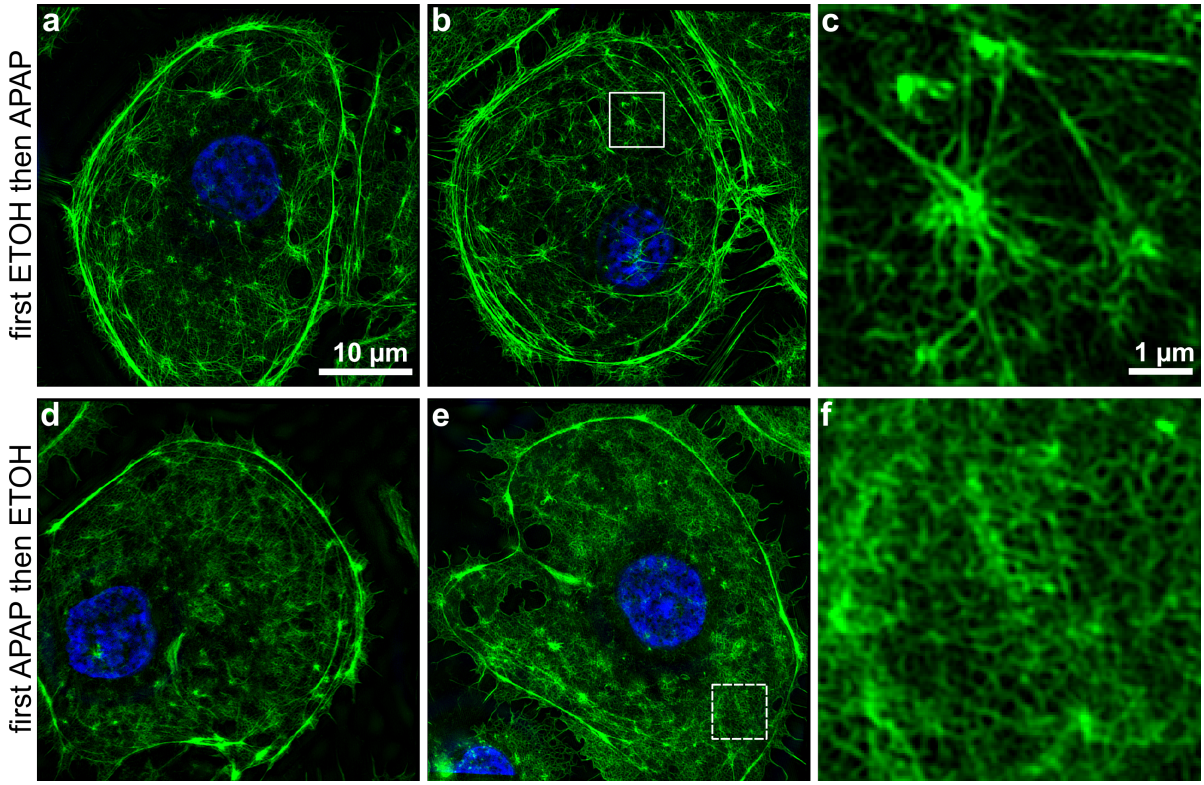

Figure 7.5.: 3D-SIM of actin stained LSECs which were pretreated for 30 min with ethanol following an APAP treatment for up to 90 min (a - c) or first 30 min APAP (2000 mg/kg) followed by ethanol for 90min (c - f). For each condition two different cells are shown (a, b and d, e). c and f are the ROI drawn in b and e respectively. The actin stain is represented in green while DAPI in blue.

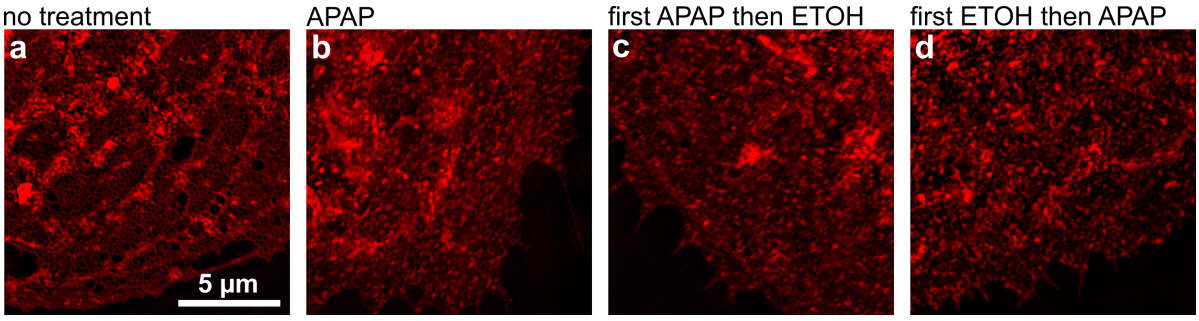

Figure 7.6.: LSECs with different treatments of APAP and ethanol were stained after fixation with CellMask Orange, and imaged in a 3D-SIM (B.3). (a) is the control which is not treated. The other panels are (c) treated with 120 min APAP, (c) pretreated 30 min with APAP, then another 90 min with APAP and ethanol and (d) pretreated 30 min with ethanol, then another 90 min with APAP and ethanol.

8. Instant SIM and its extension to two-photon microscopy

Super-resolution fluorescence microscopy places high demands on image acquisition speed to provide sub-diffractive sample information as these techniques move spatial information into the temporal domain. To observe fast dynamics, e.g. processes in living cells that occur on second and sub-second time scales, improvements to the speed of the high- and super-resolution methods become necessary. The instant SIM (iSIM) is an analog (i.e., purely optical) multi-focal implementation of the ISM approach [45] and enables 145 nm lateral and 350 nm axial resolution at up to 100 Hz [17]. This technique could be applied for live LSEC imaging providing that the resolution is high enough to enable the observation of fenestration which is tested in this chapter.

8.1. LSECs imaged by instant SIM

The setup and the working principle of the iSIM is explained in chapter 2.2.2. Due to the advantages of the high frame rates with $\sqrt{2}$ improved spatial resolution this microscope is of great interest in observing the dynamics of biological systems. The instrument not only surpasses a classical confocal microscope in terms of speed, but also implements a re-scanning like effect that improves the resolution [46] (see chapter 2.3). During the course of my work I visited the National Institutes of Health (NIH) and used the original iSIM in Hari Shroffs group to assess, if this technique is suitable for resolving fenestrations in LSECs.

The analog (optical) image-processing operations are shown in Figure 8.1. To follow the optical processes and align the setup, a fluorescent slide is produced by applying a yellow HI LITER pen on a cover glass. Compared to autofluorescent adjustment slides (Chroma) the fluorescent layer is very thin. The cover glass is mounted with prolong gold and sealed with nailpolish. Figure 8.1 (a) shows the spots generated by the first microlens array (f=1.86), which is placed in the excitation path. The spots are very bright but there is still a lot of background. In Figure 8.1 (b) the matching pinhole array is added in the emission path to filter the out-of-focus light. The result is a pattern with defined spots. The last important step is to insert the second microlens array (c), which is aligned to the spots in the emission path and effects the 0.5 scaling of each spot. To gain the high-resolution image, the foci have to be scanned over the sample and camera, which can be seen in Figure 8.1 (d). Due to a precisely aligned rotation axis with respect to the array orientation, the spots scan the whole sample

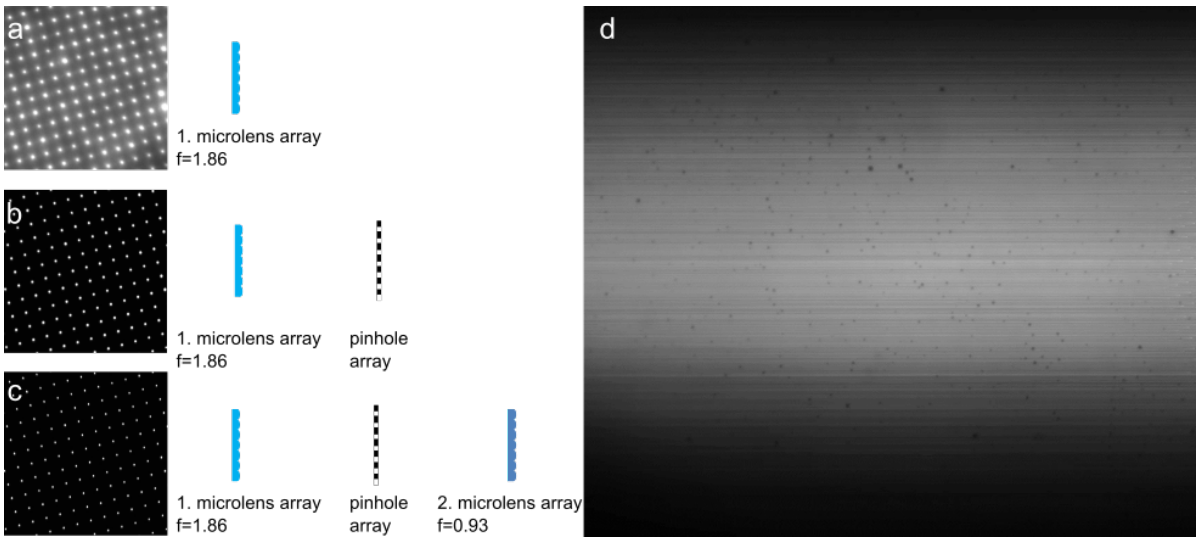

Figure 8.1.: Single steps of the optical focus compression measured with instantSIM of a HI LITER slide excited with 488 nm (left). By moving the mirror galvanometer (galvo-mirror in Figure 2.10) the spots scan the whole area in 1 frame. Here 2 sweeps within 20 ms are done. (d) is an area of 105 µm x 90 µm

with galvo-mirror movement along one axis only. A single sweep takes 10 ms. Typically several sweeps are performed to gain a better signal, as within a constant sweep speed, the number of sweeps directly yield the exposure time. In this homogenous fluorescent sample the stripes of the scanning process can still be seen. Additionally the brightness is inhomogeneous over the 105 x 90 µm^2 field of view. This is due to the rotation of the squared spot pattern. The top and bottom areas are scanned by fewer points than the middle area when swiping the pattern horizontally.

I analyzed double stained LSEC samples to test the feasibility of iSIM for resolving fenestrations. The available laser wavelengths at this setup are 488 nm and 561 nm. The important structures of LSECs are the membrane and actin skeleton and therefore these are stained by CellMask Orange and Phalloidin Alexa Fluor 488 respectively. The results are seen in Figure 8.2.

The first and the second row in Figure 8.2 (a) show the effect of the galvo-mirror sweeps does during one frame. For a strong stain, such as the membrane dye CellMask Orange, two sweeps result in a well-defined image while for the stained actin more sweeps are needed to improve the noisy image from row one. Row two gives the result for 50 sweeps during one acquisition frame. The contrast for actin is increased while the membrane images suffer from overexposure at the nuclear region. The above mentioned stripe pattern artifact in Figure 8.1 can also be seen here. The effect becomes more visible here, as the membrane is a rather planar, homogenous structure.

In (b) the final deconvolution step of the overlay from 8.2 (a) gives the highest obtainable resolution for this microscope. In the enlarged ROI several sieve plates including their fenestrations are resolved. This result is a strong improvement compared to the deconvolved CLSM images in Figure 3.5. The last two images show a comparison of the

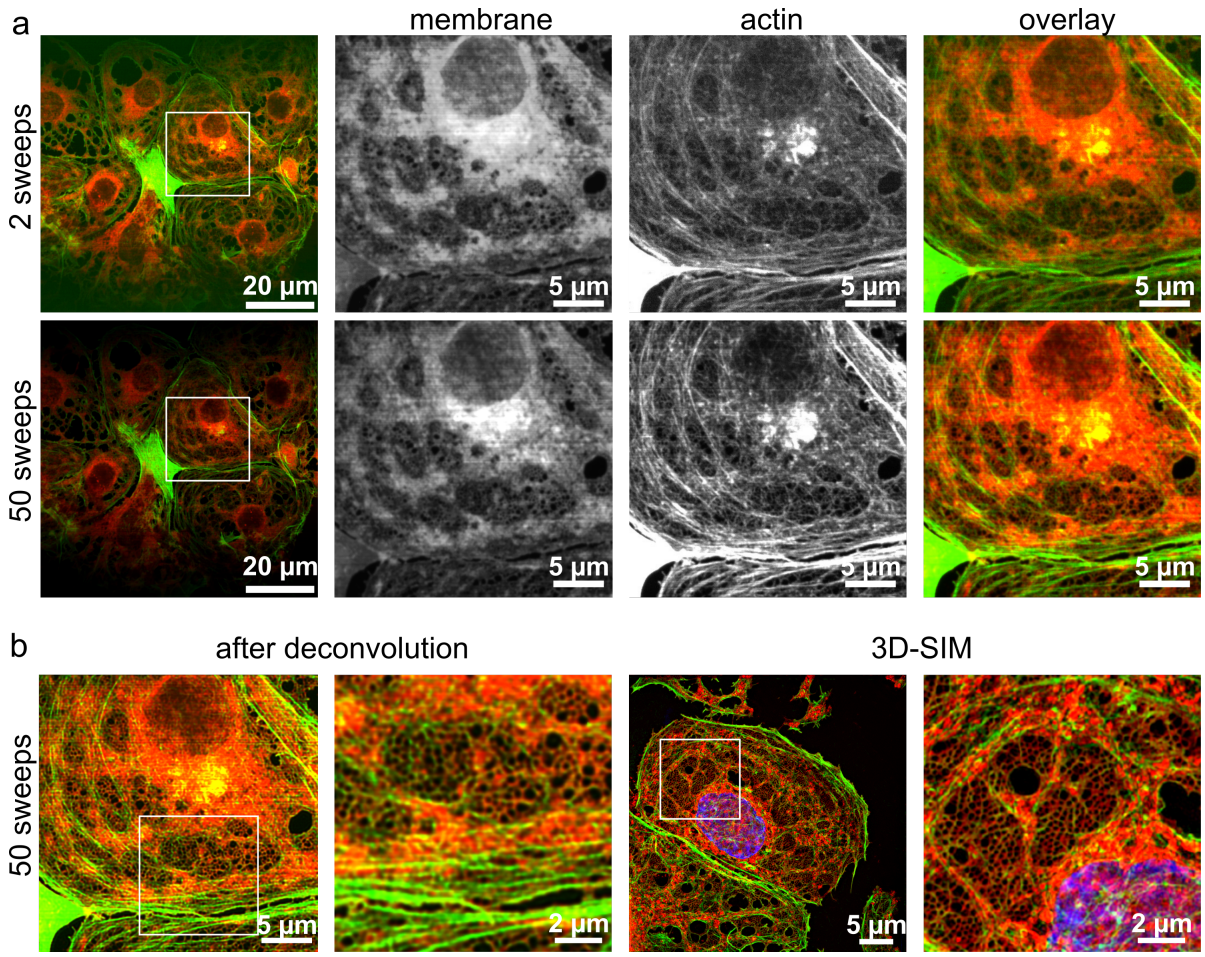

Figure 8.2.: Double stained LSECs are imaged by the instantSIM. The first row in (a) uses 2 sweeps per acquisition frame while in the second row 50 sweeps per frame are used. The bright membrane stain gives enough contrast for 2 sweeps while the less stained actin filaments need 50 sweeps. (b) The final resolution improvement is reached after a deconvolution step that results in almost similar resolution as the 3D-SIM measurements of the same sample. All images are z-projections of about 1 µm.

same sample (but different cells) imaged by a 3D-SIM. As expected the resolution in 3D-SIM is better. The fenestrations and actin filaments are well-defined and no striped pattern artifact is overlaying the data. However, the acquisition time is much fewer in the iSIM data.

Outlook: construction of two-photon instant SIM

The ideal approach for live cell imaging in thicker samples, such as tissue, is to use this approach with high resolution and high frame rates in combination with two-photon fluorescence excitation. The non-linear two-photon effect allows deeper penetration depths of up to 1000 µm with a better lateral resolution and without using pinholes. The phototoxicity and bleaching effects are also less due to the long wavelength. As the two-photon

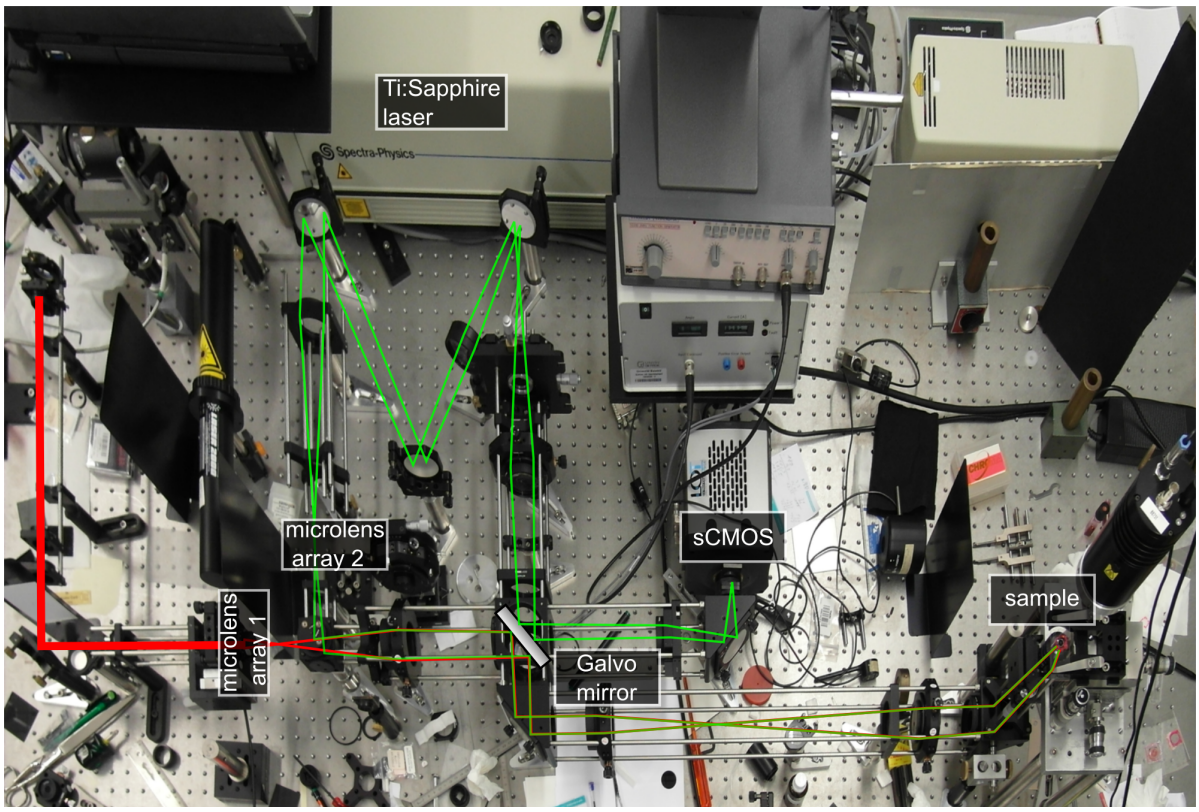

Figure 8.3.: First attempt of a two-photon iSIM. The setup is similar to the original setup. For the two-photon excitation a pulsed Ti:sapphire laser is used. The second microlens array is set to the position of the pinhole in the original setup.

process (see chapter 2.2.3) requires high photon densities and is implemented with high-power, short-pulse laser systems, there are many obstacles to a coherent, wide-field two-photon SIM implementation. A multi-spot confocal approach, such as the iSIM is much easier to realize for a two-photon microscope.

The first attempt to build this setup after the model by York et al. is seen in Figure 8.3. The lasers are replaced by a pulsed Ti:sapphire laser (Tsunami, Spectra-Physics). For the resulting two-photon excitation a pinhole in the emission path is not necessary and therefore the second pinhole array can be placed at its position.

The first results gained with a dried Rhodamin B sample are seen in Figure 8.4 (a) and (d). (a) is the scanned image without the second concentrating microlens array while in (d) the sample is scanned by the compressed spots. Even with Rhodamin B as a strong two-photon dye and long acquisition times of several seconds, the signal is very weak. The two-photon process is non-linear and scales with I^2. Therefore every loss of energy has to be avoided. Splitting the beam into small foci is the important factor of this method. However, it is decreasing the two-photon excitation probability. A second factor is the choice of the focal length of the microlens array. The influence of this effect can be seen in Figure 8.4 (b, c, e, f). (b) is the image of the microlens array from the original instantSIM with a short focal length. This results in a broad

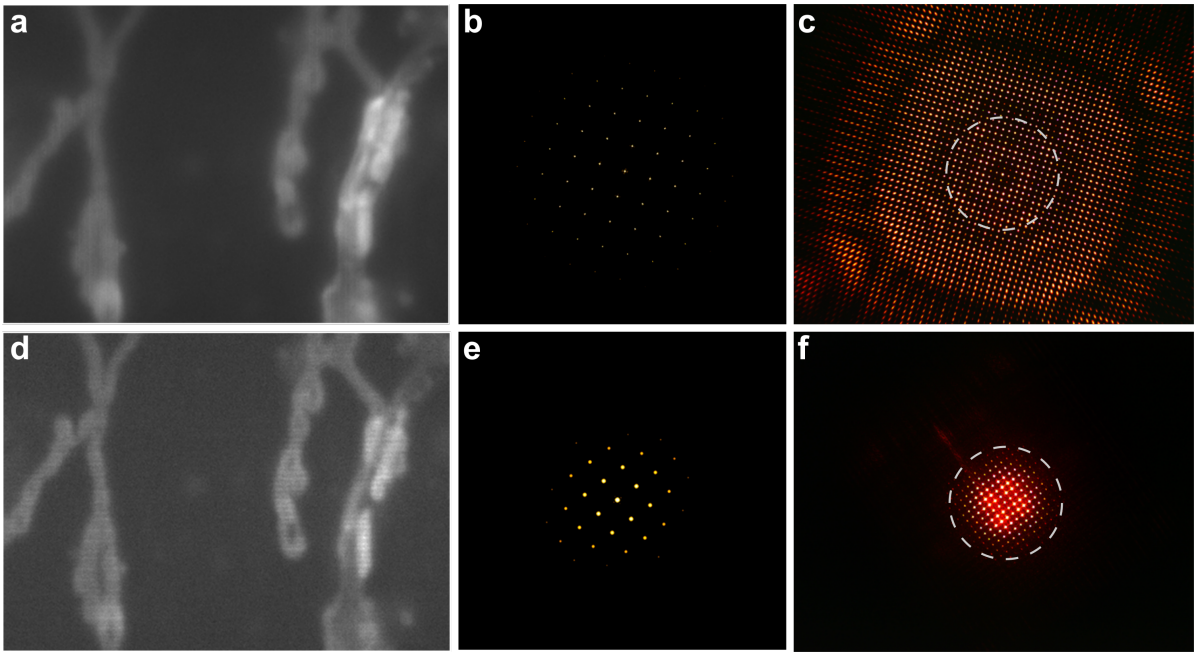

Figure 8.4.: First results of the two-photon iSIM with dried Rhodamin B show a slight improvement in contrast (a, d). To avoid the photon loss due to a short focal length of the microlens array and a resulting cut-off effect in the back focal plane different microlens arrays are tested. (b, e) shows the spots generated by the first array in real space, (c, f) are the corresponding Fourier space images that appear at the back focal plane.

Fourier distribution in the back focal plane of the objective, which is cut off due to the limited size (circle in Figure 8.4 (c)). By increasing the focal length this cut-off effect and therefore the intensity loss can be minimized (Figure 8.4 (f)).

To test the two-photon iSIM on LSECs or liver sections, further improvements have to be implemented. This work is in progress, but beyond the scope of this thesis.

9. Further super-resolution projects

During the course of this thesis, I worked and collaborated on projects not related to LSECs. I applied multimodal super-resolution techniques (introduced in chapter 5) for the complementary analysis of lipid nanodomains in neural crest-derived stem cells (NCSCs) [18]. These nanodomains are believed to be crucially involved in the regulation of signal transduction and cannot be directly imaged using conventional light microscopy due to their small size (diameter 10-200 nm). The super-resolved fluorescence images reveal the distribution of nanodomains in NCSCs by 3D-SIM and SMLM.

The second project describes the open-source reconstruction software fairSIM which we developed in our lab. FairSIM is a ready-to-use reconstruction software distributed as a plugin for ImageJ/Fiji. The software was tested on different data sets gained by 3D-SIM using single slice reconstruction for 2D analysis. The quality of the reconstruction is as good as the commercial software, however, not bound to a specific microscope and freely available.

The last project is the investigation of an alternative for fluorophores that can be used for super-resolution techniques. The observation time and the spatial resolution in fluorescence microscopy is often limited by photo-bleaching of fluorescent probes. Bleaching is fatal especially in 3D-SIM and leads to artifacts in the reconstructions. Here I demonstrate that Raman scattering nanoparticles also provide valuable contrast for optical nanoscopy. The nanotags, i.e. gold and silver nanoparticles capable of surface-enhanced Raman scattering (SERS), can be imaged with a spatial resolution beyond the diffraction limit in four dimensions alongside and with similar excitation power as fluorescent probes.

9.1. Visualizing lipid nanodomains in mammalian cells

I used my newly developed approach, which combines 3D-SIM and *d*STORM at the same setup to investigate different biological questions (see also chapter 5). 2015 I participated with Schürmann et al. [18] in a project to analyze lipid nanodomains in neural crest-derived stem cells (NCSCs) with several super-resolution microscopy techniques (Figure 9.2), such as HIM, AFM and correlative 3D-SIM/*d*STORM.

The liquid mosaic model as it was mentioned before (Figure 6.1) needs to be modified. In the last 40 years detergent-resistant membrane nanodomains called 'lipid rafts' with sizes of 10 to 200 nm were postulated [95, 96]. They consist of sphingolipids with a higher number of saturated bonds compared to other membrane lipids [97]. Due to the small size lipid rafts cannot be resolved with conventional resolution-limited microscopy.

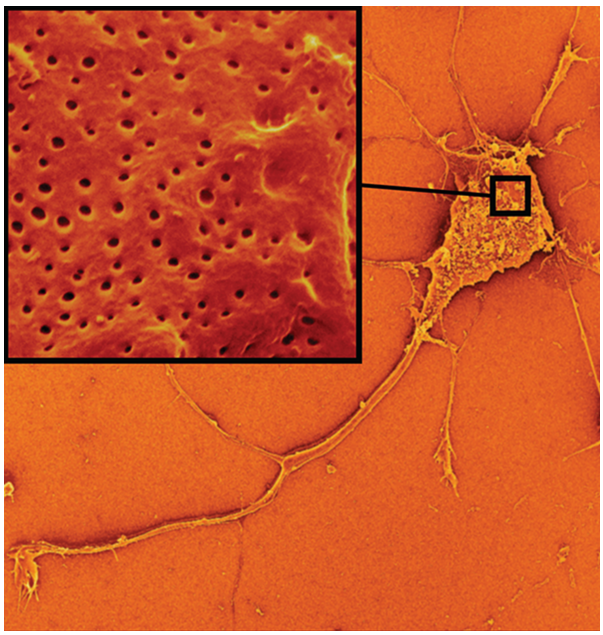

Figure 9.1.: Helium ion microscope image of a mouse neuron. The high-resolution inset reveals pit-like membrane nanodomains. Image adapted from [98]

Schürmann et al. investigated the ultrastructure of the plasma membrane with a helium ion microscope (HIM) (Figure 9.1). HIM revealed pit-like domains in the cell membrane which are thought to be a direct visualization of the membrane nanodomains (e.g. lipid rafts). The osmium tetroxide used in the cell preparation for HIM reacts with the unsaturated fatty acids of the membrane by cross-linking it. However, the saturated fatty acids of the nanodomains do not cross-link and therefore are not stabilized. They are washed out in the following preparation steps and pit-like structures remain. To further investigate this theory I used multi-modal super-resolution microscopy to investigate fixed NCSCs. The 3D-SIM image (z-projection of about 6 µm) of a whole NCSC is seen in Figure 9.2. The cell is stained with DAPI for the nucleus, Phalloidin Alexa Fluor 488 for the actin and cholera toxin fragment B (CTxB) coupled to Alexa Fluor 647 for the lipid rafts by binding to Ganglioside 1 [95]. ROIs of different positions in z and correlating *d*STORM measurements are shown on the left and right. The thickness of the region investigated by *d*STORM is about 400nm which corresponds to 3 slices from the 3D-SIM stack.

With fluorescence microscopy the osmium tetroxid and ethanol treatment can be avoided. Figure 9.3 (a) and (b) compare fixed cells stained with a DAPI and CTxB without (a) and with (b) an EtOH treatment. After washing with EtOH the raft-like nanodomains are apparently gone and could not be stained by CTxB anymore.

With a correlation of 3D-SIM and *d*STORM I could show that CTxB labels are arranged in nanodomains close to actin structures (Figure 9.3 (c) and (d)). This could confirm that besides HIM methods such as *d*STORM are able to visualize the assumed nanodomains.

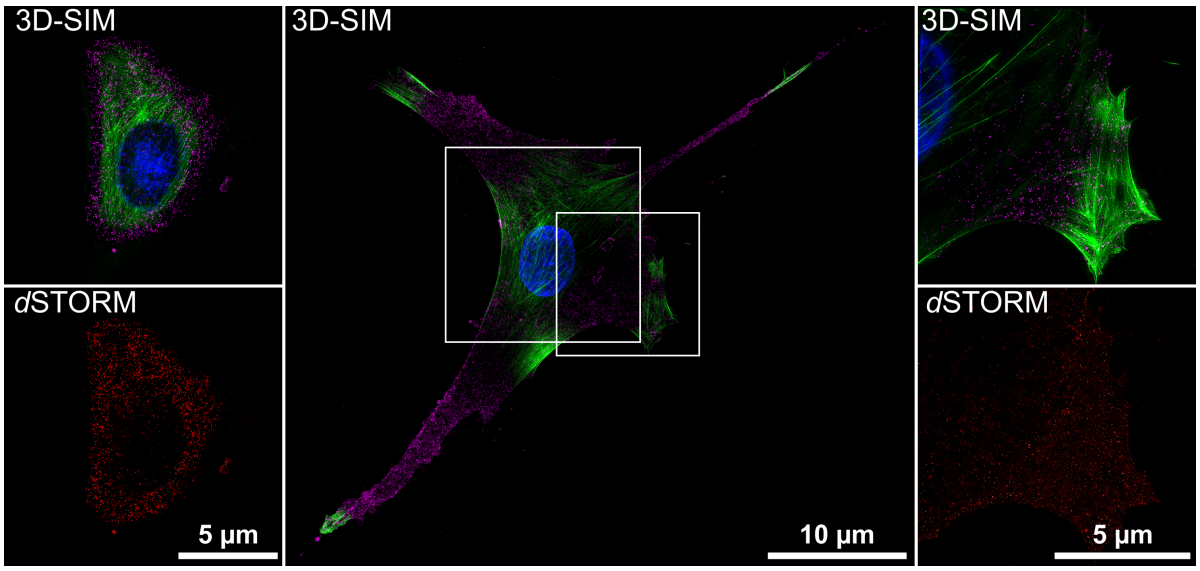

Figure 9.2.: Application of the multi-modal nanoscopy approach: The overview in the middle shows a 3D-SIM z-projection (4 µm) of a neural crest-derived stem cell (NCSC) stained with DAPI (nucleus, blue), Phalloidin Alexa Fluor 488 (actin, green) and CholeratoxinB-AlexaFluor647 (lipid rafts, magenta). On the left and right ROI are additionally imaged with 2D-*d*STORM. The left images show an area of about 3 µm distance from the coverslip with a thickness of 400 nm, the right images are in 500 nm distance from the coverslip showing areas with 400 nm thickness.

9.2. Open-source image reconstruction of super-resolution structured illumination microscopy data in ImageJ for optical nanoscopy

Since super-resolved structured illumination microscopy (SR-SIM) has become an important tool for fluorescence microscopy many research groups started developing their own setup and implementations of this technique. A successful reconstruction from the raw data obtained on these microscopes depends on the software implementation of specific SR-SIM image reconstruction algorithms (see chapter 2.4.3).

We (Müller et al. [99]) developed an open-source solution, an easy-to-use ImageJ[1]/Fiji plugin, called *fairSIM*. Before research groups who developed SIM setups had to write their own software based on the published algorithms [59]. Now fairSIM makes it easier for many researchers to focus on new developments instead of spending time on difficult reconstruction implementations. Also for research groups with commercial 3D-SIM systems fairSIM offers an independent alternative to the proprietory software delivered with the specific machine. It makes in depth analysis on every computer possible.

To date fairSIM is a 2D reconstruction software and can be used for 2D-SIM or single z-slices from 3D-SIM data. By acquiring raw data from only one focal plane the image acquisition can be much faster and less photodamage is induced. This is advantageous for live cell imaging, e.g. following fast processes inside cells, where speed and phototoxicity

[1]ImageJ is a free and widely used image analysis platform [100]

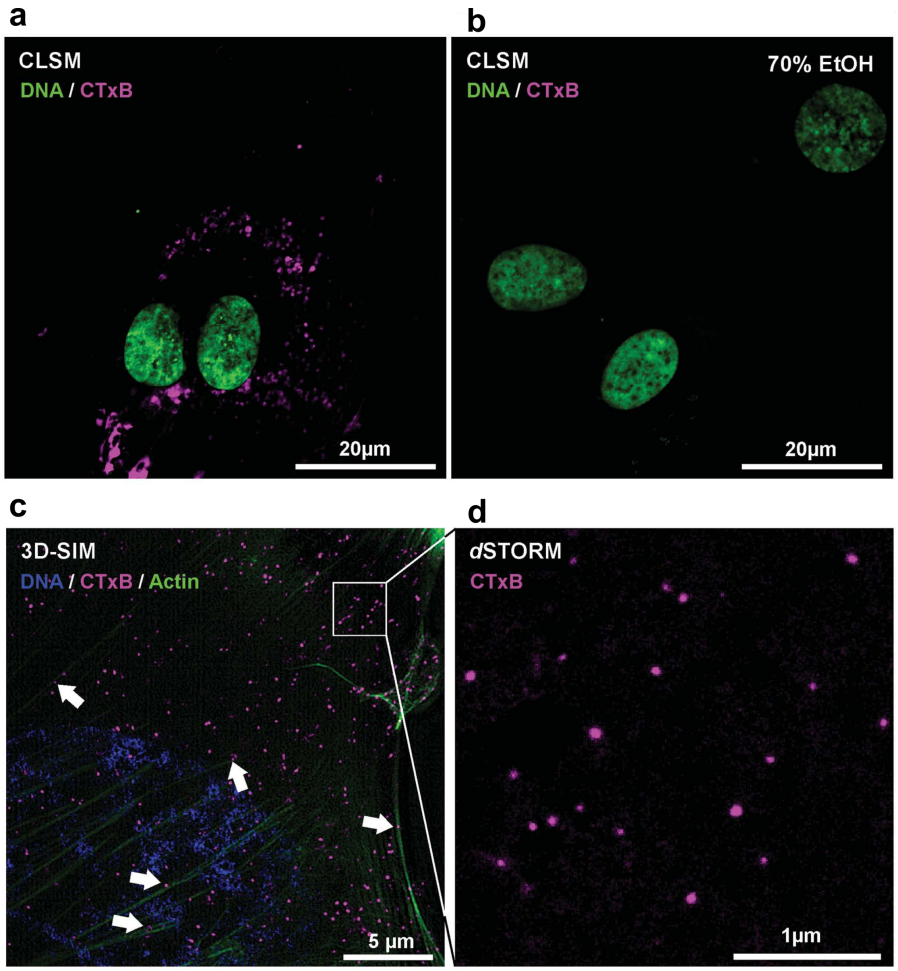

Figure 9.3.: Fixed cells labeled with CTxB (lipid rafts) without (a) and with an ethanol treatment imaged by confocal laser scanning microscopy. (b) shows no positive signal for CTxB after treatment with ethanol. In (c) 3D-SIM (z-projection) and (d) *d*STORM super-resolution images are seen. A homogenous but anisotropic distribution of CTxB labeled membrane nanodomains is found in both methods. The arrows in (c) mark the colocalization of nanodomains and actin filaments. Figure is adapted from [18]

are the critical criteria. 2D-SIM archives the same twofold lateral resolved images, however, the axial resolution is not enhanced and in thicker samples the background can lead to reconstruction artifacts in 2D-SIM reconstructions. For example, data acquired with 3D-SIM for one z-slice of a thick cell stained for actin suffer from high background, that yield reconstruction artifacts (Figure 9.4 (c)). To mitigate this effect, fairSIM provides optical sectioning through optical transfer function attenuation [101, 102]. By using the OTF attenuation the background is reduced and a good reconstruction can be generated (Figure 9.4 (d)).

The fairSIM plugin also provide in-depth analysis for advanced users (see Figure 9.5). The intermediate results of the reconstruction process and the parameter estimation are shown in frequency and spatial space. This enables to judge the quality and progress of the image reconstruction process. In addition to this it provides important feedback for

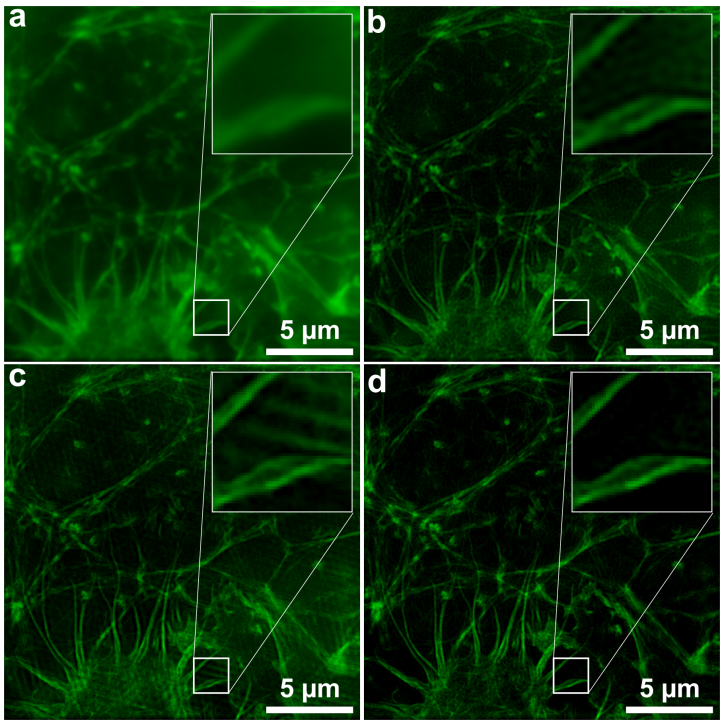

Figure 9.4.: Actin filaments in U2OS cells, labeled with Phalloidin-Atto488, measured on a DeltaVision OMX, excited at 488 nm wavelength. (a) Wide-field, (b) Wiener-filtered wide-field, (c) reconstruction using a standard 2D OTF, (d) reconstruction using the attenuated OTF (strength 0.995, FWHM 2 cycles/micron). Due to the 2D OTFs missing cone problem, background artifacts emerge when reconstructing with an unmodified OTF (c). For 3-beam data (where the bands overlap each others missing cones) and for 2-beam data (trading lateral resolution improvement for a larger overlap) the missing cones can be filled from other bands through the OTF attenuation, and the artifacts are mitigated (d). Thus, the reconstruction gains optical sectioning. Size of inset 2.0 µm. Taken from [99]

the adjustment and quality control of home-built SIM setups.

We tested the software on different samples. Figure 9.6 show two types of samples. On the left (a-f) the often used beads and on the right (g-j) LSECs as a important biological test sample can be seen. the bead surface seen in Figure 9.6 uses 200 nm TetraSpeck beads, which are therefore below the diffraction limit for an illumination at 642 nm. In (a) and (b) are the wide-field and Wiener-filtered images. The inset shows two neighboring beads not distinguishable without using SIM in (c) and (d). In (c) the 2D-SIM reconstruction with fairSIM is shown while (d) shows the full 3D-SIM reconstruction with the commercial SoftWORX package from the OMX (GE Healthcare). (e) and (f) show the cross-sections of two areas which also proves the similar resolution enhancement with both softwares.

The software was tested with data sets from several custom-build 2D and commercial 3D-SIM platforms. As mentioned in chapter 2.4.3 a successful SIM-reconstruction requires information about the parameters (pattern orientation, phase and frequency). FairSIM applies a parameter estimation following Gustafsson [59], by using weighted

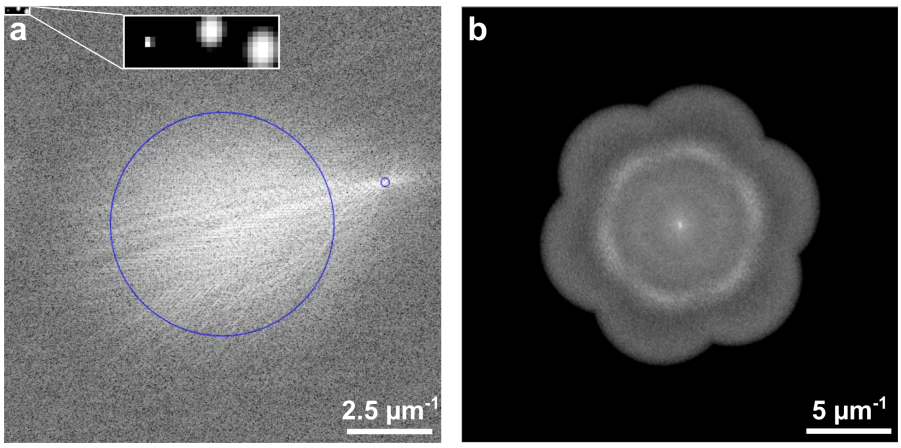

Figure 9.5.: Examples for intermediate SR-SIM results displayed as power spectra in frequency space: (a) Visualization of the cross-correlation used for parameter estimation, with circles marking the low-frequency region excluded from the fit and the detected modulation frequency. The three insets on the upper left visualize the iterative sub-pixel fits and provide a quick feedback if the fit was successful. (b) Power spectrum of the complete, reassembled SR-SIM reconstruction of fluorescent beads. The circular structure visible in the spectrum is located at about 4.5 μm^{-1}, which coincides with the bead size of 200 nm, and is thus expected. Taken from [99]

cross-correlation of frequency components to obtain the parameters. It also provides a phase-correction algorithm following [103].

An ideal biological sample for 2D-SIM are LSECs (see chapter 3.1). They are thin (less than 400 nm) and feature a very special morphological substructure: fenestrations with diameters of 50 - 200 nm which are below the diffraction limit. To verify the quality of fairSIM compared to the commercial software these cells are stained for the plasma membrane, imaged by a 3D-SIM and analyzed as depicted in Figure 9.6 (g-j). In the wide-field and Wiener-filtered image (a,b) the fenestrations cannot be resolved. However, in the single slice and the 3D-SIM reconstruction these structures can be seen and analyzed. This result enables the analysis of these cells in single-slice mode, i.e. with less phototoxic exposures and higher acquisition speeds.

9.3. Nanoparticles as nonfluorescent analogues of fluorophores

In the following are the revised results adapted from my 2015 published first-author paper 'Nanoparticles as nonfluorescent analogues of fluorophores for optical nanoscopy', see [35].

To date, fluorescence microscopy is the most widely used molecularly specific imaging technique in the biomedical sciences. This is explained by the relatively low cost of this microscopy modality, its capability for imaging live and fixed samples with a multitude of additional contrast mechanisms and colors, and the wide availability of

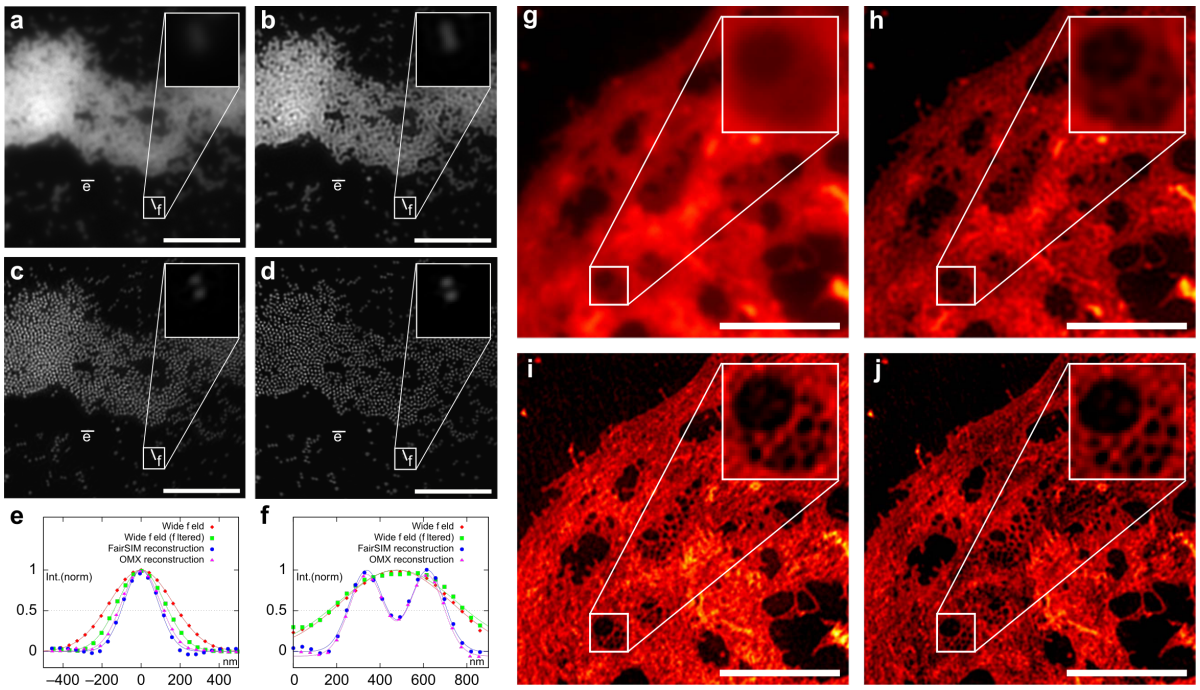

Figure 9.6.: FairSIM reconstruction of data sets of TetraSpeck beads and LSECs obtained on the GE Healthcare DeltaVision OMX (excited at 642nm wavelength). In contrast to the wide-field images (a and g) and its Wiener-filtered version (b and h), the single-slice/2D reconstructions by fairSIM (c and i) yield clearly distinct beads and cell membrane pores . The 3D SR-SIM reconstruction by SoftWORX (manufacturer software) is provided in (d) for comparison. Please note that the 3D reconstruction is based on a larger amount of input data (complete z-stack), which results in an improved signal-to-noise ratio. A quantitative comparison between (a - d) images can be found as cross-section plots for a single bead in (e) and for two adjacent beads (indistinguishable in wide-field mode) in (f). Scale bar (a-d): 5 µm, inset 1.2 µm; Scale bar (g-j): 5 µm, inset 1.6 µm, cells stained with CellMask Deep Red. Taken from [99]

fluorescent probes. Organic fluorophores are available either as intrinsically specific cellular stains or they can be reacted with a wide selection of biomolecules to render them molecularly specific. Fluorescent proteins, such as eGFP, can be fused with proteins of interest to result in intrinsically fluorescent samples (see also chapter 2.2, Figure 2.5). Super-resolution microscopy techniques improve the spatial resolution of fluorescence microscopy as explained in chapter 2.2.

A severe drawback of all fluorescence-based microscopy techniques is, however, the rapid photo-bleaching of organic fluorophores. Solutions to minimize this problem, i.e., oxygen-scavenging systems, can be utilized, but the underlying photochemical process cannot be entirely avoided, and, especially in live cell imaging, this still remains a significant problem for super-resolution microscopy. Alternatives to organic fluorophores, such as semiconductor quantum dots (Qdots) [34] or fluorescent nitrogen vacancy (NV) centers in nanodiamond particles [104] have been explored, but Qdots still exhibit some degree of photo-bleaching and uncontrolled blinking behavior and depending on the brightness NV nanodiamond particles are fairly large and cannot be multiplexed.

Another alternative presents itself in the use of Raman-active nanoparticles [105].

Raman scattering, the inelastic scattering of light by molecular bonds, results in Stokes and anti-Stokes scattered photons, where Stokes scattering is significantly stronger at room temperature. The scattered photons resemble a spectrum with sharp spectral lines that can be attributed to vibrations of different Raman-active groups within the sample. While spontaneous Raman scattering from biological samples by itself is typically too weak to serve as an alternative to fluorescent probes, enhancement mechanisms, such as coherent Raman scattering (CRS) [106] or surface-enhanced Raman scattering (SERS) [107] can produce signal strengths close to those observed from fluorescently labeled samples. Specifically, SERS nanotags, i.e., surface plasmon resonant gold or silver nanoparticles coated with an organic molecule that provides the Raman signature, can be targeted against biomolecules and could serve as a photostable, highly multiplexed optical probe [108].

Here, we explored the potential of using SERS tags as alternative labels for structured illumination microscopy. Super-resolution structured illumination microscopy (3D-SIM) uses illumination patterns with a periodicity close to the optical diffraction limit, typically generated as interference patterns, to excite fluorescence or, in our case, Raman scattering in a sample. The signal is collected as wide-field images and contains mixed spatial frequencies of the illumination pattern and the sample. If the down-shifted frequencies of sample structures below the diffraction limit can be identified and isolated, then a new image with up to twice the previous spatial resolution can be reconstructed (see also chapter 2.4.3). This method is attractive because it is very signal-efficient by collecting wide-field images with high numerical aperture microscope objective lenses and using single-photon-counting cameras. Also, it requires a low number of images, between 6 and 15, obtained for each z-plane within a sample to reconstruct the higher-resolution image. In this thesis I used 3D-SIM to image several biological samples stained with fluorophores, such as fenestrations in LSECs.

To overcome limitations imposed by photo-bleaching in all of these applications, I imaged SERS nanotags with 3D-SIM and compared their signal strength and signal persistence against those of commonly available fluorescent stains optimized for improved photostability. I found out that SERS nanotags can indeed be used as photostable analogues to fluorescent dyes for super-resolution microscopy of biological samples and offer additional benefits, such as the higher potential for multiplexing due to their spectrally narrow signatures [108] and chemical sensing capabilities [109].

3D Structured Illumination Microscopy of SERS Nanotags on a Glass Substrate

The potential of SERS nanotags to provide sufficient signal and contrast for super-resolution imaging by 3D-SIM was first investigated by depositing SERS nanotags onto a glass coverslip surface. The SERS nanotags are composed of 50 nm gold particles coated with trans-1,2-bis(4-pyridyl)ethylene (BPE) and surrounded by a SiO_2 shell (such as seen in Figure 2.5) [110]. The SERS nanotags were deposited onto the coverslip surface by allowing 10 µL of a 1:10 dilution of SERS nanotags in water to evaporate for 30 min at room temperature. This results in a glass surface with varying nanotag coverage: dense near the border of the droplet and less dense near the center of the droplet. For our

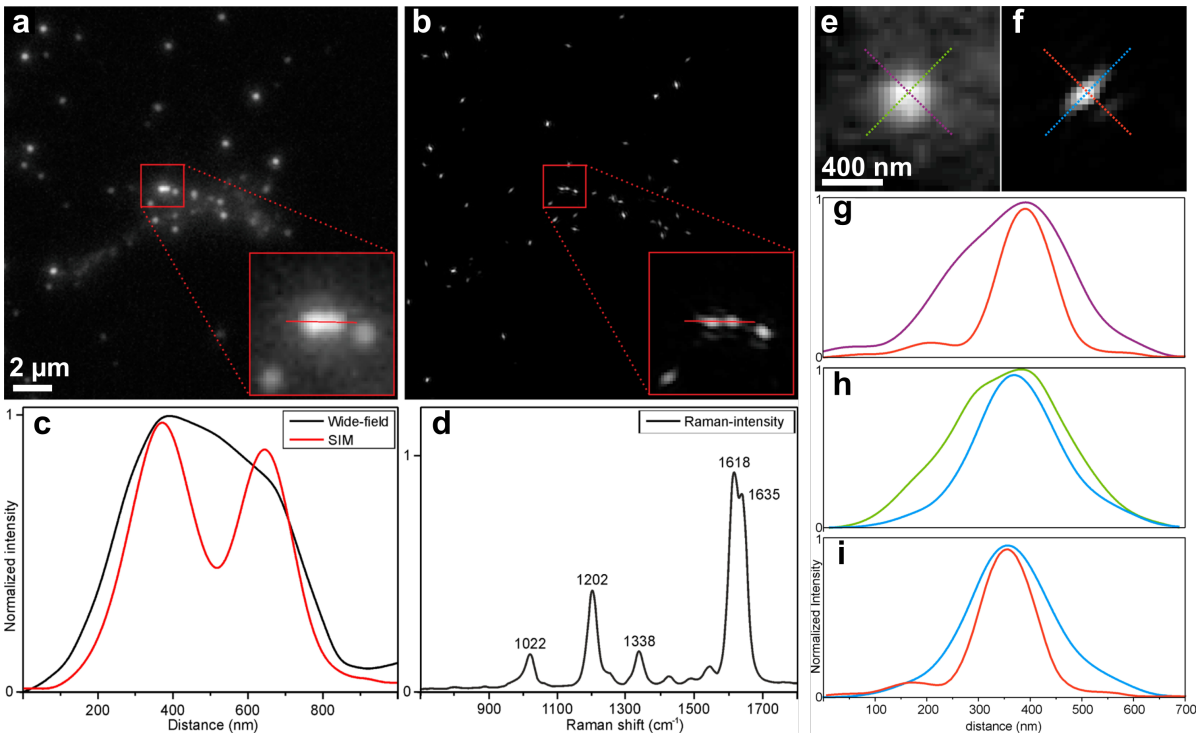

Figure 9.7.: SERS nanotags surface imaged by 3D structured illumination microscopy (3D-SIM). Images were acquired by exciting SERS nanotags at 642 nm and detecting the Stokes-shifted Raman signal through a 683/40 nm bandpass filter.
(a) Z-projection of a conventional wide-field image of the SERS tags. The projected image consists of eight single planes. (b) 3D-SIM reconstruction of the same area shown in (a). Single SERS nanotag particles can be clearly distinguished in the high-resolution image (see inset). (c) Cross-sections of the two particles shown in the insets of (a) and (b). Only the SIM reconstruction is able to separate the particles. (d) Surface-enhanced Raman spectrum of the nanotags. The particles show the typical SERS fingerprint spectrum of trans-1,2-bis(4-pyridyl)ethylene with well-separated vibrational peaks, as indicated by their Raman-active modes in the figure.
Comparison between the (e) wide-field image and (f) 3D-SIM reconstructed image of a single SERS nanotag. The colored dashed lines in the images indicate the directions of the cross-sections shown in the plots below. (g) Comparison between the cross-section along the wide-field (purple) and 3D-SIM (red) and the perpendicular case (h) (green) and 3D-SIM (blue). While the particle in the wide-field image appears to be fairly round with full width at half-maxima (fwhm) of 254 and 268 nm along the purple and green cross-sections, the fwhm of the SIM reconstruction are 107 nm (red) and 182 nm (blue). (i) Cross-sections of the SIM reconstruction shown for comparison. The graph clearly shows the difference in optical resolution along different directions within the SIM image. Taken from [35]

initial imaging experiments, I chose an area with a nanotag coverage of approximately 0.1 particles/µm^2 (Figure 9.7a, b). Images of the SERS nanotags were acquired on the commercial 3D-SIM setup (DeltaVision OMX V4-BLAZE, GE Healthcare). The wide-field images were obtained using standard wide-field illumination power density (approximately 20 W/cm2) by exciting the SERS nanotags at 642 nm.

Upon excitation at 642 nm, the SERS nanotags emit their characteristic SERS spectrum, as shown in Figure 9.7d. The Stokes-shifted SERS signal of the SERS particles

was collected using a 683/40 bandpass filter and imaged by a sCMOS camera. Individual SERS nanotags are clearly visible as white spots in the wide-field image (Figure 9.7a) and the 3D-SIM reconstruction (Figure 9.7b). However, as the insets to both images show, particles that are in close proximity (below the optical diffraction limit) cannot be resolved by wide-field microscopy, whereas the 3D-SIM reconstruction clearly identifies the particles as individual SERS nanotags. This is further confirmed by the comparison of the respective cross-sections through the particles, shown in Figure 9.7c. The distance between the particles is approximately 280 nm, as measured by 3D-SIM, which clearly is not sufficient to fully separate the particles in the wide-field image.

Interestingly, as becomes particularly evident from the enlarged view in the inset of Figure 9.7b, the SERS nanotags are reconstructed with an elliptical shape in the 3D-SIM image, whereas the wide-field image shows the particles as round spots. This behavior becomes even more apparent when we directly compare the spot dimensions of a single SERS nanotag in the wide-field and 3D-SIM images (Figure 9.7). Here, the 3D-SIM reconstruction appears highly excentric with a long axis along the vertical direction running from the lower left to the upper right of the image. A comparison of the cross-sections indicated in Figure 9.7e,f shows both the higher spatial resolution achieved by 3D-SIM as well as the elliptical artifact. Figure 9.7g compares the short axis of the images. The full width at half-maximum (fwhm) of the particle in the wide-field image measures approximately 254 nm (purple line), whereas the fwhm of the particle along the same axis in the 3D-SIM reconstruction measures 107 nm, resulting in a difference in apparent spatial resolution by a factor of approximately 2 in this direction. In the direction perpendicular to this, the particle diameter (fwhm) in the wide-field image measures 268 nm (green line), whereas the 3D-SIM reconstruction results in a width of 182 nm (blue line), resulting in only a 1.5 difference in spatial resolution. Figure 9.7i shows the discrepancy between the particle diameters measured by 3D-SIM by directly comparing the two cross-sections. Here, the difference in the reproduction of the width of the particle leads to an excentricity of 0.26.

As will be explained and verified in the following, we attribute this behavior to a reconstruction artifact due to the highly sensitive response of the SERS signal intensity to the polarization of the excitation light. As is well-known by now and as has been shown by multiple authors, SERS nanoparticles exhibit their maximum enhanced SERS signal intensity when the organic molecules giving rise to the Raman spectrum are located in the junction between two gold (or silver) nanoparticles [111]. These nanoparticles thus form a nanoparticle dimer, and the maximum enhancement of the electromagnetic field is achieved if the surface plasmons within the metal particles are excited along the dimer axis, i.e., if the polarization is parallel to the dimer axis [110]. For an excitation polarization perpendicular to the dimer axis, the SERS signal intensity will be minimal. The algorithm used to reconstruct 3D-SIM data, however, expects equal signal intensities for all angles of the SIM illumination pattern. Low signal-to-noise ratios result in a reconstruction with a poorer spatial resolution in the 3D-SIM image.

In 3D-SIM, however, in order to achieve the best contrast ratios for the interference patterns used as excitation patterns, the beams are linearly polarized. This polarization is rotated along the angles of illumination for each of the three angles that are used to

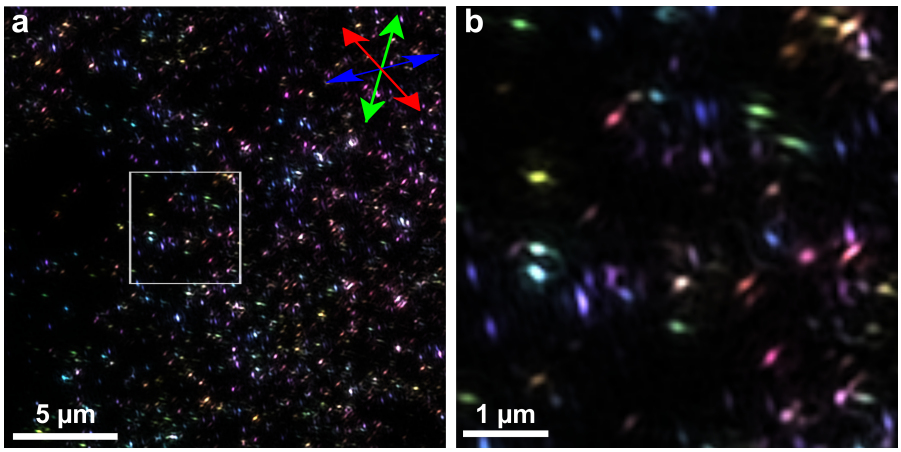

Figure 9.8.: Color-coded 3D-SIM reconstructions of SERS nanotags on a glass substrate. Red, green, and blue indicate the different angles (and therefore linear polarizations) at which the SIM data were acquired. (a) 3D-SIM overview of the SERS particles. Scale bar: 5 µm. (b) Zoomed view of the area highlighted in (a) by a white-dashed frame. Scale bar: 1 µm. Taken from [35]

obtain the 3D-SIM raw images. For the axis exactly perpendicular to the direction of the vector describing the orientation of the interference pattern, the SERS signal will be maximal. If, however, the SERS nanotag is oriented with its dimer axis parallel to the vector describing the interference pattern, then the SERS signal intensity will be minimal. This results in a highly elliptical reconstruction of the particle with a short axis (high spatial resolution) achieved for the high signal contrast and a poor spatial resolution obtained for the perpendicular direction.

I have verified this behavior by assigning different colors (red, green and blue) to the images obtained for the three different excitation angles used for 3D-SIM and by overlaying these colors with the 3D-SIM reconstruction of the particle images. The result is shown in Figure 9.8, where the colored arrows indicate the polarization for the different angles. Here, the SERS nanotags appear as a blend of the different colors assigned to the angles. As shown in the enlarged view in Figure 9.8b, the long particle axes clearly correspond to the different excitation angles, which verifies the highly polarization-dependent 3D-SIM reconstruction of SERS nanotags.

Despite this artifact, SERS nanotags still produce signal intensities rivaling those of organic fluorophores, yet they exhibit no photo-bleaching. This is shown in Figure 9.9, where U2OS cells were fixed and subsequently stained with Alexa 488 Phalloidin. After applying the fluorescent stain and three washing steps with PBS, SERS nanotags were applied to the sample and allowed to settle on the cell's surface. Using 3D-SIM, we were able to record structured illumination images from both sources, Alexa 488 and SERS particles, and compare their signal strengths against each other. Images are collected by exciting Alexa 488 with 0.1 kW/cm^2 for 10 ms and the SERS nanotags with 3 kW/cm^2 for 400 ms. Successful reconstruction of both channels using the set of SIM raw data obtained at the beginning of the experiment is shown in Figure 9.9a. Here, the Alexa 488 stain exhibited its brightest signal.

Figure 9.9b shows the same field of view using the same stains, after illuminating both

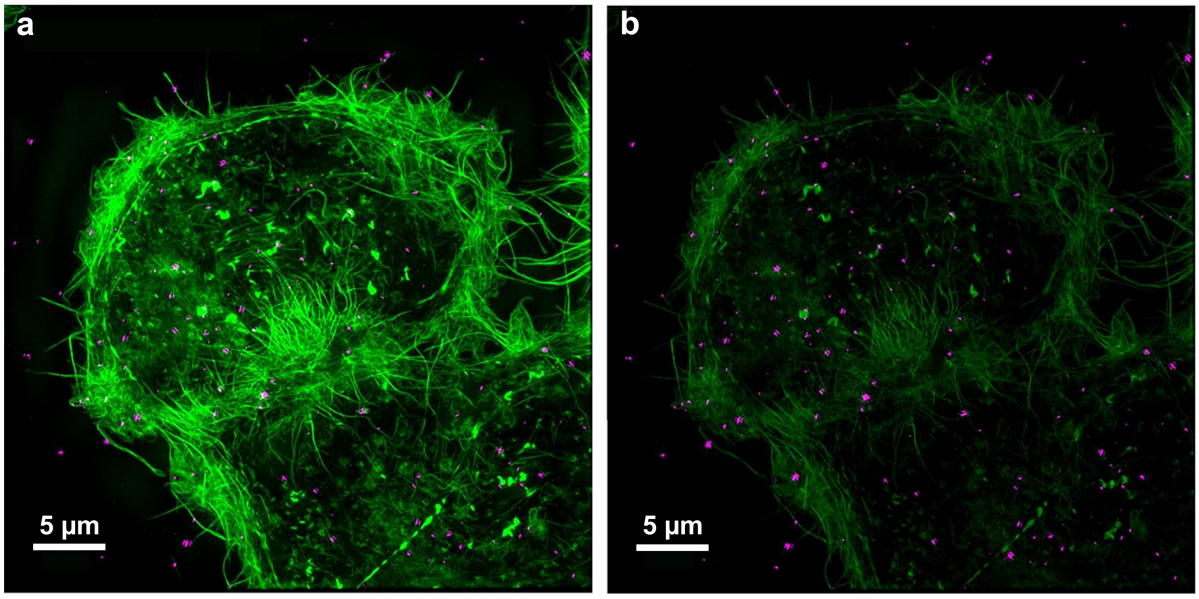

Figure 9.9.: Two-color z-projection of a 3D-SIM image of SERS nanotags (shown as magenta dots) lining a U2OS cell, where the actin cytoskeleton was stained with Alexa Fluor 488 Phalloidin (green). (a) The signal strength of the SERS nanotags in 3DSIM mode is comparable to that of the fluorescent stain, making the SERS tags easily distinguishable even against heavily stained samples. (b) SIM image of the same cell after 30 s of continuous illumination with approximately 1 kW/cm2 laser power density at 488 nm and approximately 3 kW/cm2 laser power density at 642 nm, acquired using the same conditions as in (a). The difference in brightness clearly shows the stability of the SERS nanotags against photo-bleaching in contrast to the Alexa 488 fluorophore. Scale bars: 5 µm. Taken from [35]

stains for 30 s with approximately 1 kW/cm2 laser power in the blue and approximately 3 kW/cm^2 laser power in the red excitation channels. As can be seen by the dramatic difference in contrast in Figure 9.9b, the Alexa 488 channel, although excited at even lower power than the nanotags, exhibited significant photo-bleaching after only 30 s, leading to a greatly reduced fluorescence signal. In contrast, the SERS signal remained at the same intensity level throughout the experiment, resulting in reliable reconstructions of the nanotags against the cell's background. This clearly demonstrates the potential of SERS nanotags as photostable analogues of fluorophores.

Photostability of SERS Nanotags

The use of conventional organic fluorophores and fluorescent proteins is plagued by rapid and irreversible photo-bleaching of the fluorescence. Typically, this is caused by a photoinduced reaction of the fluorophore in the excited state with molecular oxygen and can be reduced by using oxygen-scavenging systems in the imaging buffer. Especially in the case of live cell imaging experiments, however, the use of oxygen scavengers is also detrimental to cell health. photo-bleaching is a particular problem for super-resolution microscopy because pretty much all modalities require either the acquisition of multiple images or utilize rather high laser powers. Even 3D-SIM, which typically requires the

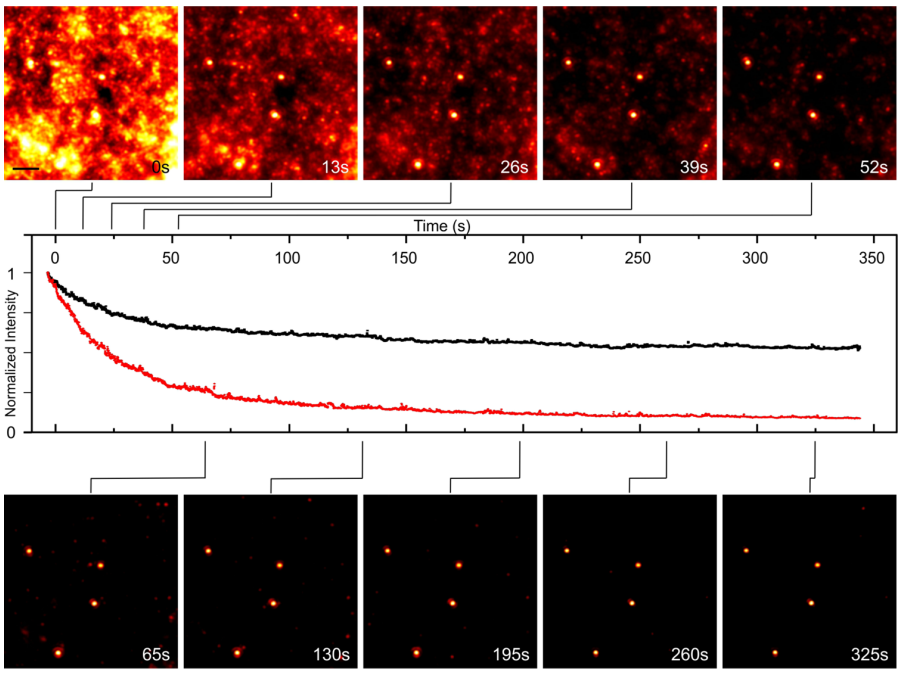

Figure 9.10.: Time-lapse image sequence of a mixture of SERS nanotags and organic fluorophores deposited onto a dry glass surface. SERS nanotags and Alexa Fluor 647 were dried on a cover glass surface and excited with 1 kW/cm2 at 643 nm. Both signals were detected simultaneously in the same channel at a frame rate of 15 Hz. Tracking the fluorescence and Raman intensity with time clearly shows the stability of SERS particles (four separated spots) in contrast to that of conventional fluorescent dyes. At the beginning of the measurement, the normalized signals taken at the location of a SERS nanoparticle (black curve) and a location of purely fluorescent dye (red curve) both start at a relative intensity of 1. After about 25 s (500 frames), the fluorescence intensity has decreased to 50% of its initial value. After 50 s, the fluorescence has almost fully vanished. Altogether, the fluorescence intensity decreases to 5% of its initial value. In contrast, the Raman signal is still well detectable after 350 s. It stabilizes at 60% of its initial value after approximately 160 s, representing the remaining SERS signal after the surrounding fluorescence contributions are photobleached. Graphical data were obtained by selection of a representative area for the fluorescence plot and selection of small areas containing the four individual spots with the SERS nanotags. Scale bar: 2 µm. Taken from [35]

lowest number of raw images to achieve a modest improvement in spatial resolution, suffers from this problem, leading to artifacts in the reconstruction of super-resolved images [112]. In order to establish the long-term photostability of SERS nanotags, we evaluated them by continuously taking wide-field images of a glass surface coated with a mixture of Alexa Fluor 647 and SERS nanotags. Alexa Fluor 647 was chosen because, in this case, both the fluorophore and the nanotags can be excited by the same laser excitation wavelength, enabling the direct comparison of their long-term signal stability. For these measurements, the mixture of SERS nanotags and Alexa 647 dyes on a coverslip was illuminated with a power density of 1 kW/cm^2 at 643 nm. The fluorescence and SERS signals were detected simultaneously with a single EMCCD camera. At the beginning of the measurement, signals from both types of particles are approximately equal in intensity (Figure 9.10). Within about 10 s following the

start of the continuous exposure, a decrease of the fluorescence signal is noticeable, and four bright spots identifying the location of the SERS nanotags become visible. Within 50 s of continuous illumination, most of the fluorescence has vanished. From this point on, only some faint blinking of the Alexa dyes can be detected. After 160 s, however, the intensity of the SERS nanotags reaches a stable value of 60% of their initial brightness and remains stable at this level until the end of the measurement. As shown in the Supporting Information (Figure S1 and accompanying text), the SERS signal of the nanotags can decrease depending on the illumination power. For high illumination powers (0.5 and2.6 kW/cm^2), an initial decrease in the SERS nanotag signal intensity was found. For lower illumination intensities (0.1 and 0.02 kW/cm^2), the SERS intensity levels remain stable. Expansions into the timetrace of the SERS signal show no blinking or major fluctuations down to a time scale of 3 ms.

We explain this behavior by first noting that the Raman-active probe molecule used for these nanotags, BPE, has an electronic absorption maximum at approximately 300 nm and no measurable absorption above 350 nm [113]. Thus, this molecule is entirely non-resonant for illumination at 642 nm and cannot photobleach at this wavelength. There are, however, other mechanisms leading to a reduction in intensity of the SERS signal, such as photoinduced molecular motion of the molecule due to repeated trans-cis or cis-trans isomerization [114]. This process does, however, also require resonant excitation of the molecule, which is not the case here.

Another possibility is detachment of the molecules from the nanoparticle surface due to photoactivation of the molecule (unlikely for non-resonant excitation) or absorption-induced heating of the nanoparticles based on their plasmon-induced absorption. The primary plasmon resonance of 50 nm gold nanoparticles exhibits a peak at 530 nm, whereas the peak of the quadrupole plasmon resonance in the case of dimerized gold nanoparticles depends on the distance between the nanoparticles and the electric permittivity of the environment [111]. For dimer-like nanoparticles in aqueous solution separated by BPE, the plasmon resonance peaks are at 680 nm or higher wavelengths [110]. In our setup, the imaging wavelength of 642 nm excites the nanotags on the leading edge of the quadrupole resonance. Exciting the particles closer to the peak resonance should boost the SERS signal even further, but this is currently not possible with our system.

3D Structured Illumination Microscopy of SERS Nanotags Internalized by Cells

To demonstrate that SERS nanotags can also be used after internalization in cell imaging applications, we conducted an initial proof-of-concept experiment. Here, U2OS cells, an osteosarcoma cell line, were incubated with SERS nanotags for 24 h to allow the cells to take up and internalize the nanotags. Prior to imaging, the cells were fixed with 4% PFA and the membrane of the U2OS cells was stained with CellMask Orange for the membrane. Each stain was imaged in its own color channel, i.e., excitation of CellMask Orange at 568nm and that of the SERS nanotags, at 642 nm. The cells were imaged by 3D-SIM before and after several bleaching steps, within which the fluorescence signal of CellMask Orange decreased dramatically, while the SERS nanotags maintain high

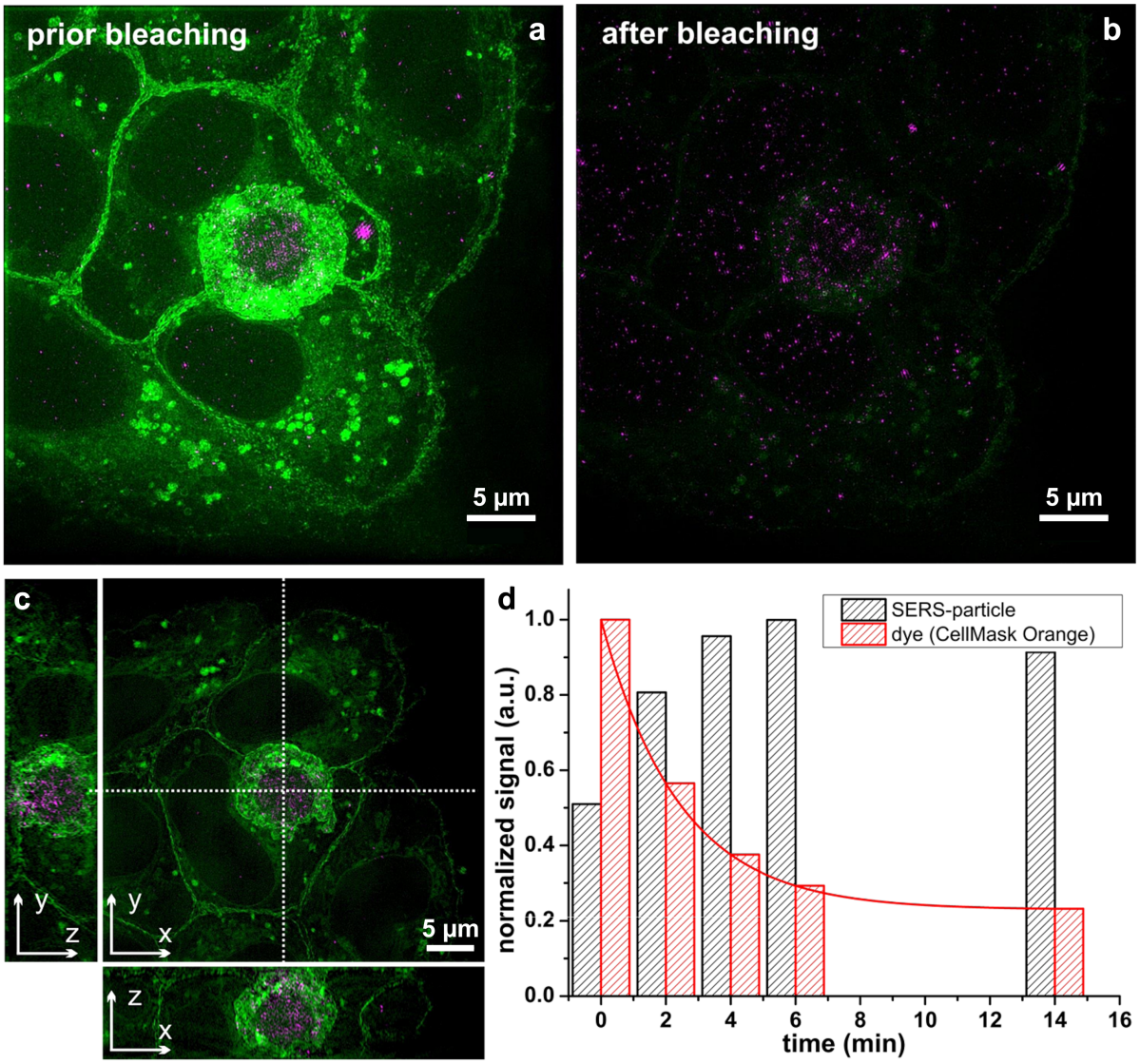

Figure 9.11.: 3D-SIM fluorescence and SERS images of living U2OS cells incubated with SERS nanotags for 24 h. (a) 3D-SIM reconstruction of the U2OS cells (stained with CellMask Orange, shown in green) and SERS nanotags internalized by the cells (magenta) (b) 3D-SIM reconstruction of the same cells after 14 min of continuous illumination. (c) 3D view as image cross-sections along the xy, xz, and yz directions of same U2OS cells. As can be seen by the xz and yz views, all SERS nanotags have been internalized by the cells. Dashed lines in the xy image indicate the position of the cross-sections. (d) Normalized intensity plot of the different channels following a 14 min illumination sequence. Whereas the fluorescent stain exhibits exponential photo-bleaching, the SERS nanotags are robust against photo-bleaching. Scale bars: 5 µm. Taken from [35]

brightness. This is demonstrated in Figure 9.11, where Figure 9.11a shows an overlay of the CellMask membrane stain (green) with the SERS nanotags (purple).

Figure 9.11b shows an image of the same cells after 14 min total bleaching time. The spectral separation between the stains enabled high-contrast imaging in each channel, respectively, with insignificant crosstalk between channels. The largest concentration

of SERS nanotags is found in the cell in the middle of the image. The surrounding cells, however, also contain nanotags, albeit at lower concentration. These particles have truly been internalized by the cells, as can be seen in Figure 9.11c, where we show cross-sectional views of the cells. SERS nanotags are clearly found in central locations within the cells, as is evident from the yz and xz cross-sections shown to the left and at the bottom of the xy image in Figure 9.11c. To further assess the signal strengths of the different stains,Figure 9.11d shows a normalized intensity plot of the different signals, where signal intensities were summed over the field of view in order to compensate for particle diffusion in the 3D-SIM projections. Timepoint 0 min is the initial z-projection of a 3D image (Figure 9.11a). Then, three subsequent bleaching steps of 2 min followed, and after every step, a measurement was conducted (time points: 2, 4, and 6 min). To correlate the temporal behavior of the photo-bleaching, equal laser powers were used in both channels. The final bleaching step took another 8 min of illumination, and the result was imaged at time point 14 min (Figure 9.11b). While the intensity of CellMask Orange decreases rapidly with the typical exponential decline found for high concentrations of organic fluorophores, the intensity of the SERS nanotags remained at a high level and, if anything, appears to have increased during the image sequence. These results show that SERS nanotags provide sufficient signal strength for wide-field imaging even against the background of fluorescent stains and the autofluorescence of cells.

In this project, I was able to show that SERS nanotags provide excellent and robust signal-to-noise ratios for imaging applications. These probes have, in particular, proven their suitability for super-resolution microscopy applications, where photo-bleaching of organic fluorophores is of concern and imposes a significant limitation. SERS nanotags, on the other hand, prove to be highly robust against photo-bleaching when excited outside any electronic resonances of the organic probe molecules that provide their Raman signature. Although we have not yet taken advantage of this property, their narrow spectroscopic signature should allow for multiplexed imaging of several tens of nanotags with different probe signatures simultaneously, if narrow bandpass filters are employed for imaging. Also, by implementing a ratiometric imaging modality, where different Raman peaks of the same nanotag are imaged onto different color channels, these particles could be used as local probes of their local environment [109]. By functionalizing the outer shell of the SiO2-coated nanotags, they can be directed against specific proteins on the surface or within the cytoplasm of cells [108]. If the physical size of the nanotags is of concern, small silver nanoclusters, often termed Ag nanodots [115], providing similar spectrally narrow signatures should also prove to be quite useful as alternative sources for super-resolution optical microscopy. We believe that such probes will pave the way into the future of live cell imaging applications for optical super-resolution microscopy, as they are only now beginning to become commercially available.

Conclusion and outlook

Nanoscopy of LSECs

The majority of my work was focused on imaging the structure and dynamics of living liver sinusoidal endothelial cells (LSECs). This research aimed at visualizing LSECs, including their important morphological substructure (fenestrations) by super-resolution microscopy methods.

LSECs have a membrane which is dissected by hundreds of nanopores, so-called 'fenestrations' with diameters of about 50 to 200 nm. Since the 1950s imaging of LSEC morphology was restricted to electron microscopies, such as TEM and SEM. I demonstrated that these physiologically highly relevant cells can also be investigated by different super-resolution microscopy techniques.

Single molecule localization microscopy applied to LSECs

I demonstrated that it is possible to resolve fenestrations with a spatial resolution of about 20 nm by single molecule localization microscopy (SMLM). In this super-resolution imaging method special photoswitchable dyes are required. Up to several tens of thousands of images are needed for the reconstruction of one super-resolved image. The main challenge for imaging LSECs is the negative contrast, as there are no markers for LSEC fenestrations, and thus they appear as dark structures against the brightly stained membrane. To accomplish this, the cellular plasma membrane was labeled at high fluorophore density with CellMask Deep Red and imaged using a reducing buffer system. Pore diameters of individual fenestrae with a diameter of less than 50 nm were identified in the reconstructed SMLM images. In addition I found that typical fenestrae have an appearance that does not necessarily resemble round holes as the limited resolution of 3D-SIM might imply. I further compared the higher degree of structural detail that SMLM provides to results obtained by 3D-SIM. The mean pore diameter observed by both techniques using wet sample preparation is 120-130 nm.

The protocols that I have developed enable SMLM on samples with negative contrast, with resolution and details comparable to SEM. To-date, these results still represent the highest resolved optical microscopy images of LSECs. My results opened up a path to image these physiologically important cells in vitro using fluorescence microscopes at very low cost and using wet sample preparation, thus enabling investigation of LSECs in most biomedical laboratories without the need for electron microscopy.

Multi-modal nanoscopy of LSECs

To obtain new insights into the association between the cytoskeleton and the plasma membrane that supports the formation of fenestrations of LSECs, I applied the complementary use of two different nanoscopy modalities, 3D-SIM and SMLM on a common optical platform. This multimodal nanoscopy method enabled me to rapidly survey quadruply-stained samples with 3D-SIM with about 100 nm resolution, which I combined with an even higher resolving (20nm) SMLM technique. At first I applied 3D-SIM to multi-color stained LSECs to rapidly acquire highly resolved overviews of large sample areas and surveyed the cells for fenestration sieve plates. I then further increased the spatial resolution to image fenestrations by applying SMLM to selected small regions of interest in the same sample on the same microscope setup. For this application I optimized the use of fluorescent membrane stains for both imaging conditions.

An advantage of this combination is that it enables the recognition of LSECs in a heterogeneous primary liver cells culture. The characteristic morphology including fenestrations and sieve plates cannot be seen in wide-field fluorescence microscopy and requires super-resolution capabilities. Imaging cells by 3D-SIM is significantly faster in acquisition time and leaner in data volume than SMLM, as 1000 times fewer raw images have to be acquired. The vast rapid survey of plated cells by 3D-SIM can then be followed by subsequent SMLM analysis at even higher spatial resolution.

This unique combination confirmed the direct correlation between the membrane and cytoskeleton in LSECs. The combination of different microscopy methods, including a faster lower-resolving three-dimensional and multi-color imaging method such as 3D-SIM, can provide added value for the analysis of the connection between different cellular constituents.

Membrane dyes and their effects on living LSECs

The most significant part of the work at hand is that I managed to obtain the first images of living LSECs, which enabled me to follow fenestration formation and dynamics. I showed that fenestrations do not remain fixed in their positions. They can move as pairs or isolated singles, they can divide into two, fuse together and increase their size until they close.

My research shows that staining living LSECs is challenging, because some dyes can have major detrimental effects on membranes and therefore cellular functions. Other stains provide additional insights beyond just fenestration structure by indicating unique lipid compositions in LSECs or they can even act as positive stains for fenestrations. Carbocyanine dyes made the first live LSEC dynamics observations possible.

This opens up the door to new analyses, as it enables testing the effects of drugs that have to pass the liver under lab conditions. The important role of LSEC fenestrations in the liver was underestimated for a long time. These findings will ultimately allow us to better understand which effects lead to liver failure due to drugs, alcohol and diet. It is important to note that, thanks to this work, it is now possible to directly observe the effects of different treatments of these cells. I demonstrated preliminary results

of different drug treatments such as actin disruptors on living LSECs. In addition I analyze the harmful effects on pre-treated rat LSECs with ethanol and paracetamol. A combination or an overdose with paracetamol lead to actin disruption and therefore a loss of fenestrations.

Instant SIM and further projects

I tested another state-of-the-art live-cell high-resolution imaging techniques, the instant SIM developed by York et al. This technique offers a resolution of about 145 nm with 100 frames/s imaging speed. This is especially useful for live cell imaging of fast dynamics and I showed that this technique could in principle be used for LSEC fenestration dynamics analysis. Furthermore I started to set up a two-photon instant SIM microscope, which will allow fast observations of dynamics in thick tissue samples with a nearly two-fold resolution increase.

All in all, the visualization of fenestrations in living LSECs has proven to be challenging, however, I was able to gain the first insights into their dynamics by combining the less-invasive 3D-SIM technique with non-destructive dyes.

Contributions to other projects

I applied the multimodal technique to other biological samples, e.g. the complementary analysis of lipid nanodomains in neural crest-derived stem cells (NCSCs). These raft-like lipid nanodomains are stained with cholera toxin fragment B (CTxB Alexa Fluor647) which is known to bind to Ganglioside 1. These nanodomains are believed to be crucially involved in the regulation of signal transduction pathways in mammalian cells. Because of their small size (diameter 10-200 nm), membrane nanodomains cannot be directly imaged using conventional light microscopy. Super-resolved fluorescence images obtained in this work reveal the distribution of Ganglioside 1 in NCSCs by 3D-SIM and SMLM. By this, I was able to show that in these mammalian cells the CTxB labels are arranged in the form of raft-like lipid nanodomains co-localized with actin. These results were independently confirmed by helium ion microscopy (HIM), which allowed us to exclude preparation and measuring artifacts in this fairly novel high contrast technique.

To make super-resolved SIM user-friendly and widely accessible, I contributed to development of the open-source reconstruction software fairSIM as a plugin for ImageJ/Fiji. SIM reconstruction is performed computationally on the acquired wide-field image data, and thus relies on a software implementation of specific SIM image reconstruction algorithms. FairSIM readily provides SIM reconstructions for a wide range of SIM platforms directly within ImageJ. With optical nanoscopy techniques becoming increasingly cost-effective, research groups building their own setups will be greatly benefiting from such ready-to-use reconstruction software. The solution that I helped develop is modular and flexible enough to be adapted to new needs, for example, the automated processing of large time series or the extension to non-linear SIM. In addition, users of commercial SIM platforms now have a tool at hand to perform reconstructions independent of the

manufacturer software, which allows in-depth data analysis even on-the-go and is not bound to a specific microscope workstation.

Furthermore I investigated the issue that super-resolution techniques are mostly restricted to fluorescence as contrast mechanism. Photo-bleaching of fluorescent probes ultimately limits the spatial resolution and observation time. This is fatal in 3D-SIM for the reconstruction of images, leading to artifacts, which make further analysis of the structure and kinetics of biological processes impossible. I was able to demonstrate that Raman scattering also provides valuable contrast for optical nanoscopy. I found that nanotags, i.e. gold and silver nanoparticles capable of surface-enhanced Raman scattering (SERS), can be imaged with a spatial resolution beyond the diffraction limit in four dimensions alongside and with similar excitation powers as fluorescent probes. The highly polarized nature of 3D-SIM renders these nanotags elliptical in the reconstructed super-resolved images, which enables us to determine their orientation within the sample. The robustness of nanotags against photo-bleaching allows us to image these particles for unlimited periods of time. My results show that SERS nanotags have the potential to become highly multiplexed and chemically sensitive optical probes for optical nanoscopy applications, such as following the evolution of biological processes for extended time scales. I believe that such probes will pave the way into the future of a variety of imaging applications for optical super-resolution microscopy, as they are only now beginning to become commercially available.

A. Preparation and staining protocols

The isolation of rat LSECs is already described in chapter 3.3. All samples are plated on #1.5 high precision cover glasses.

In case of fixation the following protocol was applied:

- Washing with pre-warmed PBS to remove the residues of the medium
- Incubation with pre-warmed Paraformaldehyde (PFA) (4% in PBS) for 10 minutes
- Washing three times with PBS and storing in the fridge at 4° C
- in case of long-term storage (2 weeks) or shipping from Norway cells were stored in 1-2% PFA

Fixed rat LSECs imported from Norway, followed a similar protocol: Rat LSECs were isolated from Sprague Dawley male rats (Scanbur BK, Sollentuna, Sweden) kept and fed under standard conditions. The treatment of the animals was performed in accordance with the Norwegian Animal Experimental and Scientific Purposes Act of 1986. The experimental protocols were approved by the Norwegian National Animal Research Authority (NARA). Young rats with a body weight between 150 and 300 g were anesthetized with a mixture of medetomidin (Domitor vet, Orion, Turku, Finland) and ketamine (Ketalar, Pfizer, New York, NY). The liver was perfused with collagenase and the isolated liver cells were centrifuged on a Percoll density cushion.

The isolated LSECs were plated on fibronectin or collagen coated #1.5 coverslips for 3h in RPMI-1640. The LSECs were then fixed with 4% paraformaldehyde (PFA) in phosphate buffered saline (PBS) and 0.02M sucrose, pH 7.2 for 15 min, and stored under PBS.

A.1. LSECs - Liver Sinusoidal Endothelial Cells

Figure 3.2

Live hLSEC were incubated with ULEX 1:50 for 20 min at 37° C, 5% CO_2. Then the cells were washed 3 times with PBS and fixed with PFA. After additional washing with PBS they were stained with CellMask Orange (1:2000), carefully washed and mounted in Vectashield including DAPI and sealed with nail polish.

Figure 3.4

Fresh: LSECs in suspension were stained with Vybrant DiO (1:200 in RPMI) and imaged 2h after seeding. Thawed: Thawed LSECs were fixed, washed and stained with CellMask Orange (1:3000) for 10 min. Then the sample was washed and mounted with Vectashield (including DAPI).

Figure 3.5

The fixed cells were permeabilized with 0.1% Triton X for 10 min at room temperature, followed by 2 washing steps with PBS. The Alexa Fluor 488 Phalloidin (1:40 of the methanol mixed stock solution in PBS) was incubated for 20 min at room temperature, followed by 2 washing steps with PBS. For the nucleus stain DAPI was incubated for 3 min with a 300nM concentration (in PBS) and subsequently washed 2 times with PBS. At last CellMask Deep Red (5µg/ml in PBS) was used to stain the membrane for 10 min at room temperature. Afterwards the sample was washed another 2 times with PBS and additionally fixed with 3% PFA for 10 min. 2 more washing steps with PBS followed. The LSM-imaging was done in PBS.

A.2. LSECs imaged by SMLM compared to 3D-SIM

The fixed samples were washed with PBS to remove unwanted residuals. The LSECs were stained with CellMask Deep Red plasma membrane stain at a concentration of 5 mg ml^{-1} for 10 min at room temperature. The staining solution was removed and the samples were carefully washed with PBS 2 to 3 times. For better background reduction the use of Tween 20 at 0.01% concentration in the washing solution proved to be beneficial.

For dye post-fixation 3.7% PFA was applied for 10 min at room temperature. Then the PFA was removed and the sample was again washed 2 to 3 times with PBS. Imaging was conducted in PBS buffer (adjusted to pH 7.4) with an oxygen scavenger system (glucose oxidase, catalase, glucose) and 100 mM MEA.

A.3. LSECs imaged by SMLM and 3D-SIM on the same setup

The fixed samples were washed with PBS. For Figures 5.1, 5.4 and 5.6 the LSECs were permeabilized for 90 s with 0.5% Triton-X100 and washed 2–3 times with PBS. Non-specific binding sites were blocked by incubating the cells for 90 min with 5% BSA in PBS at 4°C. The cells were incubated with the primary antibody (mouse anti beta-tubulin, 1:400) for 2 h at RT, then washed 3 times for 10 min with 0.1% PBS Tween-20. The secondary antibody (anti mouse Alexa Fluor 647, 1:400) was applied overnight at 4°C. The staining solution was removed and washing steps with 0.1% PBS Tween-20 (3 times for 10 min) and PBS followed. The Phalloidin Alexa Fluor 488 (1:40) and CellMask Orange (1:2000) were applied together for 20 min at 4°C. Cells were washed with PBS and post-fixed with 4% PFA for 10 min, followed by a PBS washing step.
The LSECs in Figure 5.6 were incubated with Phalloidin Alexa Fluor 488 (1:40) and Vybrant DiD (1:100) overnight at 4°C. All samples were mounted in Vectashield containing DAPI and sealed with nail polish. For Figure 5.2, LSECs were stained with CellMask Deep Red (1:2000), or Vybrant DiD (1:200) for 20 min at RT, respectively. For Figure

5.3 LSECs were stained with Vybrant DiD (1:200) for 20 min at RT. After removing the dye and rinsing each sample 3 times with PBS, these samples were mounted with a reservoir of an oxygen scavenging system including MEA.

A.4. Fluorescence stains and their effect on live cells

Figure 6.2

The fixed LSECs were stained with WGA Alexa Fluor 647 (1:100) for 10 min, washed with PBS and stained with CellMask Orange (1:3000) for 10 min. After 3 times washing with PBS, the sample was mounted with Vectashield including DAPI and sealed with nail polish.

Figure 6.3

The fixed LSECs were first permeabilized with 0.5% Triton-X for 30s and washed with PBS. Then the cells were stained with ULEX-FITC (1:100) for 30 min at room temperature, washed with PBS and stained with CellMask Orange (1:3000) for 10 minutes. The sample was mounted in Vectashield containing DAPI and sealed with nail polish afterwards.

Figure 6.4

The thawed LSECs were incubated with ULEX-FITC 1:100 for 60 min at 37° C, 5% CO_2 , then fixed with PFA. The sample was mounted in Vectashield containing DAPI and sealed with nail polish afterwards.

Figure 6.5

Freshly isolated LSECs were stained with Cell Mask Orange (1:2000 in RPMI) for 10 min at 37° C, 5% CO_2, then thoroughly washed with pre-warmed RPMI and imaged in fresh medium. Imaging was done for 60 min every 3 min with 10% 568 nm laser excitation and 2 ms acquisition time (see B.3).

Figure 6.6

Freshly isolated LSECs were stained with 1:10,000 CellMask Deep Red in RPMI for 10 min at 37° C, 5% CO_2. Then they were washed with RPMI and stained with 1:1,000 MitoTracker Red in RPMI. Imaging was done for 30 min every 30s in MitoTracker Red staining medium with low laser intensities (1% 568 nm for 10 ms, 0.1% 642 nm for 10 ms).

Figure 6.7

Freshly isolated LSECs were stained with VybrantDiO 1:100 in RPMI and incubated for 10 min at 37° C, 5% CO_2. Prior to imaging the staining solution was changed by fresh RPMI. Imaging was done for 25 min every 1 min in RPMI with 1 % 488 nm-excitation at 40 ms acquisition times (see B.3).

Figure 6.8

DiO: Freshly isolated LSECs were stained with VybrantDiO 1:200 in RPMI and incubated for 10 min at 37° C, 5% CO_2. Prior to imaging the staining solution was changed by fresh RPMI. Imaging was done for 30 min every 30s in RPMI with 1 % 488 nm-excitation at 40 ms acquisition times (see B.3).
DiD: Fixed LSECs in Fig. 4 were incubated Vybrant DiD (1:100) overnight at 4 ° C. Afterwards the sample was mounted in Vectashield (containing DAPI) and sealed with nail polish.

Figure 6.9

The fixed LSECs were incubated with Phalloidin Alexa Fluor488 (1:40) and Vybrant DiD (1:100) overnight at 4 ° C. All samples were mounted in Vectashield containing DAPI and sealed with nail polish afterwards.

Figure 6.10

The fixed LSECs were incubated with FastDiO (1:200) and CellMask Orange (1:3000) for 20 min at room temperature. After washing the sample was mounted in Vectashield containing DAPI and sealed with nail polish afterwards.

Figure 6.11

Freshly isolated LSECs were stained with FastDiO-stock (in DMSO) by premixing 1µl to 10µl PBS. This was added to 500µl RPMI and mixed and incubated for 30 min. Due to the poor staining the cells were additionally stained with 1:1000 CMO (60-70 min after FastDiO) for 5min at 37° C, 5% CO_2. For imaging the cells were washed with RPMI to reduce the CMO background.
The cell was imaged in the CellMask Orange channel (a) before and (b) after adding a 1µl of FastDiO-stock to this area.

Figure 6.12

The freshly isolated LSECs were stained before seeding them with 2 µl FastDiO-stock in 1ml cell suspension (1x10^6 cells). They were gently mixed and seeded in a total volume of 3 ml culture medium for 1.5 h at 37° C, 5% CO_2 Prior to imaging.

Figure 6.13 and 6.14

Freshly isolated LSECs were stained with FastDiO-stock (in DMSO) by premixing 1µl to 99 µl PBS. This was added to 400 µl RPMI and mixed and incubated for 10 min. Imaging was done for 30 min every 30s in FastDiO staining medium with moderate laser excitation (1% 568 nm for 5 ms, see B.3).

Figure 6.15

Thawed LSECs were stained with 1:5000 CellMask Deep Red and freshly stained on the microscope with 5µg/ml ice-cold FM4-64FX (in PBS) and directly imaged. Imaging was done by manually changing the laser while using the same emission filters as the microscope software would not allow automation of the acquisition. CellMask Deep Red was excited with 1% 642 nm for 20 ms and FM4-64FX was excited with 10% 488 nm for 20 ms. Due to bleaching the intensity and acquisition time was adapted to gain the necessary signal for a SIM reconstruction (30 ms with 10% 642 nm and 10% 488 nm)

Figure 6.16

Live LSEC were incubated with 1 µM SNARF-1 (in PBS) for 10 min at 37° C, 5% CO_2. Then the cells were washed 3 times with PBS and fixed with PFA. After additional washing with PBS they were mounted in Vectashield including DAPI and sealed with nail polish.

Figure 6.17

Thawed LSECs were stained with DPPE/BSA (DPPE dissolved in ethanol mixed 1:250 with 10µM defatted BSA) in RPMI. Imaging was done for 20 min every 30s in RPMI with 10 % 642 nm-excitation at 10 ms acquisition times (see B.3).

A.5. Fenestration dynamics and structural changes of living LSECs

Figure 7.1

Freshly isolated LSECs were stained with VybrantDiO 1:200 in RPMI and incubated for 10 min at 37° C, 5% CO_2. Prior to imaging the staining solution was changed by fresh RPMI. Imaging was done for 30 min every 30s in RPMI with 1 % 488 nm-excitation at 40 ms acquisition times (see B.3).

Figure 7.2

Freshly isolated LSECs were stained with VybrantDiO 1:200 in RPMI and mixed and incubated for 20 min at 37° C, 5% CO_2 prior to imaging. After checking the quality of the staining the medium was exchanged on the setup with 25nM Swinholide A in RPMI.

The timelapse (every 5 min for 90 min) started 10 min after treatment with Swinholide A with moderate laser excitation (1% 488 nm for 10 ms, see B.3).

Figure 7.3

Freshly isolated LSECs were stained with 1µM SIR-actin including 1µM verapamil in RPMI and incubated for 7h at 37° C, 5% CO_2 prior to imaging. After checking the quality of the staining the medium was exchanged on the setup with 25nM Swinholide A in RPMI. The timelapse (every 5 min for 120 min) started 5 min after treatment with Swinholide A with moderate laser excitation (0.1% 642 nm for 10 ms, see B.3).

Figures 7.4, 7.5 and 7.6

Freshly isolated LSECs were seeded on #1.5 coverslips in a 24 well plate. After 3h they were treated with 0.2% ethanol or 2 mg/ml paracetamol (APAP) in RPMI for 120 min at 37° C, 5% CO_2 (Figure 7.3). In the other experiment they were first pre-treated for 30 min with ethanol/APAP and then treated for another 90 min with APAP/ethanol (Figure 7.4). The medium in control was changed with pure RPMI. After 120 min the cells were fixed with 4% PFA. The fixed cells were permeabilized with 0.5 %TritionX for 30s and washed 2 times with PBS. The Alexa Fluor 488 Phalloidin (1:40 in PBS) was incubated for 20 min at room temperature, followed by 2 washing steps with PBS. Then CellMask Deep Red (1:1000 in PBS) was used to stain the membrane for 10 min at room temperature. Afterwards the sample was washed another 2 times with PBS and additionally fixed with 3% PFA for 10 min. 2 more washing steps with PBS followed. The cells were mounted in Vectashield including DAPI and sealed with nailpolish.

A.6. Instant SIM and its extension to two-photon microscopy

Fixed LSECs were permeabilized with 0.5% TritionX for 30s and washed 2 times with PBS. The Alexa Fluor 488 Phalloidin (1:40 in PBS) was incubated for 20 min at room temperature, followed by 2 washing steps with PBS. Then CellMask Orange (1:1000 in PBS) was used to stain the membrane for 10 min at room temperature. Afterwards the sample was washed another 2 times with PBS and additionally fixed with 3% PFA for 10 min. 2 more washing steps with PBS followed. The cells were mounted in Vectashield including DAPI and sealed with nailpolish.

A.7. Visualizing lipid nanodomains in mammalian cells

Super-Resolution Imaging of Lipid Rafts: NCSCs were plated on glass cover slips in DMEM containing 13% FCS and fixed with 4% PFA in PBS for 20 min at RT. Cells were then stained for 30 min with 0.1 µg/ml CTxB Alexa Fluor 647 conjugate (Life Technologies) and 165 nM Phalloidin Alexa Fluor 488 conjugate. Further NCSCs were

stained with 0.1 µg/ml DAPI in PBS for 10 min. All staining steps were executed at room temperature.

A.8. Open-source image reconstruction of super-resolution SIM data in ImageJ

LSECs

The fraction containing the LSECs was plated for selective adherence on fibronectin coated #1.5H coverslips (Paul Marienfeld GmbH & Co KG, Germany) in RPMI-1640. 3 h after plating, they were fixed with 4% paraformaldehyde for 15 min. For fluorescent staining of membranes, the LSECs were incubated with CellMask Deep Red plasma membrane stain (1:2000) for 10 min at room temperature (Fig 9.6).
LSECs were additionally permeabilized with 0.5% Triton-X for 30 s prior staining with 165nM Phalloidin Atto488 for 20 min at room temperature (Figure 9.4).

Preparation of TetraSpeck bead surfaces

TetraSpeck microspheres (200 nm, T-7280) were purchased from Thermo Fisher. Commercially available coverslips (B150 mm) with 24x60 mm^2 in size were carefully cleaned with HelmanexIII for 20 min in a supersonic bath at 45° C. Then, the coverslides were rinsed for two times with pure H_2O, followed by another 20 min in the supersonic bath in pure H_2O. Then, the coverslides were dried in an air flow prior use. A silicone sheet with a hole of 4 mm in diameter was disposed to the coverslip. A measure of 5 ml stock solution of TetraSpeck Microspheres was mixed with 5 ml H_2O and vortexed for 2min. The solution was dispensed onto the coverslip and dried headfirst over night at 4 ° C.

A.9. Nanoparticles as nonfluorescent analogues of fluorophores

U2OS Cells

U2OS cells were plated on cover glass, fixed and washed. For actin filament staining, the cells were permeabilized with Triton-X100 0.5%, washed three times with PBS and incubated with Alexa Fluor 488 Phalloidin for 20 min at room temperature. After washing three times, the PBS was removed, and 1 µl of the highly concentrated SERS nanotag stock solution was added. The sample was mounted in Vectashield and sealed with nail polish.

For the sample in Figure 9.11, U2OS were seeded in Labtek slides. They were incubated overnight with 2 µl of the SERS nanotag stock solution in 500 µl DMEM at 37° C in a 5% CO_2 environment. Afterwards they were washed with pre-warmed PBS and fixed with 4% PFA. After 2 times washing with PBS the fixed cells were stained with

CellMask Orange (1:10000) for 10 min. After thoroughly washing with PBS, the sample was imaged in PBS.

SERS Nanotags

The SERS nanotags used in this work were synthesized according to procedures established by Mulvaney and colleagues[116] and were provided to us as a free-of-charge sample by BD Biosciences. A solution of the SERS nanotags in doubly distilled water, derived at a dilution of 1:10 from the stock solution, was typically used for our experiments.

For the SERS nanotag surfaces, 10 µL of the 1:10 dilution was spread across the surface of a #1.5 coverglass. After evaporation of the liquid, the dry sample was mounted in glycerol on a glass slide and sealed with nail polish.

For Figure 9.10, 10 µL stock solution of SERS nanotags were diluted with 10 µL of $10^{-}7$ M Alexa 647 dissolved in H_2O. The sample was subsequently dried on a coverslip at room temperature.

B. Materials and methods

B.1. Materials

Alexa Fluor 488 Phalloidin (Thermo Fisher, #A12379),
Alexa Fluor 647 Phalloidin (Thermo Fisher, #A22287),
Type 1A Collagenase (Sigma Aldrich, #C9891),
RPMI (Gibco Invitrogen #11875-093),
CellMask Deep Red Plasma Membrane Stain (Thermo Fisher, #C10046),
CellMask Orange Plasma Membrane Stain (Thermo Fisher, #C10045),
MitoTracker Red (Thermo Fisher, #M7513),
FAST DiO (Thermo Fisher, #D3898),
Vybrant DiO (Thermo Fisher, #V22886),
Vybrant DiD (Thermo Fisher, #V22887),
Cytochalasin B from *Drechslera dematioidea* (Sigma Aldrich, #C6762),
Swinholide A from *Theonella swinhoei* (Sigma Aldrich, #S9810),
SIR-actin (SPIROCHROME),
SNARF-1 (Thermo Fisher, #S22801)
TetraSpeck Microspheres(Thermo Fisher, #T7280)
VECTASHIELD Mounting Medium with DAPI (Vector Laboratories, #H1200)
Mouse monoclonal Anti-beta-Tubulin antibody (Sigma Aldrich, #T8328)
Alexa Fluor 647 F(ab)2 Fragment of Goat Anti-Mouse IgG (Invitrogen, #A21237)
ULEX FITC (Sigma Aldrich, #L9006)
Verapamil (Sigma Aldrich, #V4629)

B.2. *d*STORM imaging

For the single molecule localization microscopy of conventional fluorophores (*d*STORM) in chapter 4, I used a custom-built setup as also described by van de Linde[57] and in [13]: I used an Olympus IX71 microscope equipped with an oil immersion objective (PlanApo 60x NA 1.45, Olympus) in the objective-type TIRF/HILO configuration to reduce the amount of out-of-focus light.

To enable controlled blinking of individual fluorophores, the CellMask stain was simultaneously illuminated by two continuous-wave laser beams of an ArKr-ion laser (Innova 70C, Coherent) which were selected by an acousto-optic tunable filter (AOTF). The 647 nm line was used for excitation while the 488 nm line was used for activation of the fluorophores. A dichroic filter (FF502/670) was used to separate the excitation/activation

light from the emitted fluorescence signal. Fluorescence images were acquired at high frame rates by an EMCCD camera (DV887DCS-BV, Andor) with emission filters (Bandpass 700/75, Longpass 647LP, Chroma Filters) directly mounted to the camera in order to remove residual laser excitation light. For each measurement the laser power was adjusted in such a way that single fluorophores appeared as dense as possible while being well separated for single molecule localization. In addition, the blinking rate had to be adjusted to the acquisition rate resulting in laser power densities of approximately 1–2 kW cm^{-2} at the sample.

Typically, for the final reconstruction of a super-resolved image up to 40 000 frames were acquired and analyzed by the open source reconstruction software rapidSTORM. Due to acquisition times of several minutes and a localization accuracy of a few tens of nanometers, sample drift had a significant negative effect on sharpness and contrast of the reconstructed images. Therefore, images were initially corrected for sample drift by assuming a linear drift using the built-in drift correction of rapidSTORM. To maximize the benefits of drift correction, we also developed an automated drift assessment tool. To further improve the visibility of fenestrations, all *d*STORM images in this paper were treated with a 2 pixel-wide (about 14 nm) Gaussian blur filter in the open-source software Fiji.

B.3. 3D-SIM imaging

For the 3D-SIM measurements shown in this thesis a DeltaVision OMX V4-BLAZE (GE Healthcare, Amersham, UK) is used. The system is equipped with five lasers with 405 nm (100 mW, Diode), 488 nm (100 mW, DPSS), 514 nm (100 mW, DPSS), 568 nm (100 mW, DPSS) and 642 nm (300 mW, DPSS) excitation lines. These lasers provide the illumination for the 3D-SIM and (ring-) TIRF mode. For the conventional wide-field mode a 6-color LED light source (InsightSSI) can be applied.

Four liquid-cooled sCMOS (customized PCO.edge) enable a detection in four different color channels simultaneously (TIRF, wide-field) or sequentially (SIM). For the SIM and correlative *d*STORM imaging an Olympus PlanApo N 60x 1.42 oil objective was used.

In general the intensities and exposure times are set to obtain satisfactory signal strengths in every channel without bleaching. A sequence of 15 images for each z-slice, obtained at three different angles with five phases each, was required to successfully reconstruct the super-resolution images. Typically, the images used in this thesis are maximum intensity projections of a 1 µm stack consisting of eight sections of 125 nm thickness.

The 3D-SIM reconstructions are done with the OMX-specific SoftWoRx software package for image processing.

Bibliography

[1] Ernst Abbe. Beiträge zur Theorie des Mikroskops und der mikroskopischen Wahrnehmung. *Archiv für mikroskopische Anatomie*, 9(1):413–418, 1873.

[2] Michel Orrit. Nobel prize in chemistry: Celebrating optical nanoscopy. *Nature Photonics*, 8:887–888, 2014.

[3] Stefan W Hell and Jan Wichmann. Breaking the diffraction resolution limit by stimulated emission: Stimulated-emission-depletion fluorescence microscopy. *Optics letters*, 19(11):780–782, 1994.

[4] Eric Betzig, George H Patterson, Rachid Sougrat, O Wolf Lindwasser, Scott Olenych, Juan S Bonifacino, Michael W Davidson, Jennifer Lippincott-Schwartz, and Harald F Hess. Imaging intracellular fluorescent proteins at nanometer resolution. *Science*, 313(5793):1642–1645, 2006.

[5] Michael J Rust, Mark Bates, and Xiaowei Zhuang. Sub-diffraction-limit imaging by stochastic optical reconstruction microscopy (STORM). *Nature methods*, 3(10):793–796, 2006.

[6] Rainer Heintzmann and Christoph G Cremer. Laterally modulated excitation microscopy: improvement of resolution by using a diffraction grating. In *BiOS Europe'98*, 1999.

[7] Mats GL Gustafsson. Surpassing the lateral resolution limit by a factor of two using structured illumination microscopy. *Journal of microscopy*, 198(2):82–87, 2000.

[8] E Wisse, RB De Zanger, K Charels, P Van Der Smissen, and RS McCuskey. The liver sieve: Considerations concerning the structure and function of endothelial fenestrae, the sinusoidal wall and the space of Disse. *Hepatology*, 5(4):683–692, 1985.

[9] Laurie D Deleve, Xiangdong Wang, Neil Kaplowitz, Howard M Shulman, Jannette A Bart, and Airenne Van Der Hoek. Sinusoidal endothelial cells as a target for acetaminophen toxicity: Direct action versus requirement for hepatocyte activation in different mouse strains. *Biochemical pharmacology*, 53(9):1339–1345, 1997.

[10] E Wisse. An electron microscopic study of the fenestrated endothelial lining of rat liver sinusoids. *Journal of ultrastructure research*, 31(1):125–150, 1970.

[11] Victoria C Cogger, Gregory P McNerney, Tun Nyunt, Laurie D DeLeve, Peter McCourt, Bård Smedsrød, David G Le Couteur, and Thomas R Huser. Three-dimensional structured illumination microscopy of liver sinusoidal endothelial cell fenestrations. *Journal of structural biology*, 171(3):382–388, 2010.

[12] Dmitri Svistounov, Alessandra Warren, Gregory P McNerney, Dylan M Owen, Dusan Zencak, Svetlana N Zykova, Harry Crane, Thomas Huser, Ronald J Quinn, Bård Smedsrød, et al. The relationship between fenestrations, sieve plates and rafts in liver sinusoidal endothelial cells. *PLoS One*, 7(9):e46134, 2012.

[13] Viola Mönkemöller, Mark Schüttpelz, Peter McCourt, Karen Sørensen, Bård Smedsrød, and Thomas Huser. Imaging fenestrations in liver sinusoidal endothelial cells by optical localization microscopy. *Physical Chemistry Chemical Physics*, 16(24):12576–12581, 2014.

[14] Atsushi Matsuda, Lin Shao, Jerome Boulanger, Charles Kervrann, Peter M Carlton, Peter Kner, David Agard, and John W Sedat. Condensed mitotic chromosome structure at nanometer resolution using palm and egfp-histones. *PloS one*, 5(9):e12768, 2010.

[15] Sabrina Rossberger, Gerrit Best, David Baddeley, Rainer Heintzmann, Udo Birk, Stefan Dithmar, and Christoph Cremer. Combination of structured illumination and single molecule localization microscopy in one setup. *Journal of Optics*, 15(9):094003, 2013.

[16] Virginie Hamel, Paul Guichard, Mathias Fournier, Romain Guiet, Isabelle Flückiger, Arne Seitz, and Pierre Gönczy. Correlative multicolor 3D SIM and STORM microscopy. *Biomedical optics express*, 5(10):3326–3336, 2014.

[17] Andrew G York, Panagiotis Chandris, Damian Dalle Nogare, Jeffrey Head, Peter Wawrzusin, Robert S Fischer, Ajay Chitnis, and Hari Shroff. Instant super-resolution imaging in live cells and embryos via analog image processing. *Nature methods*, 10(11):1122–1126, 2013.

[18] Matthias Schürmann, Natalie Frese, André Beyer, Peter Heimann, Darius Widera, Viola Mönkemöller, Thomas Huser, Barbara Kaltschmidt, Christian Kaltschmidt, and Armin Gölzhäuser. Helium Ion Microscopy Visualizes Lipid Nanodomains in Mammalian Cells. *Small*, 11(43):5781–5789, 2015.

[19] Gerd Binnig, Calvin F Quate, and Ch Gerber. Atomic force microscope. *Physical review letters*, 56(9):930, 1986.

[20] Dieter W Pohl, W Denk, and M Lanz. Optical stethoscopy: Image recording with resolution $\lambda/20$. *Applied physics letters*, 44(7):651–653, 1984.

[21] Max Knoll and Ernst Ruska. Das Elektronenmikroskop. *Zeitschrift für Physik*, 78(5-6):318–339, 1932.

[22] Max Knoll and Ernst Ruska. Beitrag zur geometrischen Elektronenoptik. i. *Annalen der Physik*, 404(5):607–640, 1932.

[23] Manfred von Ardenne. Improvements in electron microscopes. Patent, 1939. GB511204.

[24] Manfred Von Ardenne. Das Elektronen-Rastermikroskop. *Zeitschrift für Physik*, 109(9-10):553–572, 1938.

[25] JR Porter. Antony van Leeuwenhoek: Tercentenary of his discovery of bacteria. *Bacteriological reviews*, 40(2):260, 1976.

[26] Joseph R. Lakowicz. *Principles of Fluorescence Spectroscopy*. Springer, 3rd edition edition, 2006.

[27] Albert Sprague Coolidge, Hubert M James, and Richard D Present. A Study of the Franck-Condon Principle. *The Journal of Chemical Physics*, 4(3):193–211, 1936.

[28] Sebastian van de Linde, Mike Heilemann, and Markus Sauer. Live-cell super-resolution imaging with synthetic fluorophores. *Annual review of physical chemistry*, 63:519–540, 2012.

[29] Steven Yampolsky, Dmitry A Fishman, Shirshendu Dey, Eero Hulkko, Mayukh Banik, Eric O Potma, and Vartkess A Apkarian. Seeing a single molecule vibrate through time-resolved coherent anti-Stokes Raman scattering. *Nature Photonics*, 8(8):650–656, 2014.

[30] Osamu Shimomura, Frank H Johnson, and Yo Saiga. Extraction, purification and properties of aequorin, a bioluminescent protein from the luminous hydromedusan, Aequorea. *Journal of cellular and comparative physiology*, 59(3):223–239, 1962.

[31] Ulrich Kubitscheck. *Fluorescence microscopy: From principles to biological applications*. John Wiley & Sons, 2013.

[32] Nataliya Panchuk-Voloshina, Rosaria P Haugland, Janell Bishop-Stewart, Mahesh K Bhalgat, Paul J Millard, Fei Mao, Wai-Yee Leung, and Richard P Haugland. Alexa dyes, a series of new fluorescent dyes that yield exceptionally bright, photostable conjugates. *Journal of Histochemistry & Cytochemistry*, 47(9):1179–1188, 1999.

[33] Volker Buschmann, Kenneth D Weston, and Markus Sauer. Spectroscopic study and evaluation of red-absorbing fluorescent dyes. *Bioconjugate chemistry*, 14(1):195–204, 2003.

[34] X Michalet, FF Pinaud, LA Bentolila, JM Tsay, SJJL Doose, JJ Li, G Sundaresan, AM Wu, SS Gambhir, and S Weiss. Quantum dots for live cells, in vivo imaging, and diagnostics. *science*, 307(5709):538–544, 2005.

[35] Simon Hennig, Viola Mönkemöller, Carolin Böger, Marcel Müller, and Thomas Huser. Nanoparticles as nonfluorescent analogues of fluorophores for optical nanoscopy. *ACS nano*, 9(6):6196–6205, 2015.

[36] JE Aubin. Autofluorescence of viable cultured mammalian cells. *Journal of Histochemistry & Cytochemistry*, 27(1):36–43, 1979.

[37] Joseph W Goodman. *Introduction to Fourier optics*. Roberts and Company Publishers, 2005.

[38] Norbert Wiener. *Extrapolation, interpolation, and smoothing of stationary time series*, volume 2. MIT press Cambridge, 1949.

[39] William Hadley Richardson. Bayesian-based iterative method of image restoration. *JOSA*, 62(1):55–59, 1972.

[40] Leon B Lucy. An iterative technique for the rectification of observed distributions. *The astronomical journal*, 79:745, 1974.

[41] W. Schottky. Über spontane Stromschwankungen in verschiedenen Elektrizitätsleitern. *Annalen der Physik*, 362(23):541–567, 1918.

[42] M. Minsky. Microscopy apparatus. US patent 3,013,467, 1961.

[43] James B Pawley. Fundamental limits in confocal microscopy. In *Handbook of biological confocal microscopy*, pages 20–42. Springer, 2006.

[44] Andrew G York, Sapun H Parekh, Damian Dalle Nogare, Robert S Fischer, Kelsey Temprine, Marina Mione, Ajay B Chitnis, Christian A Combs, and Hari Shroff. Resolution doubling in live, multicellular organisms via multifocal structured illumination microscopy. *Nature methods*, 9(7):749–754, 2012.

[45] Claus B Müller and Jörg Enderlein. Image scanning microscopy. *Physical review letters*, 104(19):198101, 2010.

[46] Giulia MR De Luca, Ronald MP Breedijk, Rick AJ Brandt, Christiaan HC Zeelenberg, Babette E de Jong, Wendy Timmermans, Leila Nahidi Azar, Ron A Hoebe, Sjoerd Stallinga, and Erik MM Manders. Re-scan confocal microscopy: scanning twice for better resolution. *Biomedical optics express*, 4(11):2644–2656, 2013.

[47] Thomas A Klar and Stefan W Hell. Subdiffraction resolution in far-field fluorescence microscopy. *Optics letters*, 24(14):954–956, 1999.

[48] Stefan W Hell. Far-field optical nanoscopy. *science*, 316(5828):1153–1158, 2007.

[49] Mike Heilemann, Sebastian van de Linde, Mark Schüttpelz, Robert Kasper, Britta Seefeldt, Anindita Mukherjee, Philip Tinnefeld, and Markus Sauer. Fluoreszenzmikroskopie unterhalb der optischen Auflösungsgrenze mit konventionellen Fluoreszenzsonden. *Angewandte Chemie*, 120(33):6266–6271, 2008.

[50] Fang Huang, Tobias MP Hartwich, Felix E Rivera-Molina, Yu Lin, Whitney C Duim, Jane J Long, Pradeep D Uchil, Jordan R Myers, Michelle A Baird, Walther Mothes, et al. Video-rate nanoscopy using sCMOS camera-specific single-molecule localization algorithms. *Nature methods*, 10(7):653–658, 2013.

[51] Sebastian van de Linde, Anna Löschberger, Teresa Klein, Meike Heidbreder, Steve Wolter, Mike Heilemann, and Markus Sauer. Direct stochastic optical reconstruction microscopy with standard fluorescent probes. *Nature protocols*, 6(7):991–1009, 2011.

[52] Steve Wolter, Anna Löschberger, Thorge Holm, Sarah Aufmkolk, Marie-Christine Dabauvalle, Sebastian van de Linde, and Markus Sauer. rapidSTORM: Accurate, fast open-source software for localization microscopy. *Nature methods*, 9(11):1040–1041, 2012.

[53] Daniel Sage, Hagai Kirshner, Thomas Pengo, Nico Stuurman, Junhong Min, Suliana Manley, and Michael Unser. Quantitative evaluation of software packages for single-molecule localization microscopy. *Nature methods*, 12(8):717–724, 2015.

[54] Martin Ovesnỳ, Pavel Křížek, Josef Borkovec, Zdeněk Švindrych, and Guy M Hagen. ThunderSTORM: A comprehensive ImageJ plug-in for PALM and STORM data analysis and super-resolution imaging. *Bioinformatics*, 30(16):2389–2390, 2014.

[55] Russell E Thompson, Daniel R Larson, and Watt W Webb. Precise nanometer localization analysis for individual fluorescent probes. *Biophysical journal*, 82(5):2775–2783, 2002.

[56] Thorge Holm, Teresa Klein, Anna Löschberger, Tobias Klamp, Gerd Wiebusch, Sebastian van de Linde, and Markus Sauer. A Blueprint for Cost-Efficient Localization Microscopy. *ChemPhysChem*, 15(4):651–654, 2014.

[57] Sebastian van de Linde. *Photoswitching of organic dyes and single molecule based super resolution imaging*. PhD thesis, Bielefeld University, 2011.

[58] Alfonso De Simone, Stefano Gianni, and Michele Vendruscolo. *Bio-nanoimaging: Protein Misfolding and Aggregation*. Elsevier Inc., 2013.

[59] Mats GL Gustafsson, Lin Shao, Peter M Carlton, CJ Rachel Wang, Inna N Golubovskaya, W Zacheus Cande, David A Agard, and John W Sedat. Three-dimensional resolution doubling in wide-field fluorescence microscopy by structured illumination. *Biophysical journal*, 94(12):4957–4970, 2008.

[60] Anthony L Mescher. *Junqueira's basic histology: text and atlas*. Mcgraw-hill, 13 edition, 2013.

[61] DW Fawcett. Observations on th ecytology and electron microscopy of hepatic cells. *J Natl Cancer Inst*, 1955.

[62] JC Hampton. An electron microscope study of the hepatic uptake and excretion of submicroscopic particles injected into the blood stream and into the bile duct. *Cells Tissues Organs*, 32(3):262–291, 1958.

[63] E Wisse. An ultrastructural characterization of the endothelial cell in the rat liver sinusoid under normal and various experimental conditions, as a contribution to the distinction between endothelial and Kupffer cells. *Journal of ultrastructure research*, 38(5-6):528–562, 1972.

[64] Sigurdur Magnusson and Trond Berg. Extremely rapid endocytosis mediated by the mannose receptor of sinusoidal endothelial rat liver cells. *Biochemical Journal*, 257(3):651–656, 1989.

[65] Peter AG McCourt, Bård H Smedsrød, Jukka Melkko, and Staffan Johansson. Characterization of a hyaluronan receptor on rat sinusoidal liver endothelial cells and its functional relationship to scavenger receptors. *Hepatology*, 30(5):1276–1286, 1999.

[66] Montserrat Martin-Armas, Jaione Simon-Santamaria, Ingvild Pettersen, Ugo Moens, Bård Smedsrød, and Baldur Sveinbjørnsson. Toll-like receptor 9 (TLR9) is present in murine liver sinusoidal endothelial cells (LSECs) and mediates the effect of CpG-oligonucleotides. *Journal of hepatology*, 44(5):939–946, 2006.

[67] Karen Kristine Sørensen, Peter McCourt, Trond Berg, Clive Crossley, David Le Couteur, Kenjiro Wake, and Bård Smedsrød. The scavenger endothelial cell: a new player in homeostasis and immunity. *American Journal of Physiology-Regulatory, Integrative and Comparative Physiology*, 303(12):R1217–R1230, 2012.

[68] Allan J McLean, Victoria C Cogger, Guan C Chong, Alessandra Warren, Astrid Markus, Jane E Dahlstrom, and David G Le Couteur. Age-related pseudocapillarization of the human liver. *The Journal of pathology*, 200(1):112–117, 2003.

[69] Eddie Wisse, Filip Braet, Dianzhong Luo, Ronald De Zanger, Danny Jans, Evelyne Crabbe, and AN Vermoesen. Structure and function of sinusoidal lining cells in the liver. *Toxicologic pathology*, 24(1):100–111, 1996.

[70] Alessandra Warren, David G Le Couteur, Robin Fraser, David G Bowen, Geoffrey W McCaughan, and Patrick Bertolino. T lymphocytes interact with hepatocytes through fenestrations in murine liver sinusoidal endothelial cells. *Hepatology*, 44(5):1182–1190, 2006.

[71] Robin Fraser, Victoria C Cogger, Bruce Dobbs, Hamish Jamieson, Alessandra Warren, Sarah N Hilmer, and David G Le Couteur. The liver sieve and atherosclerosis. *Pathology-Journal of the RCPA*, 44(3):181–186, 2012.

[72] David G Le Couteur, Alessandra Warren, Victoria C Cogger, Bård Smedsrød, Karen K Sørensen, Rafael De Cabo, Robin Fraser, and Robert S Mccuskey. Old age and the hepatic sinusoid. *The Anatomical Record*, 291(6):672–683, 2008.

[73] Victoria C Cogger, Ute Roessner, Alessandra Warren, Robin Fraser, and David G Le Couteur. A sieve-raft hypothesis for the regulation of endothelial fenestrations. *Computational and structural biotechnology journal*, 8(11):1–9, 2013.

[74] SonyaA Clark, H Bramwell Cook, RobertB G Oxner, HelenB Angus, PeterM George, and Robin Fraser. Defenestration of hepatic sinusoids as a cause of hyperlipoproteinaemia in alcoholics. *The Lancet*, 332(8622):1225–1227, 1988.

[75] Anne-Marie Steffan, Jean-Louis Gendrault, and André Kirn. Increase in the number of fenestrae in mouse endothelial liver cells by altering the cytoskeleton with cytochalasin B. *Hepatology*, 7(6):1230–1238, 1987.

[76] Filip Braet, Ilan Spector, Ronald De Zanger, and Eddie Wisse. A novel structure involved in the formation of liver endothelial cell fenestrae revealed by using the actin inhibitor misakinolide. *Proceedings of the National Academy of Sciences*, 95(23):13635–13640, 1998.

[77] Jeremy Meyer, Carmen Gonelle-Gispert, Philippe Morel, and Léo Bühler. Methods for isolation and purification of murine liver sinusoidal endothelial cells: A systematic review. *PloS one*, 11(3):e0151945, 2016.

[78] Berit Hansen, Beatriz Arteta, and Bård Smedsrød. The physiological scavenger receptor function of hepatic sinusoidal endothelial and kupffer cells is independent of scavenger receptor class a type i and ii. *Molecular and cellular biochemistry*, 240(1-2):1–8, 2002.

[79] Reto Fiolka, Lin Shao, E Hesper Rego, Michael W Davidson, and Mats GL Gustafsson. Time-lapse two-color 3d imaging of live cells with doubled resolution using structured illumination. *Proceedings of the National Academy of Sciences*, 109(14):5311–5315, 2012.

[80] Lin Shao, Peter Kner, E Hesper Rego, and Mats GL Gustafsson. Super-resolution 3d microscopy of live whole cells using structured illumination. *Nature methods*, 8(12):1044–1046, 2011.

[81] Peter Kner, Bryant B Chhun, Eric R Griffis, Lukman Winoto, and Mats GL Gustafsson. Super-resolution video microscopy of live cells by structured illumination. *Nature methods*, 6(5):339–342, 2009.

[82] Viola Mönkemöller, Cristina Øie, Wolfgang Hübner, Thomas Huser, and Peter McCourt. Multimodal super-resolution optical microscopy visualizes the close connection between membrane and the cytoskeleton in liver sinusoidal endothelial cell fenestrations. *Scientific reports*, 5, 2015.

[83] Jane B. Reece Neil A. Campbell and Lawrence G. Mitchell. *Biology*. Benjamin-Cummings Pub Co, 5 edition, 1999.

[84] Kent Molin, Pam Fredman, and Lars Svennerholm. Binding specificities of the lectins PNA, WGA and UEA I to polyvinylchloride-adsorbed glycosphingolipids. *FEBS letters*, 205(1):51–55, 1986.

[85] Guanhua Xie, Lin Wang, Xiangdong Wang, Lei Wang, and Laurie D DeLeve. Isolation of periportal, midlobular, and centrilobular rat liver sinusoidal endothelial cells enables study of zonated drug toxicity. *American Journal of Physiology-Gastrointestinal and Liver Physiology*, 299(5):G1204–G1210, 2010.

[86] Daniel E Gomez, Hitoschi Yoshiji, Julie C Kim, and Unnur P Thorgeirsson. Ulex europaeus i lectin induces activation of matrix-metalloproteinase-2 in endothelial cells. *Biochemical and biophysical research communications*, 216(1):177–182, 1995.

[87] Martina Comiskey and Carol M Warner. Spatio-temporal localization of membrane lipid rafts in mouse oocytes and cleaving preimplantation embryos. *Developmental biology*, 303(2):727–739, 2007.

[88] Rebecca Notman, Massimo Noro, Brendan O'Malley, and Jamshed Anwar. Molecular basis for dimethylsulfoxide (dmso) action on lipid membranes. *Journal of the American Chemical Society*, 128(43):13982–13983, 2006.

[89] Marie-Amélie de Ménorval, Lluis M Mir, M Laura Fernández, and Ramon Reigada. Effects of dimethyl sulfoxide in cholesterol-containing lipid membranes: a comparative study of experiments in silico and with cells. *PloS one*, 7(7):e41733, 2012.

[90] Christian Eggeling, Christian Ringemann, Rebecca Medda, Günter Schwarzmann, Konrad Sandhoff, Svetlana Polyakova, Vladimir N Belov, Birka Hein, Claas von Middendorff, Andreas Schönle, et al. Direct observation of the nanoscale dynamics of membrane lipids in a living cell. *Nature*, 457(7233):1159–1162, 2009.

[91] Gražvydas Lukinavičius, Luc Reymond, Elisa D'Este, Anastasiya Masharina, Fabian Göttfert, Haisen Ta, Angelika Güther, Mathias Fournier, Stefano Rizzo, Herbert Waldmann, et al. Fluorogenic probes for live-cell imaging of the cytoskeleton. *Nature methods*, 11(7):731–733, 2014.

[92] Hidekazu Tsukamoto, Sally J Towner, Lefran M Clofalo, and Samuel W French. Ethanol-induced liver fibrosis in rats fed high fat diet. *Hepatology*, 6(5):814–822, 1986.

[93] ROBIN M Walker, WJ Racz, and TF McElligott. Scanning electron microscopic examination of acetaminophen-induced hepatotoxicity and congestion in mice. *The American journal of pathology*, 113(3):321, 1983.

[94] CHIFUMI Sato and CHARLES S Lieber. Mechanism of the preventive effect of ethanol on acetaminophen-induced hepatoxicity. *Journal of Pharmacology and Experimental Therapeutics*, 218(3):811–815, 1981.

[95] Linda J Pike. The challenge of lipid rafts. *Journal of lipid research*, 50(Supplement):S323–S328, 2009.

[96] F Goodsaid-Zalduondo, DA Rintoul, JC Carlson, and W Hansel. Luteolysis-induced changes in phase composition and fluidity of bovine luteal cell membranes. *Proceedings of the National Academy of Sciences*, 79(14):4332–4336, 1982.

[97] Kai Simons and Julio L Sampaio. Membrane organization and lipid rafts. *Cold Spring Harbor perspectives in biology*, 3(10):a004697, 2011.

[98] Matthias Schürmann, Natalie Frese, André Beyer, Peter Heimann, Darius Widera, Viola Mönkemöller, Thomas Huser, Barbara Kaltschmidt, Christian Kaltschmidt, and Armin Gölzhäuser. Helium Ion Microscopy: Helium Ion Microscopy Visualizes Lipid Nanodomains in Mammalian Cells (Small 43/2015). *Small*, 11(43):5852–5852, 2015.

[99] Marcel Müller, Viola Mönkemöller, Simon Hennig, Wolfgang Hübner, and Thomas Huser. Open-source image reconstruction of super-resolution structured illumination microscopy data in ImageJ. *Nature communications*, 7, 2016.

[100] Caroline A Schneider, Wayne S Rasband, Kevin W Eliceiri, et al. NIH Image to ImageJ: 25 years of image analysis. *Nat methods*, 9(7):671–675, 2012.

[101] Kevin O'Holleran and Michael Shaw. Optimized approaches for optical sectioning and resolution enhancement in 2D structured illumination microscopy. *Biomedical optics express*, 5(8):2580–2590, 2014.

[102] Kai Wicker, Ondrej Mandula, Gerrit Best, Reto Fiolka, and Rainer Heintzmann. Phase optimisation for structured illumination microscopy. *Optics express*, 21(2):2032–2049, 2013.

[103] Kai Wicker. Non-iterative determination of pattern phase in structured illumination microscopy using auto-correlations in Fourier space. *Optics express*, 21(21):24692–24701, 2013.

[104] Eva Rittweger, Kyu Young Han, Scott E Irvine, Christian Eggeling, and Stefan W Hell. STED microscopy reveals crystal colour centres with nanometric resolution. *Nature Photonics*, 3(3):144–147, 2009.

[105] X-M Qian and SM Nie. Single-molecule and single-nanoparticle SERS: From fundamental mechanisms to biomedical applications. *Chemical Society Reviews*, 37(5):912–920, 2008.

[106] Andreas Zumbusch, Gary R Holtom, and X Sunney Xie. Three-dimensional vibrational imaging by coherent anti-Stokes Raman scattering. *Physical review letters*, 82(20):4142, 1999.

[107] Paul L Stiles, Jon A Dieringer, Nilam C Shah, and Richard P Van Duyne. Surface-enhanced Raman spectroscopy. *Annu. Rev. Anal. Chem.*, 1:601–626, 2008.

[108] Cristina L Zavaleta, Bryan R Smith, Ian Walton, William Doering, Glenn Davis, Borzoyeh Shojaei, Michael J Natan, and Sanjiv S Gambhir. Multiplexed imaging of surface enhanced Raman scattering nanotags in living mice using noninvasive Raman spectroscopy. *Proceedings of the National Academy of Sciences*, 106(32):13511–13516, 2009.

[109] Chad E Talley, Leonard Jusinski, Christopher W Hollars, Stephen M Lane, and Thomas Huser. Intracellular pH sensors based on surface-enhanced Raman scattering. *Analytical chemistry*, 76(23):7064–7068, 2004.

[110] Kristin L Wustholz, Anne-Isabelle Henry, Jeffrey M McMahon, R Griffith Freeman, Nicholas Valley, Marcelo E Piotti, Michael J Natan, George C Schatz, and Richard P Van Duyne. Structure- activity relationships in gold nanoparticle dimers and trimers for surface-enhanced Raman spectroscopy. *Journal of the American Chemical Society*, 132(31):10903–10910, 2010.

[111] Chad E Talley, Joseph B Jackson, Chris Oubre, Nathaniel K Grady, Christopher W Hollars, Stephen M Lane, Thomas R Huser, Peter Nordlander, and Naomi J Halas. Surface-enhanced Raman scattering from individual Au nanoparticles and nanoparticle dimer substrates. *Nano letters*, 5(8):1569–1574, 2005.

[112] LH Schaefer, D Schuster, and J Schaffer. Structured illumination microscopy: Artefact analysis and reduction utilizing a parameter optimization approach. *Journal of microscopy*, 216(2):165–174, 2004.

[113] Evan J Blackie, Eric C Le Ru, and Pablo G Etchegoin. Single-molecule surface-enhanced Raman spectroscopy of nonresonant molecules. *Journal of the American Chemical Society*, 131(40):14466–14472, 2009.

[114] Mathieu L Juan, Jérôme Plain, Renaud Bachelot, Pascal Royer, Stephen K Gray, and Gary P Wiederrecht. Multiscale model for photoinduced molecular motion in azo polymers. *ACS nano*, 3(6):1573–1579, 2009.

[115] Junhua Yu, Sungmoon Choi, Chris I Richards, Yasuko Antoku, and Robert M Dickson. Live cell surface labeling with fluorescent Ag nanocluster conjugates. *Photochemistry and photobiology*, 84(6):1435–1439, 2008.

[116] Shawn P Mulvaney, Michael D Musick, Christine D Keating, and Michael J Natan. Glass-coated, analyte-tagged nanoparticles: A new tagging system based on detection with surface-enhanced Raman scattering. *Langmuir*, 19(11):4784–4790, 2003.

Acknowledgment

I would like to thank everyone who supported me during the last years. First, I want to express my gratitude to Prof. Dr. Thomas Huser for giving me the chance to work in his group and on all these exciting topics. You always supported me with ideas. I also want to thank Prof. Dr. Andreas Hütten for agreeing to act as reviewer of my thesis. For a great co-supervision I want to thank Dr. Wolfgang Hübner. It always was a pleasure to work with you, to discuss problems and benefit from your experience in biology and imaging.

I am also very grateful to Dr. Marcel Müller, who was always helpful and had an open ear for every problem.

I want to thank my colleges from the biology department, especially Dr. Peter Heimann and Prof. Dr. Christian Kaltschmidt for realizing LSEC isolations here in Bielefeld. This project would not have been possible without Dr. Cristina Øie and Prof. Dr. Peter McCourt from the Tromsø University. Thank you both! Especially Cristina I want to thank for the intensive and fruitful weeks of her visits.

I would like to express my gratitude to Dr. Gerd Wiebusch for a lot of technical advices and the support at the iSIM. Andreas Markwirth is also gratefully acknowledged for supporting the iSIM.

I want to thank Matthias Schürmann and Prof. Dr. Christian Kaltschmidt for the NCSC preparation and the good collaboration.

Many thanks to Dr. Andrew York and Dr. Hari Shroff for the possibility to visit the NIH and use their iSIM. It was a great experience.

I want to thank Dr. Sebastian van de Linde (Sauer Lab in Würzburg) for letting me visit their lab teaching me dSTORM. That gave me the possibility to re-establish dSTORM in our lab.

Dr. Simon Hennig I want to thank for the bleaching experiments on his setup and Carolin Böger for the Raman spectrum of the SERS particle. Many thanks to Saskia Bannister, Stephan Bergmann, Andreas Markwirth, Dr. Marcel Müller and Dr. Wolfgang Hübner for proofreading.

A special thank goes to Henning Hachmeister and Christian Pilger for all the fruitful discussions.

I want to thank all my friends at the Biomolecular Photonics group for their wonderful support during the last years. Thank you for the nice time and all the nice barbecue and movie nights!

The greatest thanks are to my family! Thank you for your never ending support!

Erklärung

Hiermit erkläre ich,

1. dass mir die geltende Promotionsordnung der Fakultät für Physik der Universität Bielefeld bekannt ist.

2. dass ich die vorliegende Dissertation selbst angefertigt, dabei keine Textabschnitte von Dritten oder eigener Prüfungsarbeiten ohne Kennzeichnung übernommen und alle von mir benutzten Hilfsmittel und Quellen in der Arbeit angegeben habe.

3. dass Dritte weder unmittelbar noch mittelbar geldwerte Leistungen von mir für Vermittlungstätigkeiten oder für Arbeiten erhalten haben, die im Zusammenhang mit dem Zustandekommen oder dem Inhalt dieser vorliegenden Dissertation stehen.

4. dass ich diese vorliegende Dissertation oder wesentliche Teile davon nicht als Prüfungsarbeiten für eine staatliche oder andere wissenschaftliche Prüfung eingereicht habe.

5. dass ich die gleiche, eine in wesentlichen Teilen ähnliche oder eine andere Abhandlung nicht bei einer anderen Hochschule als Dissertation eingereicht habe.

Viola Mönkemöller

Eingereicht am:

Diese Arbeit wurde auf säurefreiem, alterungsbeständigem Papier (gemäß DIN ISO 9706) gedruckt.

Publications and conference contributions

Publications

S. Bergmann, V. Mönkemöller, T. Huser (2016) Comment on „Magnetic-field-enabled resolution enhancement in super-resolution imaging“ *Physical Chemistry Chemical Physics* (accepted)

M. Müller, V. Mönkemöller, S. Hennig, W. Hübner, and T. Huser (2016). Open-source image reconstruction of super-resolution structured illumination microscopy data in ImageJ. *Nature Communications*, 7.

V. Mönkemöller, C. Øie, W. Hübner, T. Huser, and P. McCourt (2015). Multimodal super-resolution optical microscopy visualizes the close connection between membrane and the cytoskeleton in liver sinusoidal endothelial cell fenestrations. *Scientific Reports*, 5.

S. Hennig*, V. Mönkemöller*, C. Böger, M. Müller, and T. Huser (2015). Nanoparticles as nonfluorescent analogues of fluorophores for optical nanoscopy. *ACS Nano*, 9(6), 6196-6205. (* contributed equally to this work)

M. Schürmann, N. Frese, A. Beyer, P. Heimann, D. Widera, V. Mönkemöller, T. Huser, B. Kaltschmidt, C. Kaltschmidt and A. Gölzhäuser (2015). Helium Ion Microscopy Visualizes Lipid Nanodomains in Mammalian Cells. *Small*, 11(43), 5781-5789.

V. Mönkemöller, M. Schüttpelz, P. McCourt, K. Sørensen, B. Smedsrød, and T. Huser (2014). Imaging fenestrations in liver sinusoidal endothelial cells by optical localization microscopy. *Physical Chemistry Chemical Physics*, 16(24), 12576-12581.

Conference contributions

T. Huser, H. Hachmeister, C. Pilger, V. Mönkemöller, W. Hübner, S. Hennig, M. Müller, G. Wiebusch, and M. Schüttpelz. Extending super-resolution optical microscopy beyond fluorescence (2016) Invited Talk, ICON EUROPE 2016

T. Ebert, V. Mönkemöller, W. Hübner, A. Markwirth, T. Huser, and M. Müller. Investigating the optical sectioning power of 2-beam and 3-beam structured illumination microscopy (2016) Poster, ICON EUROPE 2016

V. Mönkemöller, C. Øie, P. Heimann, C. Kaltschmidt, B. Kaltschmidt, P. McCourt, T. Huser, and W. Hübner. Multimodal nanoscopy reveals unique structural dynamics of liver endothelial cells (2016) Talk, ICON EUROPE 2016

M. Müller, V. Mönkemöller, S. Hennig, W. Hübner, T. Huser. FairSIM - open-source SR-SIM reconstruction in ImageJ/Fiji (2016) Short-Talk/Poster, ICON EUROPE 2016

V. Mönkemöller, C. Øie, W. Hübner, P. McCourt and T. Huser Correlative 3D structured illumination and single molecule localization microscopy of fenestrations in liver sinusoidal endothelial cells (2015) Talk, Focus on Microscopy

T. Huser, V. Mönkemöller, W. Hübner, M. Müller, S. Hennig, C. Pilger, H. Hachmeister, G. Wiebusch, M. Schüttpelz. Super-resolution optical microscopy and colloids: a match well worth exploring (2015) Invited Talk, 11th Zsigmondy Colloquium of the Colloid Society, Bielefeld

P. McCourt, T. Huser, K. Sørensen,C. Øie, V. Mönkemöller, B. Ahluwalia, Optical nanoscopy to reveal structural and functional properties of liver cells (2015) Invited Talk, SPIE Optics and Photonics, San Diego, Nanoimaging and Nanospectroscopy

T. Huser, H. Hachmeister, C. Pilger, V. Mönkemöller, W. Hübner, S. Hennig, M. Müller, G. Wiebusch. Label-free super-resolution Optical Microscopyof Cellular Dynamics (2015) Invited Talk, Asia Communications and Photonics Conference (ACP)

T. Huser, V. Mönkemöller, M. Müller, S. Hennig, C. Pilger, H. Hachmeister, G. Wiebusch. Super-Resolution Structured Illumination Microscopy Using Raman Scattering as Contrast Mechanism (2015) Invited Talk, International Workshop on Novel Probes for Fluorescence Microscopy, Göttingen, Germany.

V. Mönkemöller, M. Schüttpelz, P. McCourt, K. Sørensen, B. Smedsrød, and T. Huser Imaging fenestrations in liver sinusoidal endothelial cells by optical localization microscopy (2014) Poster, PicoQuant Single Molecule Workshop

V. Mönkemöller, B. Dale, W. Hübner, B. Chen, and T. Huser. Distinguishing immature and mature HIV-1 particles by superresolution optical fluorescence microscopy (2013) Poster, DPG Spring Meeting

V. Mönkemöller, W. Hübner, B. Dale, B. Chen; G. McNerney, T. Huser. Distinguishing immature and mature HIV-1 particles by superresolution optical fluorescence microscopy (2013) Talk, CLEO/Europe-IQEC 2013.